ULTRA-HIGH-SPEED LASER-INDUCED BREAKDOWN SPECTROSCOPY (LIBS) APPLICATIONS USING A PULSE-BURST LASER SYSTEM

A Thesis

by

AYOBAMI OLUWAPELUMI SHOYINKA

Submitted to the Office of Graduate and Professional Studies of
Texas A&M University
in partial fulfillment of the requirements for the degree of

MASTER OF SCIENCE

Chair of Committee,	Waruna D. Kulatilaka
Committee Members,	Eric L. Petersen
	Alexei V. Sokolov
Head of Department,	Andreas Polycarpou

May 2019

Major Subject: Mechanical Engineering

ABSTRACT

Laser-induced breakdown spectroscopy (LIBS) is a technique that utilizes intense laser pulses to generate a localized plasma that can be used for chemical analysis via quantifying the elemental composition of a sample. During the LIBS process, the emission generated from the plasma is collected, sent through a spectrometer and typically imaged using an intensified charged coupled devices (CCD) array. Unique spectral lines can then be detected, quantified, and assigned to specific elements that make up the sample. For the first time, to the best of our knowledge, a custom-designed pulse-burst laser operating at 100-kHz repetition rate was used for an ultra-high-speed LIBS application. While conventional LIBS methods utilize 10-Hz repetition-rate lasers, the higher repetition rate of 100-kHz allows for a faster sampling rate; specifically, during high-speed, short duration events such as explosions and shockwaves. Consequently, the potential benefits and applications of ultra-high-speed LIBS were explored using the pulse-burst laser system.

In the preliminary studies, solid aluminum and copper targets were used for system characterization and calibration. Further studies were conducted to quantify the capabilities of high-speed LIBS for applications involving dynamic events lasting several milliseconds or less. Under the current experimental conditions, LIBS emissions from a high-exit-velocity air nozzle with additives of aerosol compounds were clearly recognized and detected at a high hit rate. Upon successful applications of the pulse-burst laser for preliminary testing, experiments were conducted during combustion of hydroxyl-

terminated polybutadiene/ammonium perchlorate (HTPB/AP) propellants doped with varying concentrations of metals consisting of aluminum (Al), and lead (Pb). The pulse-burst laser LIBS system was successful in detecting the released metallic particles within the hot reaction zone of HTPB/AP propellants. A calibration study showed a relationship between the concentration of metals within the propellants and the hit rate at which the pulse-burst laser pulses interact with metallic particles. The limit of detection (LOD) of metal particles in the hot reaction zone was successfully calculated for subsequent applications of the pulse-burst-laser-based LIBS for predicting the metallic concentration with respect to the baseline case of 16% aluminum propellant samples.

ACKNOWLEDGEMENTS

I would like to thank a few key individuals who were instrumental during this thesis research and in my overall success.

I would like to first thank my committee chair and advisor, Dr. Waruna Kulatilaka for the time and effort he dedicated to my growth and the completion of my degree. I am grateful for his guidance and support throughout this research. I would also like to thank my committee members, Dr. Eric Petersen and Dr. Alexei Sokolov for their time and insightful comments.

Next, I would to thank the department faculty and staff, colleagues of the Optical Diagnostics and Imaging Laboratory, and other friends for making the time spent at Texas A&M University so memorable and fun.

Finally, sincerest gratitude to my mother for her support and encouragement through the toughest moments, and to Danielle for her patience and love.

CONTRIBUTORS AND FUNDING SOURCES

Contributors

This work was supervised by a thesis committee consisting of Dr. Waruna Kulatilaka and Dr. Eric Petersen of the J. Mike Walker'66 Department of Mechanical Engineering and Dr. Alexei Sokolov of the Department of Physics and Astronomy.

All work for the thesis was completed by the student, in collaboration with Dr. Yejun Wang of the Optical Diagnostics and Imaging Laboratory at the J. Mike Walker'66 Department of Mechanical Engineering.

Funding Sources

The research was funded by grant from Strategic Environmental Research and Development Program (SERDP, Grant No. W912HQ-16-C-008), and the Office of Naval Research (ONR, Grant No. N00014-16-1-2578). The student also received partial financial support from the Texas A&M University Ralph James Fellowship, and The National GEM Consortium Fellowship

NOMENCLATURE

Item	**Definition**
Al	Aluminum
AP	Ammonium Perchlorate
C	Carbon
Cu	Copper
CH_2FCF_3	Tetraflouroethane
H	Hydrogen
HTPB	Hydroxyl-terminated polybutadiene
Hz	Hertz (s^{-1})
LIBS	Laser-induced breakdown spectroscopy
LOD	Limit of detection
ms	Millisecond
N	Nitrogen
Nd:YAG	Neodymium-doped yttrium aluminum garnet
Nu (v)	Frequency
O	Oxygen
Pb	Lead
ps	picosecond
SNR	Signal-to-noise ratio
σ	Standard Error

TABLE OF CONTENTS

Page

LIST OF FIGURES

Page

LIST OF TABLES

Page

1. INTRODUCTION

1.1. Laser-Induced Breakdown Spectroscopy (LIBS) and High Repetition Lasers

Laser induced breakdown spectroscopy is a powerful analytical optical technique used to analyze the chemical disposition of a material samples containing elemental additives such as aluminum (Al), Nitrogen(N), Hydrogen(H), copper(cu), magnesium(mg), and iron(Fe) in gunshot residue [1], flames [2, 3], Liquid gas [3] , explosives [4-6] and solid propellants [7, 8]. Metallic and non-metallic additives generally enhance combustion properties, concentration, specific impulses, and density of mixtures [9-12]. The attractiveness of LIBS has been rapidly growing in the last two decades. It is a technique that can rapidly and concurrently dissociate, excite, and ionize samples, and it is generally easy to implement even in complex environments. This technique can be applied on materials in the solid, liquid, or gas phases [13-15]. For these reasons, LIBS has been widely used in chemical, biological, radiological, nuclear, and explosive (CBRNE) material detection [13]. Although LIBS has historically been performed predominantly on solid samples, there have been studies that analyze aerosol particles and detecting several elemental particulates even in low concentrations and at ambient conditions [13, 16-26].

LIBS is widely considered non-invasive and convenient, primarily because it can be fielded in virtually any environment with little preparation and remote system operation. In LIBS a pulsed laser is used to target a sample. Upon contact, a plasma is generated with trace amounts of the sample ionized in the process. The ionized sample

signal can then be recorded by a detector, digitized and displayed as a spectrum [13, 15, 16]. It is common to use a high energy low repetition rate of 10-Hz to 30-Hz nanosecond (ns) lasers in LIBS applications due to the high energy generation in the hundreds of millijoules (mJ) regime. This is mainly due to the large commercial availability of these types of lasers [13]. Due to advances in laser technology, the LIBS community has investigated the benefits of ultra-short pulse laser systems such as femtosecond lasers for LIBS with up to 1-kHz repetition rates [8]. The driving force is that ultra-short pulses, when compared to nanosecond lasers yield higher spatial resolution. These types of lasers require less energy for ablation, produce ultra-fast excitations, and tend to rely less on gated detectors. [27-31]. The analysis of short-term duration events is extremely attractive, therefore an interest in high repetition rate lasers has been a major focus for many in the optical diagnostic community [32-36].

Over the last decade, there has been a significant increase in the interest in high-repetition pulsed laser systems that produce tens to thousands of laser pulses within a burst for imaging and variety of diagnostic applications [32, 37-41]. The high repetition rates of laser systems make it possible to optimize the integration time on the detection side over the pulse train, thereby improving the overall signal-to-noise ratio (SNR) of the system. High repetition laser systems also help in scanning and collecting the average spectrum of a sample to minimize the effects of surface non-uniformity and pulse to pulse variation uncertainties. For turbulent and reacting flows, it is beneficial to utilize repetition rates on the order of tens of kHz and above to record the dynamics of the flow [34, 42-47]. Therefore, we will be investigating the use of a custom designed pulse-burst laser. This is

to characterize and quantify the performance of a stable, high repetition rate laser for fast sampling rate of brief time scale events such as explosions and shock waves.

1.2. Significance of the Thesis Research

The primary objective of this work is to explore the capabilities of the high repetition nanosecond pulse-burst laser system in a LIBS application for detecting metallic particulates released in combustion events under atmospheric conditions. This work simulates real world applications using HTPB/AP solid propellants with metallic additives of varying concentrations in a gas-phase reaction zone. Many publications have highlighted the use of LIBS for elemental species detection, especially on airborne particles using standard nanosecond and femtosecond laser systems. Conversely, there are few records of a successful use of a high repetition rate pulse-burst laser used in LIBS applications [8, 24, 25, 48-51]. The success of this work can potentially expand on the limitations of standard 10–30-Hz nanosecond lasers through the increase in sampling rates and increased limit of detection (LOD). Furthermore, the success of this thesis can present potential possibilities to using high-repetition pulse-burst laser to analyze the dynamic behaviors of elemental particles in fast and short duration reactive events. The analytic capability of observing the dynamic behavior of elemental particles in ultra-fast and short events can present crucial information to better understand the characteristics of reactions in explosives and shockwave-induced reactions.

1.3. Thesis Outline

The objective of this work is to utilize a custom high repetition pulse-burst nanosecond laser system as an energy source to gather quantitative spectroscopic data

points on the time-resolved evolution of chemical species in particulate matter containing various elemental species such as aluminum (Al), copper (Cu), lead (Pb), hydrogen (H), oxygen (O), and carbon (C). Section 2, features a literature review of the principles, applications, and development of LIBS and Pulse-burst laser systems. Section 3 details the experimental apparatus, samples, sample preparations, and diagnostic procedures for the experiment and data collection. Section 4 discusses the result from preliminary analysis of solid targets, wavelength detection, laser energy characterization, gate delay optimization, and propellant strand studies. In section 5, there is a detailed analysis of aerosol elemental particle detection. The final section, section 6, summarizes the thesis with conclusions and recommendations for future works.

2. LITERATURE REVIEW

2.1. Principles of LIBS

2.1.1. Overview

LIBS is a powerful quantitative elemental analysis technique that utilizes an intense focused energy pulse from a pulsed laser to provide in-situ chemical composition analysis. The pulsed laser is a low-energy in the tens to hundreds of mJ per pulse. It is a high-energetic laser that, when interacting with elemental samples, creates a matter ionizing plasma which excites all present elemental species and ionic dispositions within a sample. Upon excitation, the plasma is collected by an optical detector through fiber optic cables (FOC) and filtered through a spectrometer for conversion to corresponding wavelengths and intensity of elemental constituents discovered [13, 16] . A common set-up for LIBS is shown in Figure 2.1.

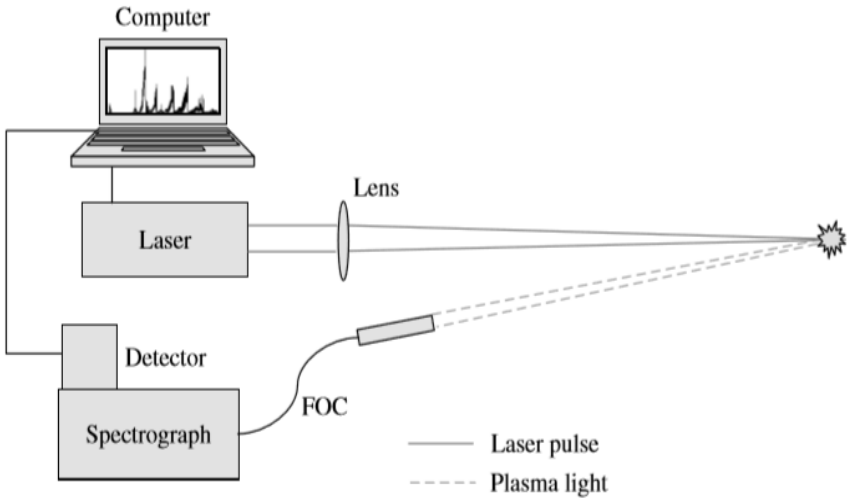

Figure 2.1 A commonly used apparatus for laser-induced breakdown spectroscopy experiments. Reprinted from [13]

Figure 2.2 displays the spectrum collected from a sample, the transition from low to high-resolution spectrum of elemental components, and surrounding background emissions. The focus of the soil analysis in Figure 2.2 was the detection of strong nitrogen spectra lines. However, the elements displayed in the figure below are trace amounts present in the soil.

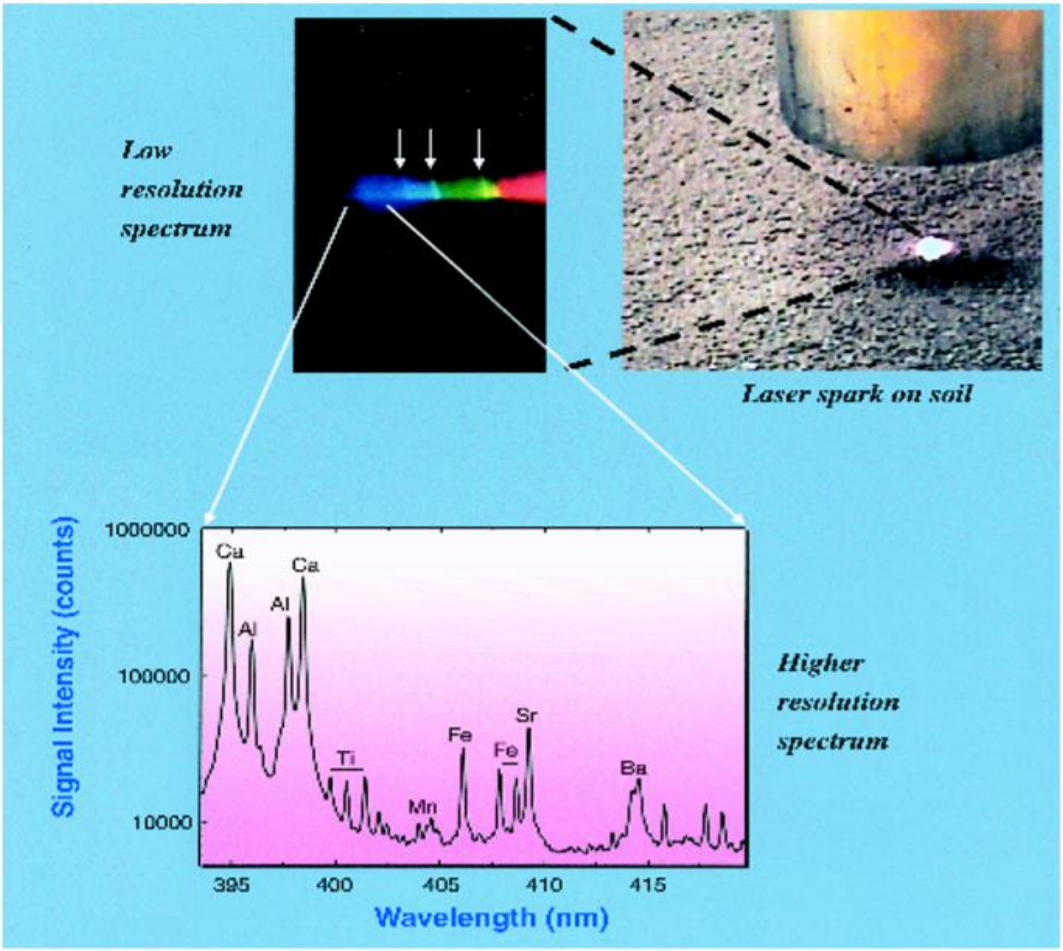

Figure 2.2 LIBS spectrum collected from a soil sample. Reprinted from [13]

2.1.2. Plasma Generation

The basis of plasma generation is governed by the interaction between protons and electrons. A plasma is induced by the interaction between a laser pulse and the target sample. There are discrete lines within the plasma that characterize the sample of interest. There are 3 main focal points to the generation of a successful plasma and particle emissions in a LIBS experiment: the plasma ignition process, the expansion and cooling process, the particle emission process [13]. Figure 2.3 displays the stages of LIBS plasma life and effects. Figure 2.4 displays an image of a plasma generated during the pressurized aerosol segment of this work.

In the plasma ignition process, the laser beam is focused through a focusing lens to generate a plasma at the location of interest. This stage is where bonds begin to break and is strongly dependent on the pulse duration and irradiance of the laser. For nanosecond lasers, there can be plasma shielding occurrences due to pulse durations. This phenomenon can influence how much of a target mass is converted to vapor due to the subsequent increases in heating from pulses. The expansion process is generally the directional propagation of shockwave induced by the vaporized mass within the plasma as it expands. This process is crucial in LIBS analysis and measurement, and it is dependent on the conditions of the sample and environmental properties (matter state, temperature, and pressure) in which the experiment takes place. During the expansion process, as temperature of plasma and number density decrease, particle atomic emission lines are generated and carried within the plasma. The next step, particle ejection and condensation, is not crucial to LIBS analysis because the emission is a mass of the sample that was

ablated by the laser pulse but not excited to provide information conducive to the basic LIBS measurement parameters [16, 52].

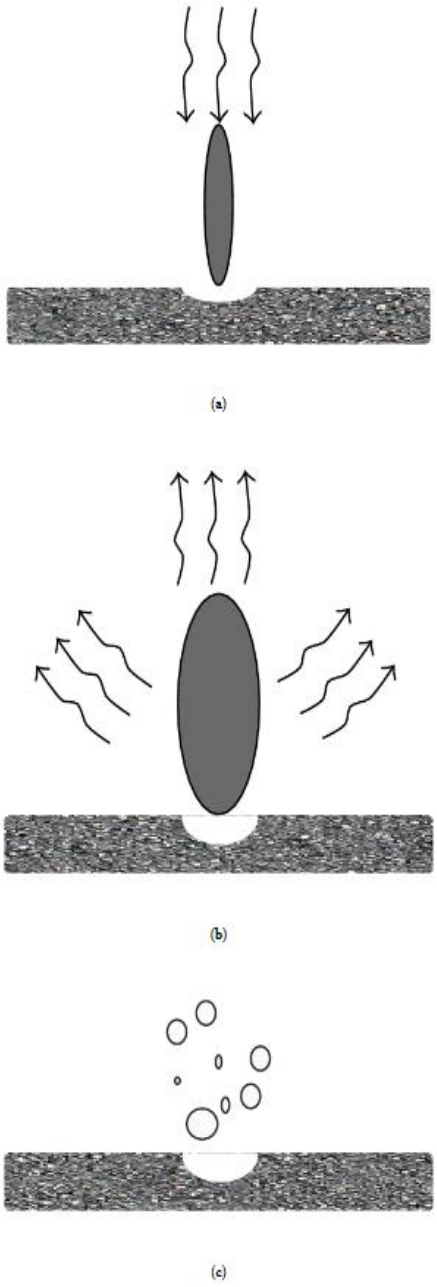

Figure 2.3 Plasma and particle emission process: (a) plasma ignition, (b) plasma expansion and cooling, (C) particle emission. Reprinted from [52]

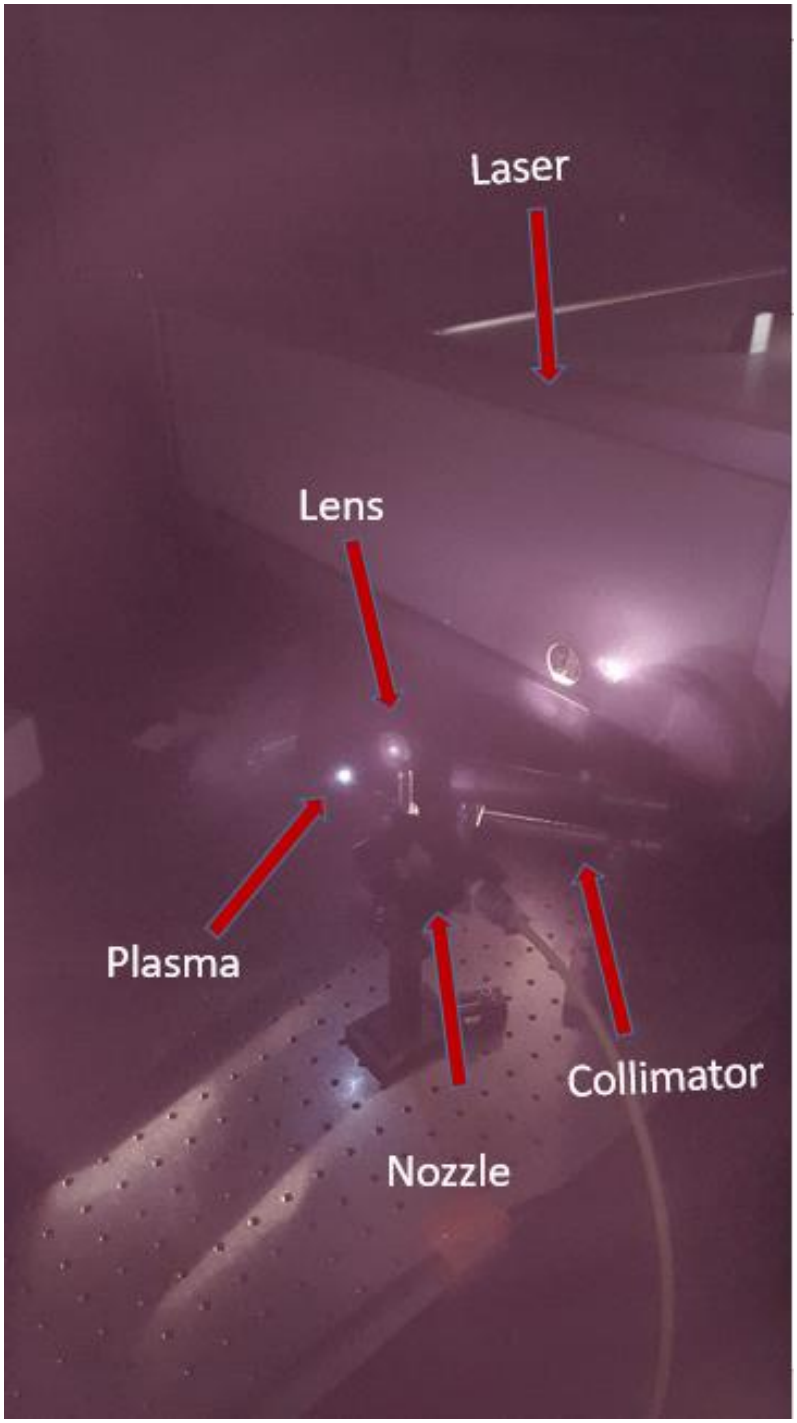

Figure 2.4 Image of plasma generated under high-speed flow conditions through a 2.5 mm exit, 6.5 mm inlet under-expanded nozzle

2.1.3. Characterization of Laser-Generated Plasmas

The characteristics of a plasma is the culmination of molecules, ions, and electrons, and can be directly characterized by plasma temperature (measured with Boltzmann method), electron density, and level of ionization [13, 16] .Consequently, the line emission created in LIBS from the plasma plays a crucial role in analytical strategies of electron density and temperature with the presence of Doppler width and stark effects. Some of these analytical strategies for studying electron densities involve Rayleigh, Thompson scattering, Langmuir probe, and Schlieren. Stark effects are caused by the collision of electrons and ions, while Doppler width is based on the absolute temperature and the atomic weight of the elemental emission species of focus. The full width half maximum (FWHM) of the line emissions generated through a Lorentz function can be used to estimate electron number densities and plasma temperature with the following Stark-effect equation [16].

$$\boldsymbol{N_e = C(N_e, T)(\Delta\lambda_s)^{1.5} = 8.02 * 10^{12}\left(\frac{\Delta\lambda_{\frac{1}{2}}}{\alpha_{\frac{1}{2}}}\right)^{1.5}} \qquad \textbf{(1)}$$

Where $\Delta\lambda_{\frac{1}{2}}$ is the FWHM, $\alpha_{\frac{1}{2}}$ is the stark width coefficient that is a function of temperature and pressure, N_e is the electron density, T is temperature, C is a constant based on the electron density and temperature. Figure 2.5 displays an example of measurements of electron temperature and densities of the O (I) lines calculated with the Langmuir probe measured with the stark effects, and Boltzmann method. The open squares are electron densities calculated with Stark effect method at 500-mJ/pulse. The open circles are

temperature calculated using the Boltzmann method at 500-mJ/pulse. The black circles and open triangles are electron temperatures measured with the Langmuir probe at 500-mJ/pulse and 800-mJ/pulse respectively

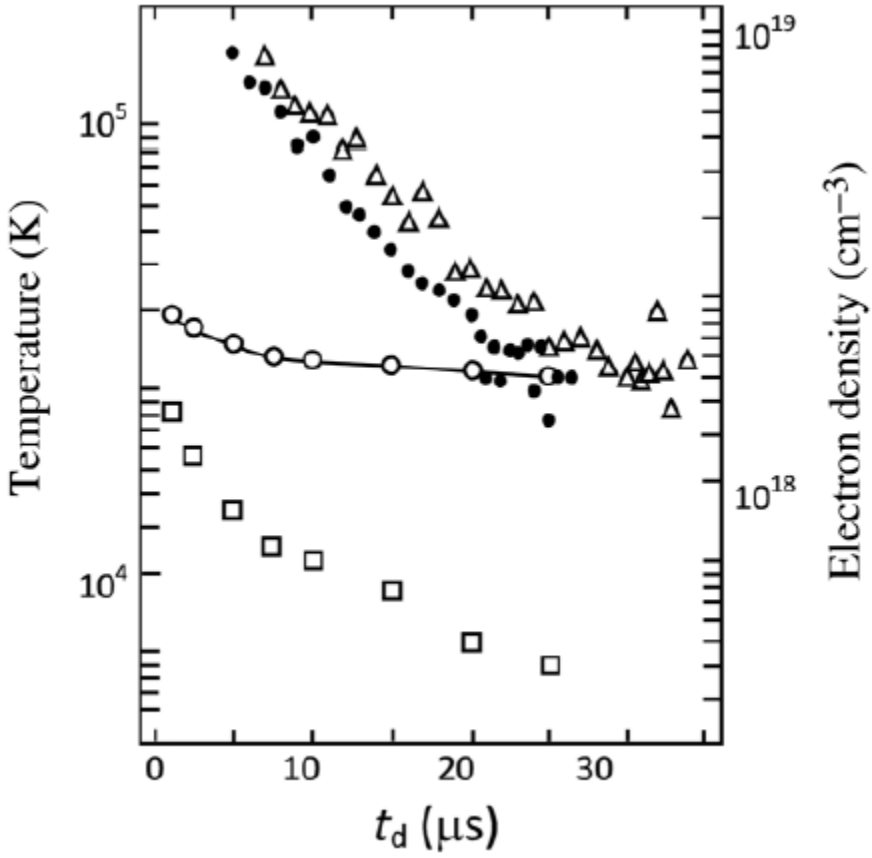

Figure 2.5 Electron temperature and density relationships measured with different diagnostic methods of O (I) lines. Reprinted from [13]

2.1.4. LIBS Experimental Components

Figure 2.1 displayed a general overview of the components needed for typical LIBS experimentation and analysis.

The purpose of a laser in LIBS is to generate a powerful enough energy pulse to vaporize a sample and form the plasma. The wavelength, pulse energy, pulse duration (explained in plasma generation section), and beam quality of the laser are all properties that typically affect the generation of a plasma. As explained in the review article by A. Anabitarte et al., laser wavelength influence can be described through energy absorption and the interaction between plasma and target material [52]. To summarize, a shorter wavelength increases material ablation rate, but increases the threshold for plasma generation. However, a longer wavelength decreases material ablation rate and increase fractionation (redistribution of elements between phases) but increases inverse Bremsstrahlung occurrence which assists in the reheating of plasma. Inverse Bremsstrahlung is the absorption of energy during plasma expansion to raise the energy and temperature of electron particles. The most commonly used wavelengths in LIBS are 1064-nm, and 532-nm. Depending of the type of LIBS analysis, longer or shorter wavelength can be utilized. Laser pulse energy is the energy per unit area induced on the material for the ablation process. Laser energy effect is dependent on the wavelength selection, laser repetition rate and pulse duration. Therefore, when analyzing the effects of laser energy in LIBS, it is important to consider the wavelength and pulse duration of the laser. Generally, nanosecond pulse duration lower repetition rate, and higher wavelength produce higher laser pulse energy. High laser pulse energy can also increase background spectral emissions. Overall, the rate of ablation and the amount of mass ejected is dependent on laser pulse energy [53].

The latter side of a typical LIBS setup is the detection side; which consists of the fiber optic probe, spectrometer, detector, and a computer. The fiber optic probe, consisting of FOC, used to collect plasma light generated on a sample, especially when the spectrometer cannot simply be placed in a feasible location for collection. FOC transmit the collected light using total internal reflection. Figure 2.6 shows a general design for an FOC. The core's diameter ranges from 50 um to 1 mm for ones made of fused silica. The cladding is made of low refractive index when compared to the core to help guide the collected light. The buffer is a protective barrier that keeps the cladding from damage. The spectrometer is a device that separated the individual wavelengths within the collected plasma light through a diffraction grating. The most commonly used spectrometers are the Echelle spectrometer and the Czerny-Turner spectrometer. The spectrometer used for the experiments in this work is based on the principles of the Czerny-Turner spectrometer. The Czerny-Turner spectrometer has an entrance slit with two mirrors and a diffraction grating. The first mirror directs the light to the grating while the second mirror directs the wavelengths reflected from the grating to the detector. The detector is a device that breaks down the spatial information of the light reflected for the spectrometer grating. There are various types of detectors, but the most common are charged coupled devices (CCD) and intensified charge coupled devices (ICCD). This work uses a complementary metal oxide semiconductor (CMOS) detector. Figure 2.7 compares the basic operating principles of CMOS and CCD style detectors. Unlike the CCD or ICCD, the CMOS require less power and are considered more efficient in high speed image processing [54]. The basic of the

detector are that photons from collected light are converted to electrons and stored in potential wells to generate digital information. [13, 16, 52].

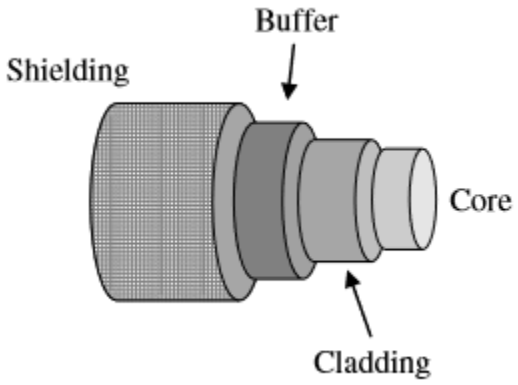

Figure 2.6 Fiber optic design. Reprinted from [13]

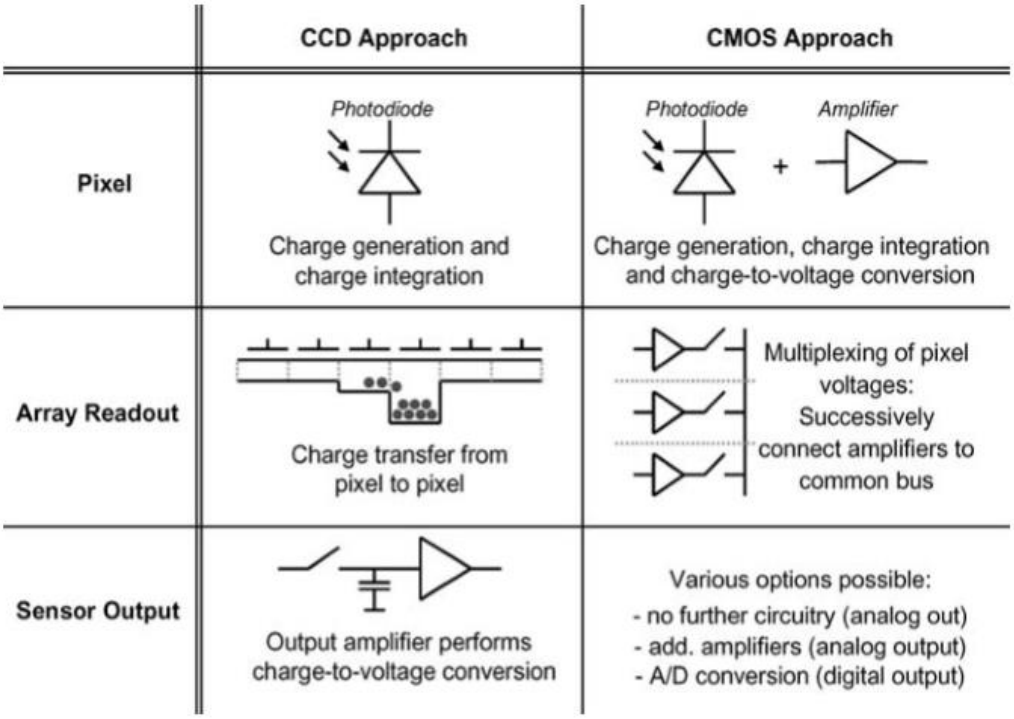

Figure 2.7 Comparison of CCD and CMOS detectors. Reprinted from [54]

2.1.5. LIBS in Solid and Liquid Media

LIBS in solid material have been a major area of study over the past few decades with many success and reproducibility when compared to its gaseous and aerosol counterparts. Many literatures have been successful in applying LIBS to various experiments of solid and liquid analysis.

Solid and liquid analysis with LIBS has been performed by many researchers over the years is a continuing interest [55]. Fitchet et al. [14, 56] focused on the detection of trace elements, submerged in different type of liquids for nuclear applications. This experiment utilized a Q-switched Nd:YAG 532-nm laser tilted at an angle on the liquid surface to detect various metal traces within the liquid sample. Cremers et al. [26] in 1984 used a 10-Hz repetition laser to observe the limit of detection for various elemental metals including aluminum in aqueous solutions. Zhang et al. [57] introduced a method for improving accuracy in LIBS liquid analysis by quantitively analyzing traces of chromium and sodium elements in an aqueous solution. This work utilized an Nd:YAG laser with up to 220-mJ of energy to interact with liquid samples injected into a mounted capillary. Bilge et al. [58] studied both solid and liquid phases of milk to target and analyze the limit of detection and limit of quantification for one of the nutritional elements, calcium.

Other studies have reported the use of LIBS in solid bulk concentrations of metals and metal alloys. In 2002, Melessanaki et al. [59] reported the use of LIBS analytical technique to extract historical and important inflation from archeological ceramics and metal artifacts. Using a 1064-nm Nd:YAG laser system as the ablation source, the group analyzed elemental structures of various metals and ceramics suffused with elements such

as copper, silver, gold, and tin. It has also been demonstrated that quantitative LIBS analysis can be extended to metallurgical purposes and the observation of arsenic concentrations in metallic artifacts [60], and studies of jewelry [61, 62]. Giakoumaki et al. [63] further report the use of LIBS for elemental analysis in archeological science areas and projects.

2.1.6. LIBS in Gas Phase and Aerosols

LIBS in aerosol can present unique problems generally not found in analysis of other media. This can partially be contributed to interference elemental substance in the gaseous state such as nitrogen, oxygen, and carbon; and the significant drop in number densities at the gaseous state for elements such as aluminum, copper and lead. These obstacles make it difficult to successfully detect and quantify the gaseous elements of samples of interest, however, there have been reported success of LIBS found in gas and aerosol media [24, 25, 48, 49, 64].

Aside from the problems mentioned earlier, the methodology of analyzing LIBS results in aerosol are unique as well. At low concentrations in ambient conditions, the hit efficiency by the laser pulse tend to be low. Furthermore, there can be a large variation in the noise to signal ratio from pulse to pulse, making it difficult to simply average hundreds and thousands of spectra together as was historically done. With this method, it is extremely difficult to accurately quantify the results due to low signals or domination of background noise. To increase the accuracy and reliability of aerosol sampling, strategies were implemented, most of which were used in the reference earlier mentioned in this subsection. A conditional pulse to pulse analytical technique for aerosol sampling was

suggested [16, 65]. The theme is to create a feasible threshold criterion for considering relatively spectral noise when compared to the spectra of interest.

2.2. High-Repetition-Rate Lasers for LIBS

2.2.1. Recent Developments of Pulse-Burst Lasers

The rise of pulse-burst lasers began in the earlier 2000s [32, 37]. The general objective was to develop a high-pulse-energy laser system to capture high-speed and turbulent flow structure. To achieve this, higher repetition rate lasers in the kHz and MHz range were needed to capture the evolution of reactions in time. However, conventional pulse laser had many limitations when attempts were made to stretch capabilities. When commercially available laser systems such as the 10-Hz, 1.5-J/pulse Nd:YAG system were ran in a megahertz range continuously, thermal loading limits the output energy to approximately 150-μJ per pulse. This energy output was too low to be utilized in high - speed flow applications and Imaging. Therefore, the burst concept was created to reduce the duty cycle of the laser while increasing the energy output through pulse energy amplification. Figure 2.8 displays a general concept of the pulse-burst laser system.

Figure 2.8 Basic outline of a pulse-burst laser system. Reprinted from [37]

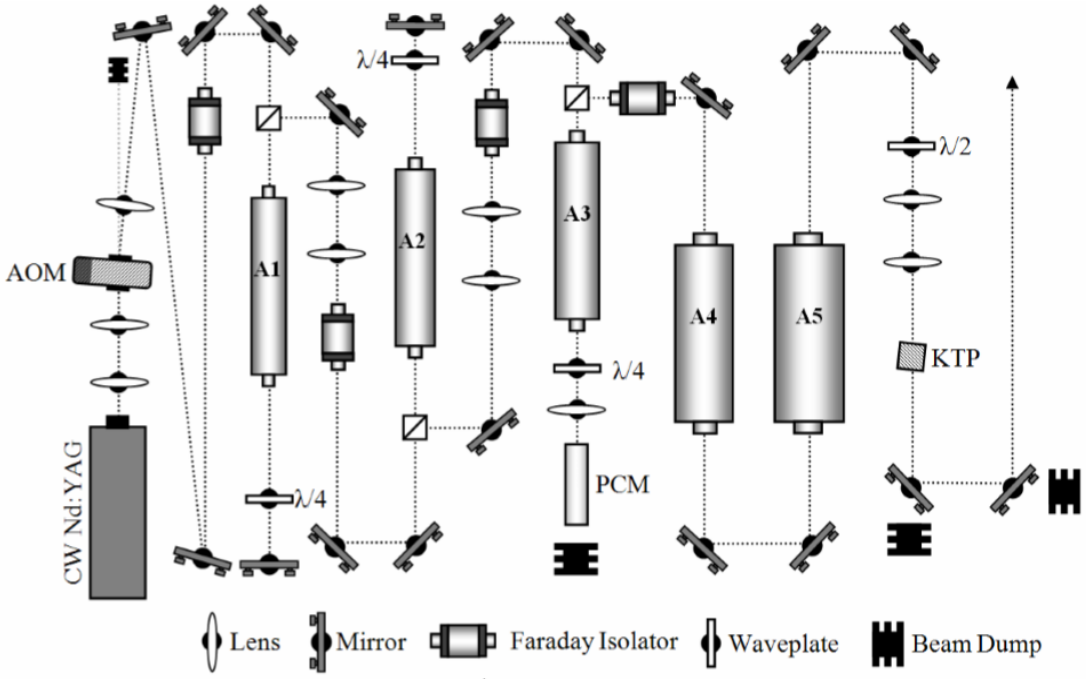

Figure 2.9 3rd generation pulse-burst laser system configuration for 532 nm output. Reprinted from [33]

2.2.2. Major Components of the Pulse-Burst Laser

Figure 2.9 details the modern general configuration of a Pulse-Burst Laser. The system is classified as master oscillator power amplifier (MOPA). In this system, burst of low energy pulse are served through multiple amplifiers. The first part of this system is a low power, continuous wave (CW) Nd:YAG laser operating on a single mode output at 1064 nm. The Nd-YAG is consider the master oscillator.

The master oscillator is then directed through the pulse slicer which then generates burst of pulses. There are two main types of pulse slicer; the Acousto-Optic Modulator (AOM) and the Electro-Optic Modulator (EOM). Both can create varying number of pulses with repetition rate up to tens of MHz and pulse duration as short as 10ns. The EOM uses electro optic Pockels cell and polarizing optics to rapidly manipulate the output

rate of pulses. AOM uses diffraction where the movement of acoustic wave through a crystal help generate an incident light that is then diffracted. AOM are also known as Bragg cells. Although slower, AOMs are generally preferred over EOMs due to cost and reliability concerns [66].

The rapid division of pulses through the pulse slicer causes a significant drop in pulse energies and so, the low energy pulses are moved through stages of amplification. The 3rd generation featured five amplifiers with rod diameters of 4,5, 6.3, 9.5 and 12.7-mm respectively. As described by Thurow et.al [33] the first 3 amplifiers maximized gain while the latter two prevented the loss of gain in addition to the Faraday isolators; which were designed to reduce the amount of gain loss between each amplifier stage.

The final stage is the frequency double stage in which the 1064-nm is filtered through a doubling crystal to output 532-nm wavelength. In this work, the doubling stage was not implemented, rather the 1064-nm wavelength was deemed sufficient for the parameters of the experiment. The work by Thurow et.al explored the generation of pulse trains in excess of 100 pulses. The work explained that the number of pulses used for experimentation was dependent on the capture capacity of detectors and high-speed cameras.

2.2.3. Applications and Evolution of Pulse-Burst Laser Systems

Over the past decade, pulse-burst lasers have proven to be effective in Thomson scattering [67-69] high-speed flow visualization [70-72], high speed time-resolved particle image velocimetry (PIV) [73], planar laser- induced fluorescence (PLIF) [44, 45, 74], and planar Doppler velocimetry (PDV) [75].

In the Thomson scattering works, it was demonstrated that a 15 pulse, 2-J per pulse at 1064-nm burst train on the order of repetition rate from 1–12.5-kHz can be used in Madison symmetric torus reversed-field pinch to capture the evolution of electron temperature profile and fluctuations.

High-speed flow visualization capabilities were first demonstrated in 2000 [32, 37] with a frequency-doubled laser producing a burst of more than 30 pulse with an average laser pulse energy up to 70-mJ at 1-MHz to visualize shock and boundary layer evolution in a supersonic flow. A similar experimentation was conducted with a 1064 nm laser system that generated burst of up to 99 pulses in a Mach 2.5 flow at 500 kHz repetition rate. In other works, 3-d flow visualization capabilities were realized in turbulent jets with the pulse-burst laser produce burst up to 100 pulses and beyond [71, 76]. In work involving S. Roy et.al [70], a 1064-nm pulse burst laser with approximate 100-ps pulse duration over 10-ms burst duration, operating between 10-kHz and 1-MHz and producing 10 to 10,00 laser pulses was used to gather time resolve measurements such as velocity in turbulent high-speed reacting flows.

PIV potential was demonstrated using a 20-kHz repetition rate burst mode laser that outputs 100 pulses every 12 seconds at 532-nm to examine turbulent fluid dynamics and exothermic reactions. In a high-speed trans-sonic wind tunnel experiment, the operating condition for the laser was up to 10.2-ms burst duration at 5–500-kHz every 8 seconds to gather dynamic measurement over a rectangular cavity.

PLIF experiments featured the use of pulse-burst systems in a Mach 10 hypersonic wind tunnel, turbulent flames. In the wind tunnel the laser generated 16–20 pulses in a

burst at 500-kHz to analyze Nitric Oxide dynamics in hypersonic flows. The turbulent flame works used a pulse-burst at 355-nm, operating at 10-kHz and outputting approximately 100-mJ/pulse.

Brian et.al explored the potential of temporally resolved PDV potential using a 10-ns, 250-kHz repetition rate laser that generated 28 pulse with an average energy of approximately 1-mJ/pulse at the second harmonic stage (532-nm).

The versatility of pulse-burst lasers is vast. For this work, a custom pulse-burst laser will be employed. Table 2.1. Details the basic parameter of the laser used in this work, and Figure 2.10 displays the pulse to pulse data of the laser. It was confirmed that the first and last few pulses induce weak plasma, however the remaining pulses where substance at a constant amplitude with minimal pulse to pulse variation pulse. It was therefore concluded that those pulses will not have any considerable effect on the LIBS studies and results. Approximately 970 pulses were analyzed and averaged for each experimental run. Figure 2.10 shows the average normalized amplitude over 970 pulses in a single burst. A single burst is approximately 10-ms. The average confirms that there is little pulse to pulse beam signal variation of less than 5% being outputted by the laser. Preliminary laser pulse energy characterization was conducted to ensure that there was no drastic variation in pulse to pulse energy during the LIBS studies.

Table 2.1 Texas A&M University (TAMU) pulse burst laser parameters

	Pulse-Burst Capabilities at 532 nm	**Experimentation Parameters**
Wavelength	532 nm	1024 nm
Repetition Rate	10,100,1000 kHz	100 kHz
Energy/pulse	300 mJ,15 mJ,2 mJ	26 mJ–30 mJ
Number of Pulses	100,1000,1000	1000
Length of Burst	1 ms, 10 ms, 10 ms	10 ms

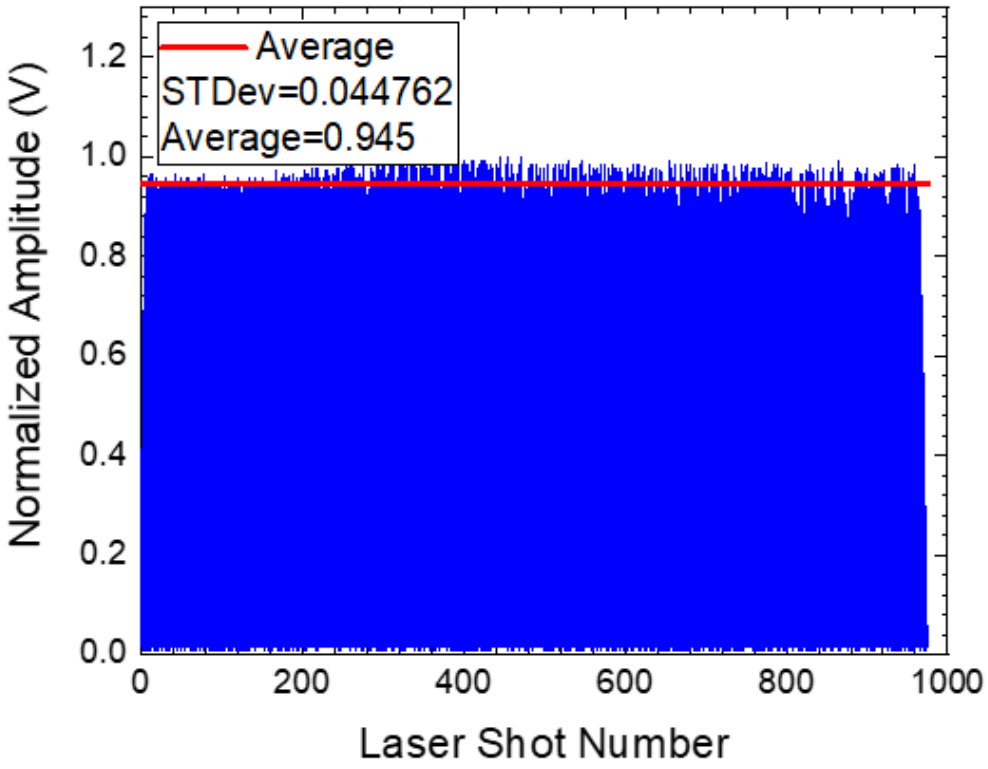

Figure 2.10 Signal of an individual pulse taken directly from the laser beam over 10-ms and recorded on a Lecroy 4-GHz, 40 GS/s oscilloscope

3. EXPERIMENTAL APPARATUS AND PROCEDURE

3.1. Experimental Apparatus

The energy source for the plasma generation is a custom designed 1064-nm nanosecond duration pulse-burst laser (Continuum). A schematic of the instrumental components of the laser and the experimental system is displayed in Figure 3.1. The laser is a megahertz repetition rate laser that outputs 1000 pulses in 10-ms. Figure 3.2 displays the concept of the pulse burst laser in which a series of approximately 1000 pulses is outputted every 5 seconds. This current experimental system set-up for all the experiments in this work were operated at 100-kHz repetition rate. The output beam diameter of the laser was approximately 5-mm with a pulse duration of 200-ns and a pulse to pulse width of 10-μs. The output beam was focused towards the location of the target using a +50-mm focal length plano-convex lens. The experiment samples were adjusted on a platform with two modes of movement, vertical and horizontal.

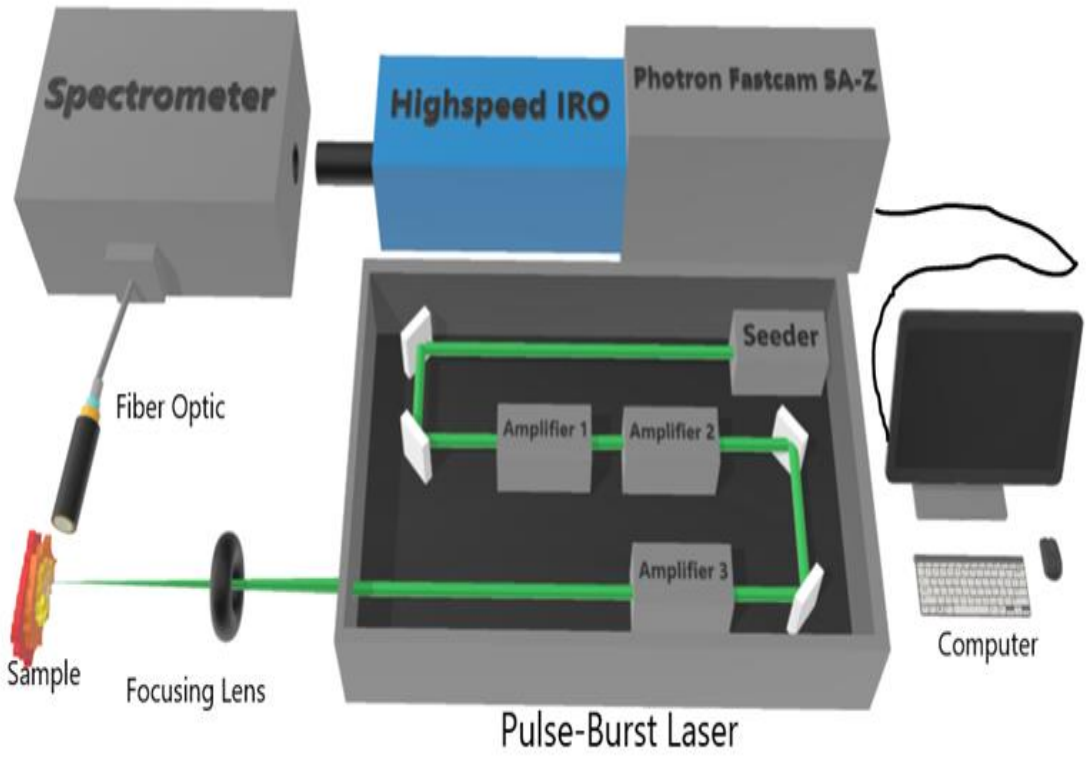

Figure 3.1 Pulse-burst laser and experimental apparatus: Emission side consists of the pulse burst laser and focusing lens. Detection side consists of spectrometer, intensifier, high speed camera, and fiber optic probe

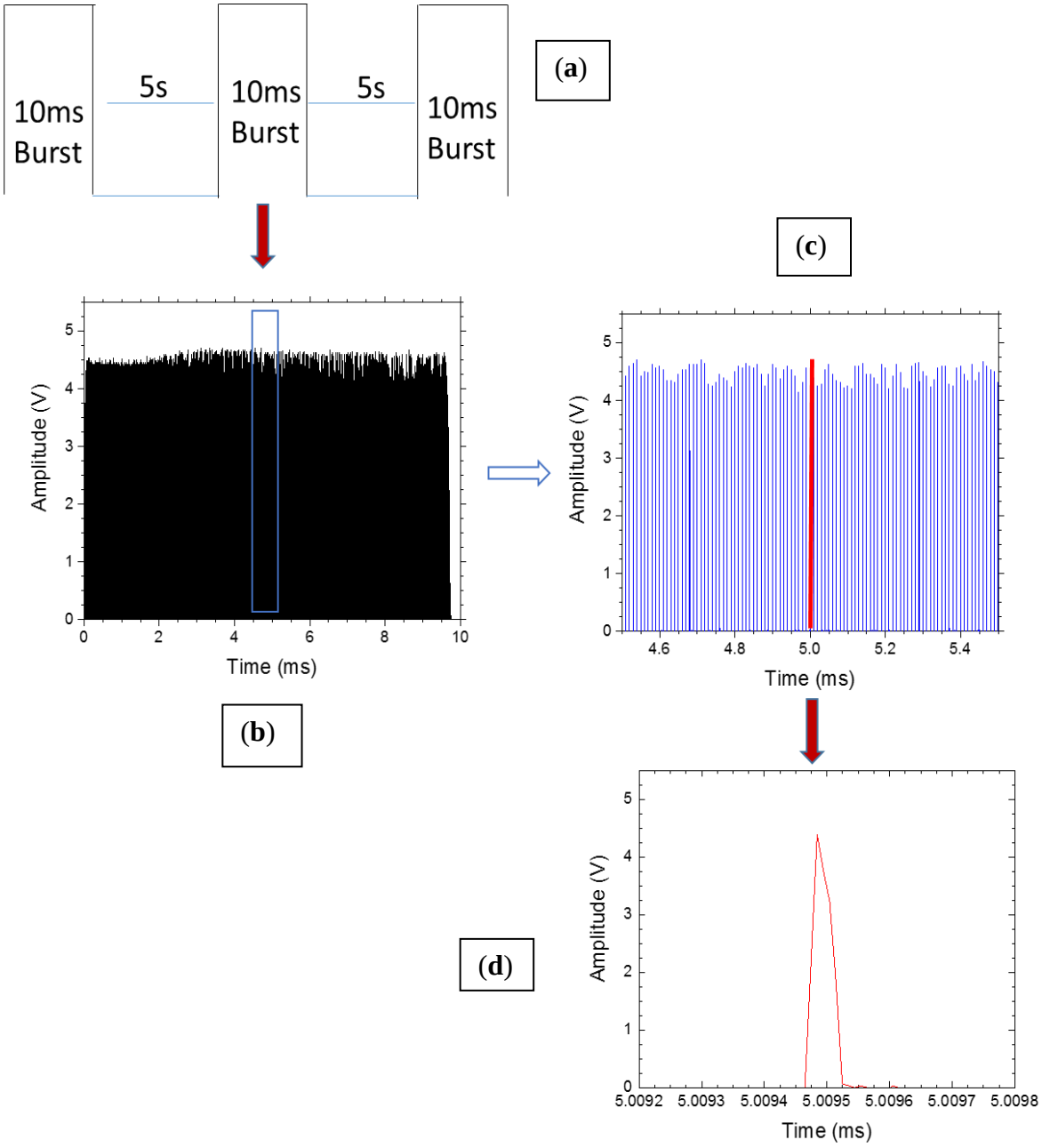

Figure 3.2 Burst schematic of pulse-burst laser: (a) Concept of pulse-burst laser. (b) Pulses within a sign burst. (c) Image of a few pulse within 1-ms of a burst. (d) Individual pulse at 5-ms of the burst with a pulse duration of 200 ns

The laser pulse signal intensities were captured and recorded with a photodiode (Thorlabs DET 10A) and recorded on a high definition oscilloscope (HDO 9404 Teledyne Lecroy). Initial observations of spectrums were recorded with an Ocean Optics Flame-S spectrometer (HR2000+). An image of the actual laboratory set-up for this work is displayed in Figure 3.3. To record the emission in higher resolutions, the spectrometer was switched out with a Princeton Instrument spectrometer (IsoPlane 160) with multiple grating capabilities. This work used 300-g/mm grating. Along with the spectrometer, the detection side included an intensifier (Lavision IRO S20/S25) coupled with Photron a high-speed camera (SA-Z) to retain sampling and detection speed that match the high repetition rate of the pulse-burst laser and allowed for gating time capabilities. The sample emissions generated from the plasma were collected by a fiber optic collimating lens probe which transmits to the Spectrometer to record the spectrum and intensity of the emissions. It is important to note that substantial amount of effort was placed in the assembly of the Isoplane 160 spectrometer, IRO intensifier, and the Photron high-speed camera as displayed in Figure 3.4. Reason being that the camera and intensifier are not exactly attached to the spectrometer but focus at a point to record the spectrum reflected spectrometer grating. This configuration reduces the signal captured by the camera, limits the wavelength window, and resolution of the spectra. Therefore, this system was optimized for signal detection. To rectify the limitations of spectra detection range, positioning calibration effects were made to record spectra from different samples containing Al, Cu, H, O, F, and C. All the elements and emission line wavelength focused on in this thesis are displayed in Table 3.1 along with the respective position optimal

detection. Each position allowed us to successful view the species spectrum within a 300 nm range. This allowed us to properly verify the accuracy of the recorded spectra captured by the camera and intensifier with previous recorded LIBS spectra from sources such as the National Institute of Standards and Technology (NIST).

Table 3.1 Elements of focus and camera position for optimal detection

Additive/Mixture	Chemical Formula	Emission Line of Focus (nm)	Position
Copper	Cu	511	1
Aluminum	Al	396.15	2
Lead	Pb	406	2
Hydrogen	H	656.2	3
Carbon	C	736.5	3
Fluorine	F	685.7	3
Oxygen	O	777	3

To remotely manage and control the gate, laser workload, and exposure level of the Intensifier-Camera, the communication between the detection side and the laser plasma emission were controlled by three Delay Generators (DG). The first DG was tuned to manage a consistent repetition rate of 100-kHz; and the second DG allow for us to set a burst interval of 0.2-Hz which means there is a burst of 1000 pulses every 5 seconds.

The third DG creates a direct communication between the power source and the detection side to ensure the appropriate gate delay time and exposure following the ablation and ionization stages.

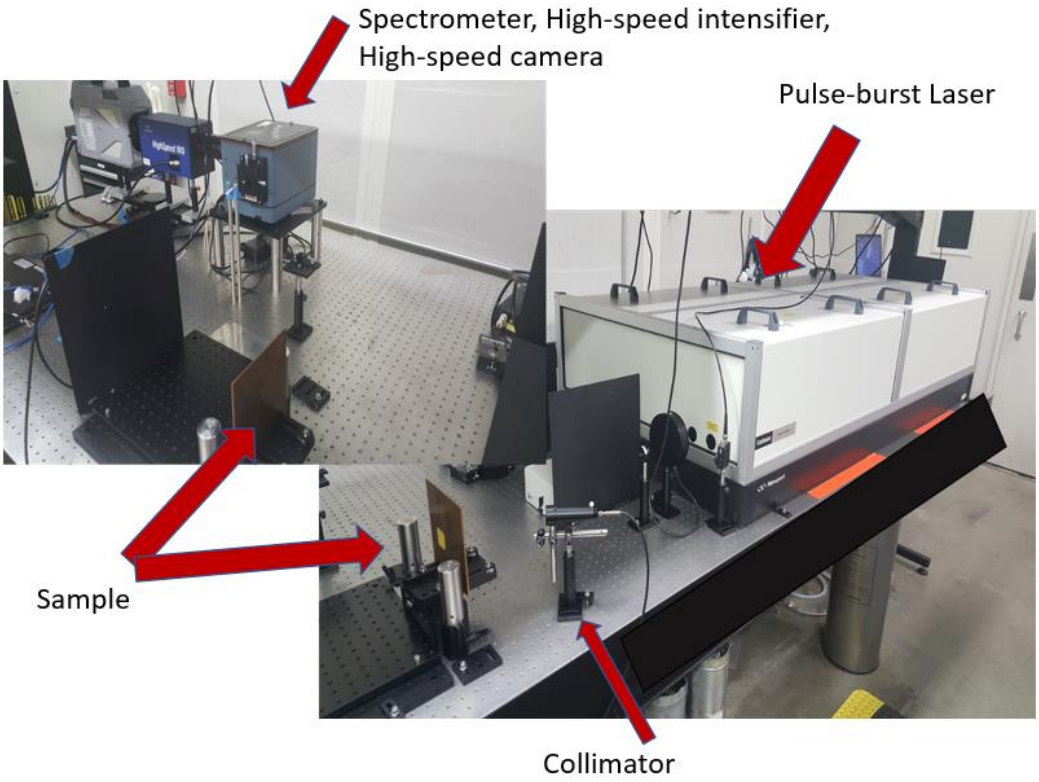

Figure 3.3 Photograph of the experimental apparatus of preliminary analysis with the pulse burst laser system, copper plate, and detection side equipment

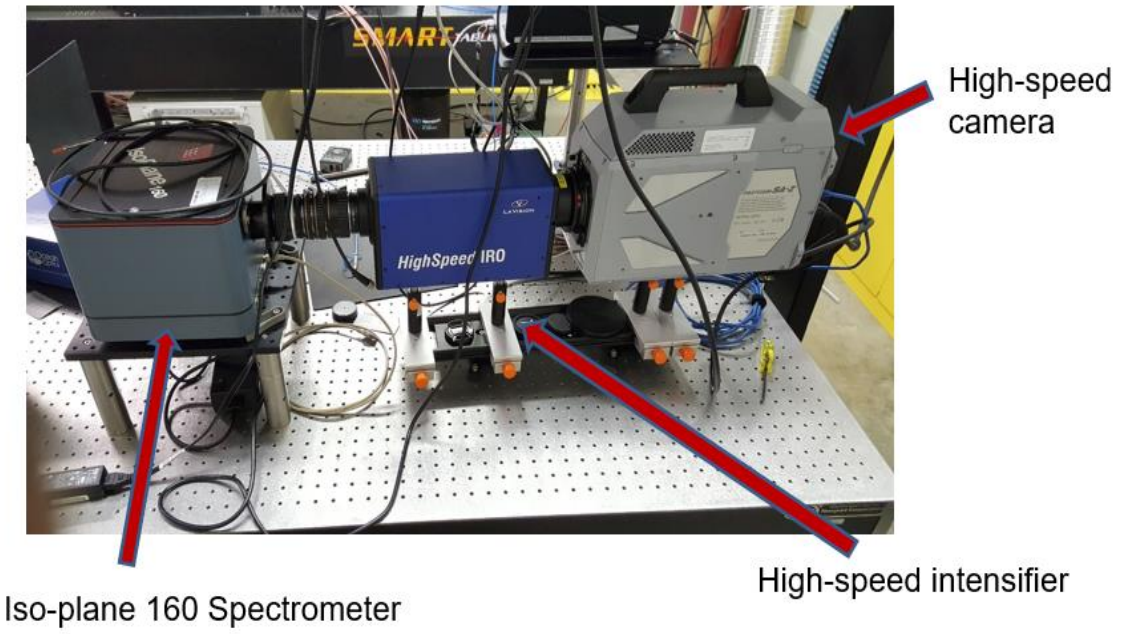

Figure 3.4 High-speed detection system set-up

3.1.1. Solid Samples Set-up

The preliminary experimental setup were bulk solid targets uniquely composed of Al, and Cu respectively were analyzed. The sample targets are displayed in Figure 3.5. The targets were placed at a focal length of 50-mm while fixed on an adjustable moving platform for position adjustment, both vertical and horizontal. The plasma emission was collected by an optical probe and the encoded material component spectra were sent a Flame -S spectrometer. The desired result of this preliminary experiment was to conduct a wavelength study to allow for accurate calibration of the ISO-plane 160 spectrometer, optimal gate delay studies, and characterization of laser pulse energy dependence for SNR studies. This is to acquire a rudimentary understanding of the pulse-burst laser for LIBS; particularly for the propellant experiments.

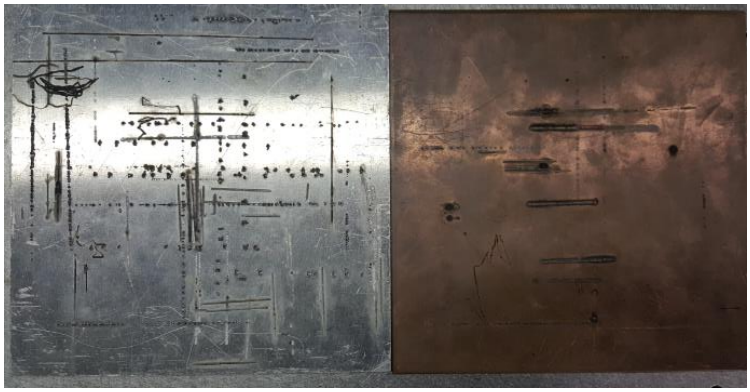

Figure 3.5 Preliminary experiment solid plate samples

3.1.2. Pressurized Aerosol Set-up

A quarter inch to 2.5-mm under-expanded nozzle was used to generate a high velocity air stream at room temperature at 110-psi. An aerosol diagnostic freeze spray from the company Techspray (Freezer) at a velocity of 10-m/s was then introduced to the stream at the outlet of the nozzle. The aerosol has a Tetrafluoroethane (CH_2FCF_3) chemical compound. The elemental composition consisting of carbon (C), fluorine (F), and hydrogen (H). Oxygen(O) were introduced to the mixture from the under-expanded nozzle air stream. A focal length of 50-mm was also used for this experiment. Image of the aerosol can is displayed in Figure 3.6

Figure 3.6 Image of the aerosol can used for the experiments

3.1.3. Propellant Samples Set-up

The propellant samples were fixed in a holder on a similar adjustable moving platform as the solid plate samples. This will help keep the flame zone breakdown within the area of interest. The propellants were manually lit with a handheld torch. To control the emission of fumes, a fume exhaust vent, place approximately 10 inches above the experiment zone, was designed to guide the emissions to prevent over exposure and inhalation of particle; which can potential be harmful.

The samples used for the propellant were carefully concocted and hand-mixed by Dr. Petersen's students, Katherine Dillier, Felix Rodriguez, and James Thomas ;following the procedures previously validated and expressed in works and publications [12, 77]. The samples were made with HTPB/AP composites as the baseline. Then small percentages of

additives containing metallic elements were mixed with the HTPB until fully coated. The samples are then allowed to cure. The samples are approximately 1.5 inches in length with burn times ranging from 20–30 seconds. Figure 3.7 shows the propellant strands with Teflon tubing (left) and without Teflon tubing (right), while Figure 3.8 displays an image of a burning propellant and the location in which the laser is focused. Table 3.2 details the additives and mixtures used for all experiments in this work, and their concentrations.

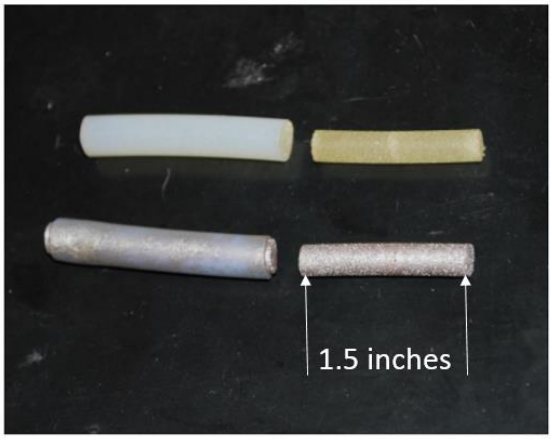

Figure 3.7 Image of the propellant samples

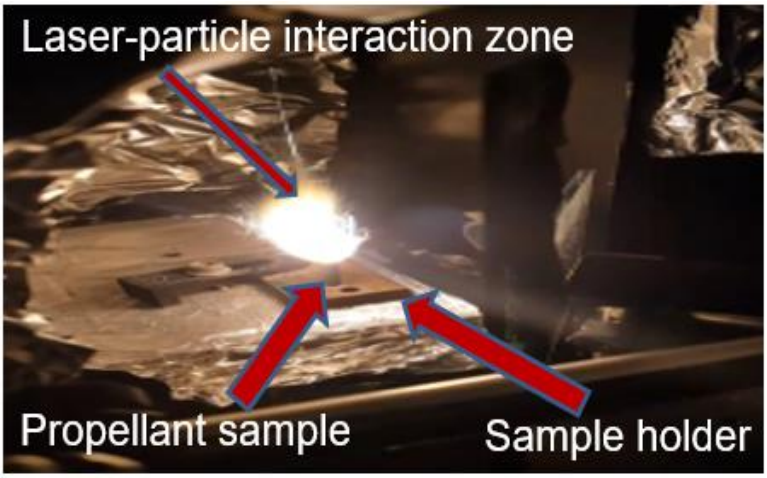

Figure 3.8 Photograph of the experimental propellant setup and in-experiment burning

Table 3.2 Propellant mixture samples used for experimentation

Additive/Mixture	Chemical Formula	Emission Line of Focus (nm)	Additive Concentration by Mass (%)	Number of Strands
Aluminum	Al	396.15	16	10
Aluminum	Al	396.15	10	10
Aluminum	Al	396.15	5	10
Lead	Pb	406	16	10
Lead Stearate	$(C_{17}H_{35}COO)_2Pb$	406 (Pb)	16	3
Tetrafluoroethane	CH_2FCF_3	656.2 (H) 685.7 (F) 736.5 (C) 777 (O)	unknown	N/A

3.2. Experimental Procedure

Prior to each set of experiments, the room temperature was set to approximately 20°C to maintain optimum operating conditions for the pulse-burst laser. Following the comprehensive guidelines in the standard operating procedures document for the TAMU pulse-burst laser, appropriate safety protocols are followed protective gear is donned, and the laser is turned on. The pulse shape and power are then measured for stability to ensure consistency in data collection. The pulse shape is measured on the Teledyne Lecroy

oscilloscope with the Thorlabs photodiode. The laser pulse energy was measure with an Ophir power meter (7Z02724).

Once it was confirmed that the laser safety parameters and optimum operating conditions were met, the laser power was reduced, and the shutter closed. The samples were then carefully place at the focal point for interaction as described in the "set-up" sections of each sample.

Next, the positioning and recalibration of the detection side for the respective species of interest. Since a high-speed detection system is not commercially available for high repetition rates elemental analysis and visualization, a custom high-speed detection system was constructed as displayed in Figure 3.4. Though the system was designed for high-speed analysis, there were some shortcomings in which the intensity was significantly affected. Therefore, the slit for the spectrometer was fully open to maximize optical power. Consequently, there was a reduction in resolution, resulting in detection width of the elemental emission lines as displayed in Figure 3.9 being wider than their natural widths. High spectra resolution was not a demand for this work thereby, low spectral resolution did not impede the analysis done in this work.

However, due to low spectra resolution, the spectra range of the spectrometer grating was significantly diminished and therefore three configuration positions were needed for optimal detection of all samples and elements of interests. The spectra range recorded on the detection system was approximately 200 nm. This range allow for accurate analysis of Cu (504-nm & 511-nm) emission lines at position 1, Al (396.15-nm) and Pb (406-nm) emission lines at position 2, and H (656.2-nm), F (685.7-nm), C (736.5-nm) and

O (777-nm) emission lines at position 3. Upon changing positions, the spectrometer was recalibrated with a Princeton Instruments neon-argon calibration lamp and then the spectra emission lines were compared to initial spectra taken from the flame-s miniature spectrometer at 1-ms integration time and the NIST database to ensure accuracy. Overall, the custom assembly was optimized for detection, sampling rate, and fast gating.

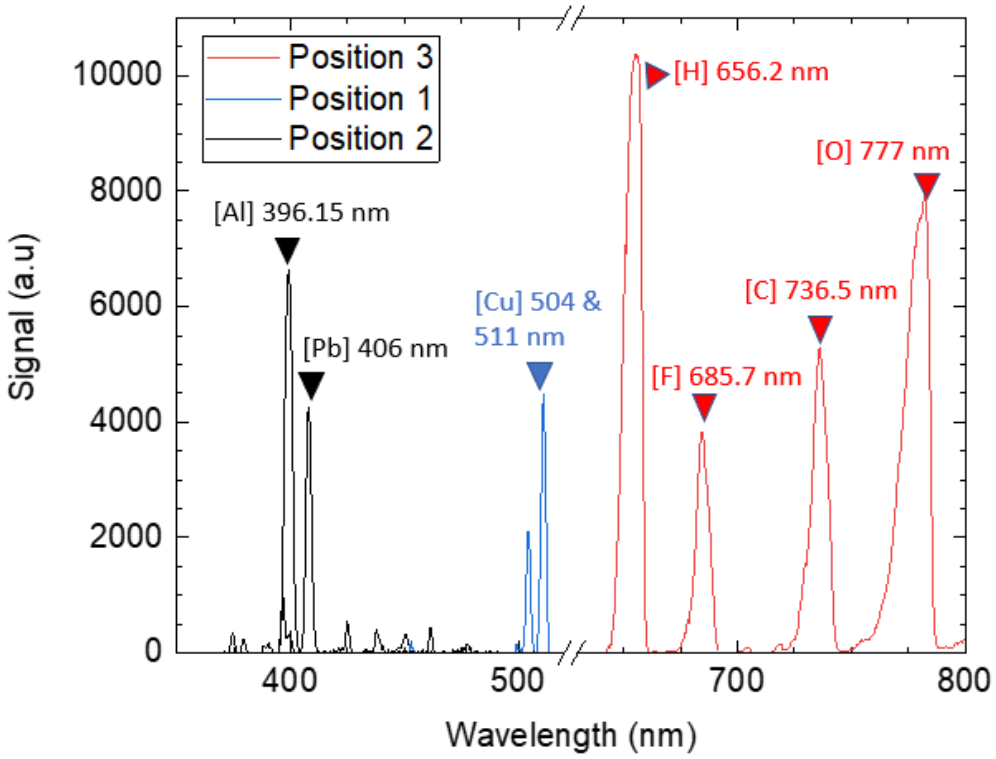

Figure 3.9 LIBS sample spectra of peaks detected from the different detection configurations

After the custom detection system was correctly configured, preliminary optimization experiments were conducted to increase sensitivity and accuracy of the LIBS analytical method. The main preliminary optimization is the Bremsstrahlung emission,

which is a continuum emission that radiate upon plasma generation [52, 78] . These radiations tend to hide emission peaks; therefore, it is important to collect data when the radiation is negligible in comparison to spectrum signal. To locate the point where the continuum radiation is negligible, an optimal delay scan must be performed. It is important to note that laser pulse energy, pulse duration, integration time, and data analysis methods are important parameter for optimization [52, 79]. Optimal gate delay time is often a function of all the parameters previously listed, therefore all parameters were studied and considered.

After the preliminary optimization studies were performed, the first analysis was performed on the solid plates to observe the laser-target interactions. The second analysis performed was on the aerosol sample to observe the dynamic behavior of particles moving in space. The final analysis focused on the propellant strands. The areas of study with the propellants were particle emission detection, propellant concentration study, and limit of detection analysis.

3.3. Data Analysis

When analyzing the propellant and high-speed aerosol data, conditional analysis method will be invoked to calculate the level of detection with each additive concentration limit of detection (LOD) [80].

$$\boldsymbol{LOD = \frac{3.3\sigma}{Slope}} \qquad \textbf{(2)}$$

In which σ is the standard error the regression.

To further attempt to analyze the actual concentration of a sample during reaction based on the calibration line developed form the conditional analysis method, the equation below [16]:

$$\boldsymbol{X_{true} = (X_{hits}) * \frac{total\ hits}{total\ pulses}} \quad \textbf{(3)}$$

In which X_{true} is the actual concentration of the sample, X_{hits} is the hit determine through the conditional analysis calibration curve, and the 'total hit' indicates all elemental particle hits within the reaction zone.

The equation w was used to determine X_{hits} of the elemental particle emission lines of focus.

$$\boldsymbol{X_{hits} = \frac{particle\ hits}{total\ pulses}} \quad (4)$$

Where 'particle hits' is the number of times the emission line of focus is deemed a hit based on the conditional analysis condition, and 'total pulse' is the amount of pulses within a burst.

The conditional analysis conditions are as followed:

1. Pre-selected number of pulses for analysis in each run.
    a. 1 burst (970 pulses).
2. Noise to signal threshold for particle hit consideration.
    a. Signal of emission line of focus is 120% above selected noise threshold near the emission line.

3. Total number of hits of all elemental particle hits must be at least 20 to be consider a usable dataset.

4. RESULTS AND DISCUSSION

4.1. Calibration Experiments

4.1.1. Line Verification and Laser Characterization

For the Al, C, F, H, O, and Pb elements, the encoded spectra associated with the elemental components were recorded to optimize and appropriately characterize the expected line spectra results. A characterization test of the emission lines was performed by recording the spectra lines with the Iso-plane spectrometer, IRO intensifier, and high-speed camera. This test was to properly ensure the correct calibration for the spectrometer and accurate positioning of the highspeed camera/intensifier. Figure 3.9 displayed the emission lines recorded at approximately 200-ns delay. The lines were then compared to the NIST atomic spectra data to verify close alignment [81]. The figure is a conglomerate of different elemental verification experiments. The reason being, that the camera can capture up to 200-nm wavelength is configured to acquire. Therefore, the positioning of the highspeed camera/IRO must be adjusted slightly to accurately capture a different range of wavelength. Position 1 was used for the laser characterization pulse energy study using Cu spectra. Position 2 was used for the detection of AL, and Pb in the propellants and solid plates. Position 3 was for the detection of the H, O, F, and C gases in the aerosol sprays. The peaks were in a reasonable confidence level of detection capabilities for different elemental composition both in the solid and gas phases and allowed for the experiments to proceed.

Following the emission line detection accuracy verification, a SNR study was performed by conducting a gate delay and laser- energy dependence study of Cu at 511-nm. Figure 4.1 displays the signal intensity data recorded as a function of laser energy with the error margins. The signals were recorded using the ISO-plane 160 spectrometer. Copper was used for this study because the S-25 IRO intensifier was utilized. This intensifier was readily available at the time of this study and has a higher sensitivity for the spectra emission ranges for copper. However, for the decay study it was more beneficial to use the aluminum spectra and the S-20 IRO, and the S-25 IRO intensifier for the copper spectra and the aerosol elemental spectra due to the efficiency of the intensifiers at those wavelength ranges. Appendix C displays the difference in efficiency between the S-20 and S-25 intensifier at different wavelength range. The data observed for from the decay study would be used as a gauge for the propellant tests. The specifications and relationship between the S-20 and S25 IRO intensifiers can be seen in Appendix C. The Cu emission line at 511-nm was chosen because of its high intensity compared to other copper line at 504-nm. The figure shows the peak intensity output of the Cu line at 511-nm at increasing power output from the laser system. There is an increasing correlation between the intensity and laser pulse energy. The overall intensity is the average of the 50 pulses from 100–150 laser shot numbers. Approximately 30–35-mJ per pulse from the laser is required to breakdown ambient air molecules, therefore the acceptable maximum laser pulse energy was 30-mJ/pulse. The selected laser pulse energy will allow for the best SNR while preventing the breakdown of air background interference within the test region.

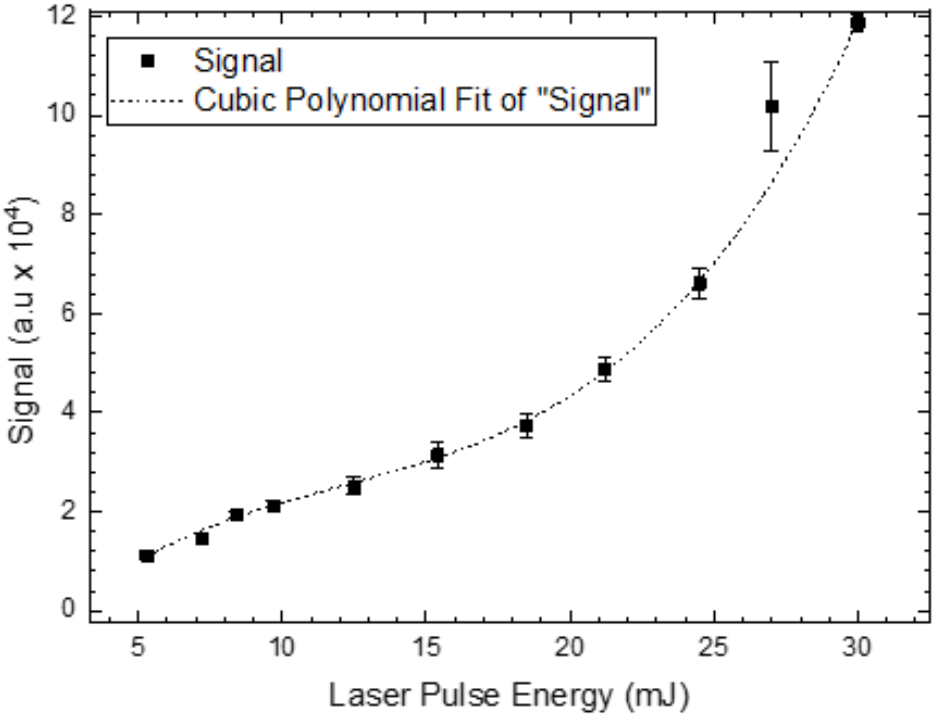

Figure 4.1 Laser energy dependence of the copper LIBS signal corresponding to the 511 nm emission line

4.1.2. Optimum Gate Delay Analysis

The next study conducted was to investigate and characterize pulse range and optimal delay time required for solid breakdown analysis. This study was conducted across various delay time from 0–5000-ns. An increase in delay time allows for us to reduce background spectrum to an acceptable level without sacrificing overall elemental emission spectra signal. The gate width for the Lavision high-speed IRO (S20) was 1000 ns. Figure 4.2 shows the relation between the Al 396.15-nm spectra emission intensity and the individual pulses within each burst of pulses. The data was repeated across various

delay times and shows that initial surface penetration and subsequent depth penetration of a stationary solid material affects the intensity of individual pulses. Although the target was translated after every burst to allow for optimal emission, due to the high repetition rate of the pulses it was difficult to move the target at a rate that match with 100-kHz repetition rate of the pulses. Consequently, the emission signal with respect to laser pulse shot is a function of the penetration depth of the target. The figure profile indicates that it requires approximately 10–50 pulses to remove the outward coating of the target and reach the bulk of the sample. Prime intensity was observed from approximately 100–200 laser pulse shots, and as laser pulse shots increase, the penetration depth increases due to continue ablation in a single space; resulting the Al emission decreases.

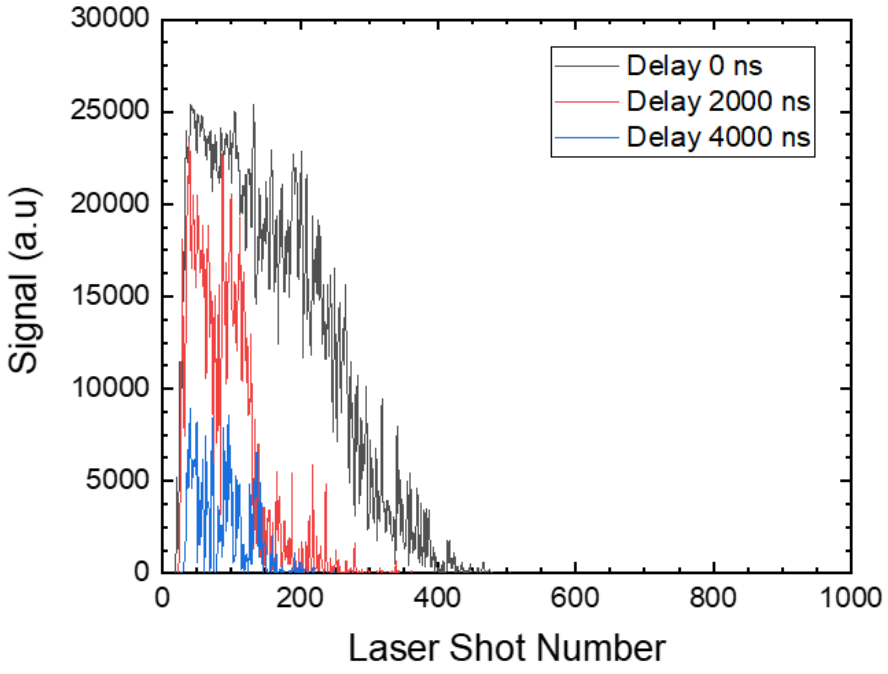

Figure 4.2 Signal of individual shot number within each burst train and the effect of penetration depth Al, 396.15 nm emission line, plate sample

The similar experiment was performed on a copper plate to confirm the results observe in the aluminum plate. The results are display in Figure 4.3.

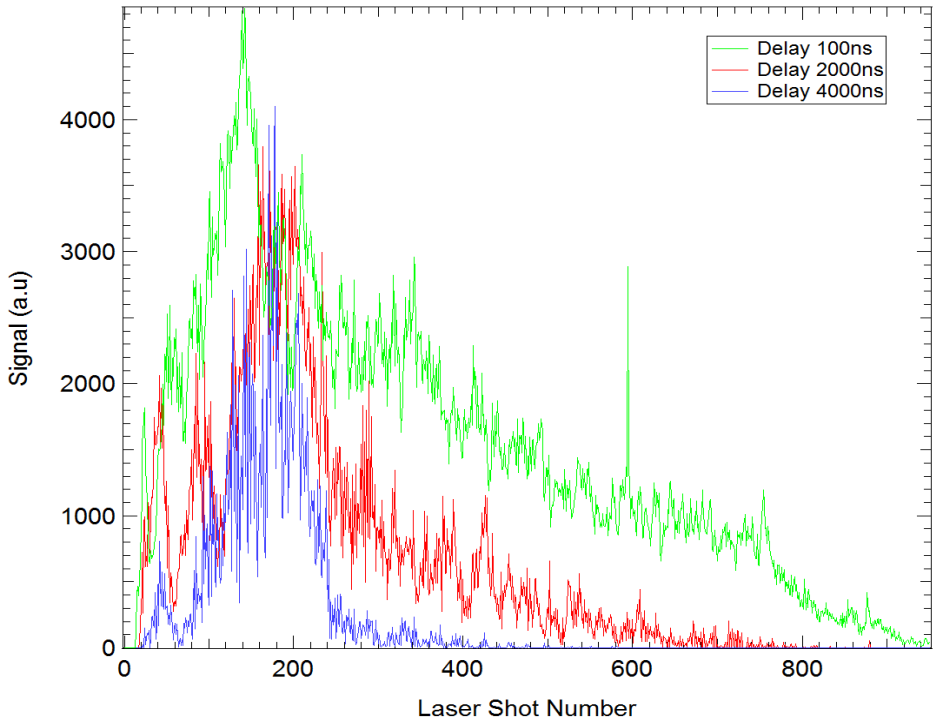

Figure 4.3 Signal of individual shot number within each burst train and the effect of penetration depth Cu, 511 nm emission line, plate sample

Figure 4.4 displays the normalized data observed from the plasma decay study. The data was observed across a time delay range from 0–5500-ns. A delay in collection gate allows for minimal collection intensity level of continuum background emission. At low detection gate delay thresholds, the plasma emissions are too great to ignore. As the detection delay gate increase there is an increase in the SNR. The target emission spectra are more defined as detection delay time was increased. However, beyond the optimal gate delay the overall target emission spectral will decrease as seen in Figure 4.4. The Al emission signal was observed from 394-nm to 398-nm while the background plasma

emission signal was recorded from 410-nm to 430-nm. From the figure, it was concluded that the optimal detection gate delays were approximately 150-ns. The study was recorded using the ISO-plane spectrometer and intensifier-camera (S20) with gain of 48 and a gate width of 1-ms. The spectra were integrated over the average of the first 200 pulses from within a burst.

4.2. High-Speed LIBS Measurement of Aerosols

Following the laser and detection characterization studies, an air stream coupled with a manually injected aerosol mixture plasma experiments was conducted. The purpose of this test was to observe the data gather from constantly moving target. This was the best

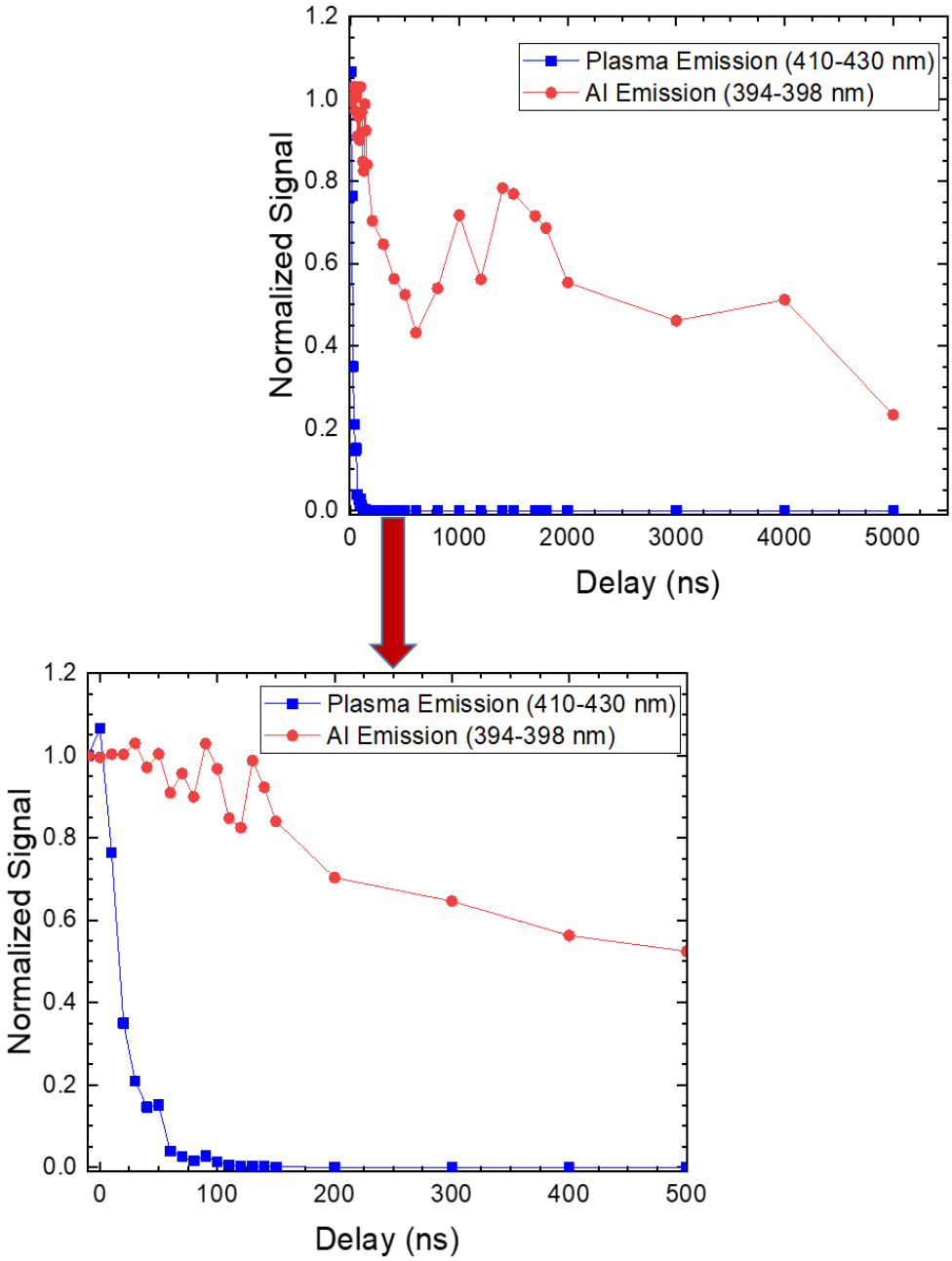

Figure 4.4 Al emission signal and plasma continuum emission as a function of capture gate delay

simulation that could mimic the release of particles from the propellant strands, and therefore allowed us to observe the relative signal behavior of fast-moving samples when compared to relatively slow bulk samples (plates from preliminary analysis). The air stream was fed though the under expanded nozzle at approximately 100 psi. The detection gate experiment was repeated. Similar to the solid plates, the background emission dissipated for the aerosol at approximately 150-ns, however at 1500-ns delay time, higher sigs were observed. Therefore 1500-ns was chosen as the delay time. It is important that this experiment did not exhibit much noise interference in the wavelength ranges that were focused on and therefore it was possible to use a non-gated approach. The energy chosen for the breakdown remained constant at 26-mJ/pulse. The gain increased to 67. The elemental focus of this study was the emission of hydrogen. From Figure 4.5, the detection of hydrogen, oxygen, carbon, and fluorine elemental emissions was achieved from the mixture Tetrafluoroethane (CH_2FCF_3).

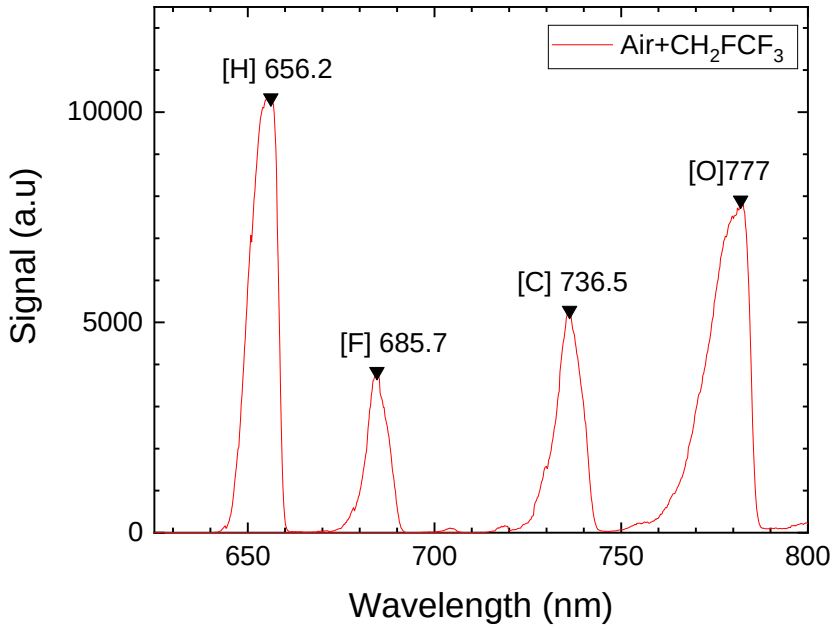

Figure 4.5 Signal recorded from 300-g/mm grating spectrometer and gated intensifier/high-speed camera of aerosol-freezer mixture in an open high-speed air stream

Similar to the propellant sample experiments, a signal pulse relation study was observed as shown in Figure 4.6 and the scatter plot in Figure 4.7. Figure 4.7 shows that with the pulse to pulse signal vary widely with a higher standard deviation variable when compared to the laser shot signal consistency. O'Niel et al. noted in his work that large variations in the signal pulses breakdown particles can be due to the difference in particle size, different elemental particles not being hit, the speed of the particles, or multiple particle being hit simultaneously [7].

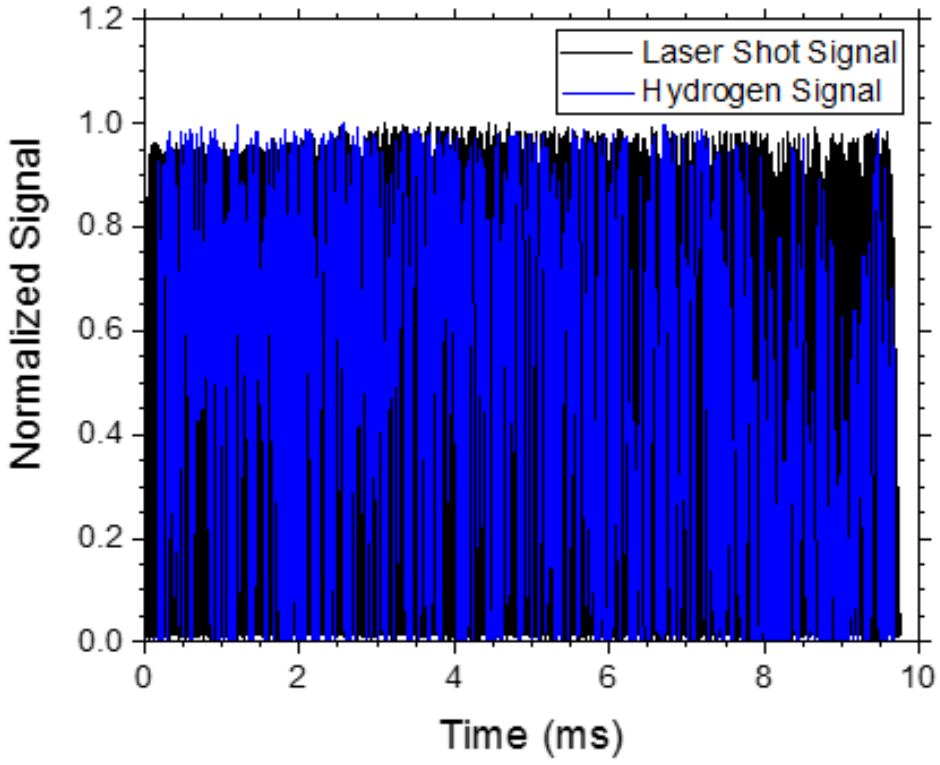

Figure 4.6 Signal of each individual H hits vs taken directly from the laser shots recorded on the oscilloscope. There is minimal pulse to pulse intensity variation. The average and STD were taken over 970 pulses

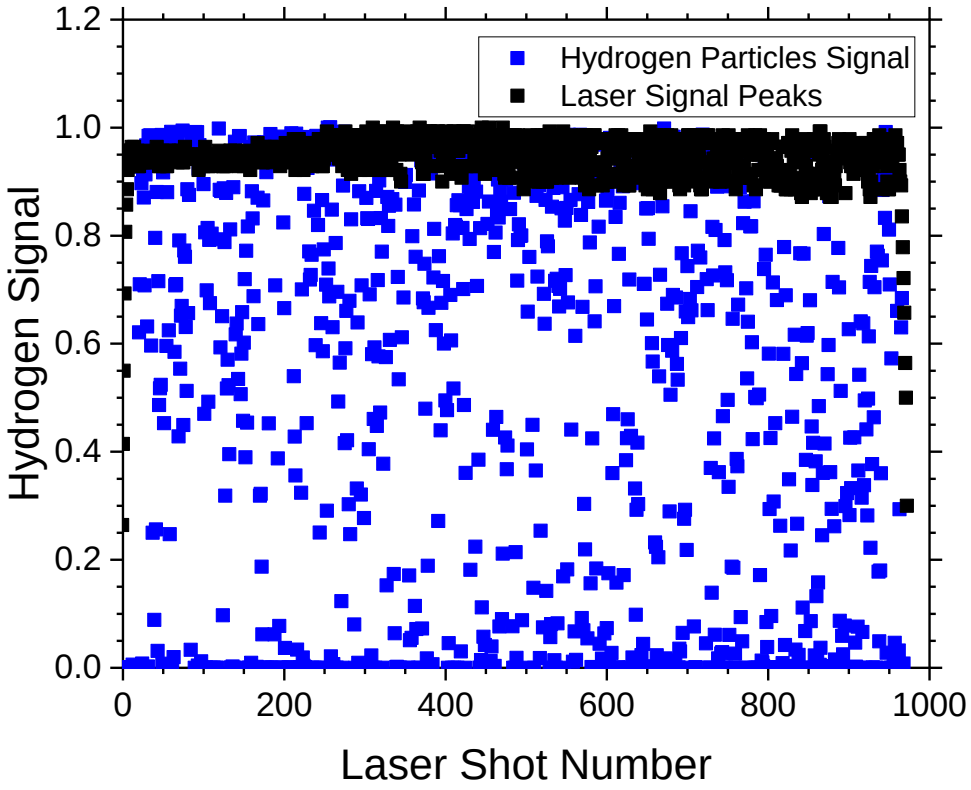

Figure 4.7 Scatter plot normalized signal of each individual H at 656.2 nm hits vs laser signal taken directly from the laser shots (970) peak intensity recorded on the oscilloscope. There is minimal pulse to pulse intensity variation on the laser signal but large variations with the emission signals

While we did not see the same penetration issues from earlier experiments, there is still a large pulse to pulse variation with confirmed that the pulses were hitting particles at different focal depths in the reaction zone. The further away from the focal point in which there is an interaction between the laser pulse and particle, the lower the signal intensity. The emission signal scatter plot was repeated for all elemental line emissions of

oxygen, carbon and fluorine. These plots are displayed in Figure 4.8, Figure 4.9, and Figure 4.10 respectively.

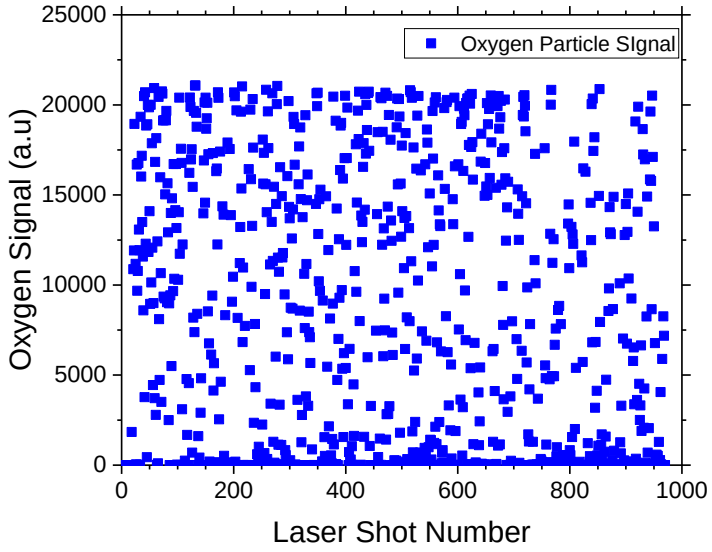

Figure 4.8 Scatter plot signal distribution of oxygen emission particle signals

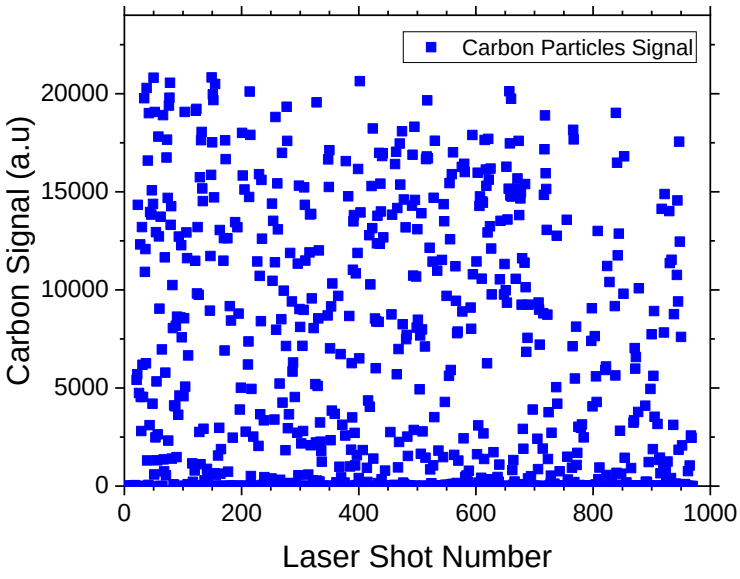

Figure 4.9 Scatter plot signal distribution of carbon emission particle signals

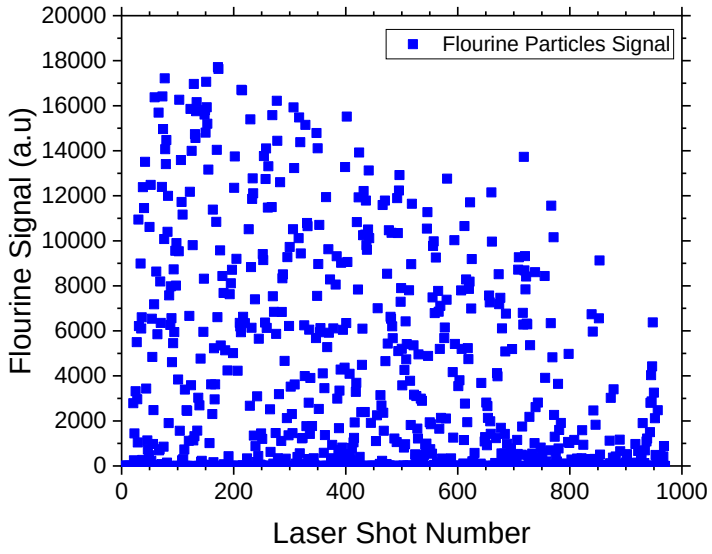

Figure 4.10 Scatter plot signal distribution of fluorine emission particle signals

Although, the figures above show that there is a completely random distribution of pulse signal that can potentially be attributed to many factors listed earlier, there seems to be a concentration cluster of signals across the plots. Therefore, a series of histograms as displayed in Figure 4.11, Figure 4.12, Figure 4.13, and Figure 4.14 were generated to better illustrate the concentration of elemental detection signals of hydrogen, oxygen, carbon and fluorine respectively within the aerosol sample. Since the concentration of the species within the CH_2FCF_3 is unknown, it was difficult to generate a calibration curve for particle concentration within the mixture. Therefore, the histograms were constructed with been sizes of 1000, and so the first 1000 will be considered the noise threshold or laser-particle interaction miss threshold for observing the relations between the elemental species.

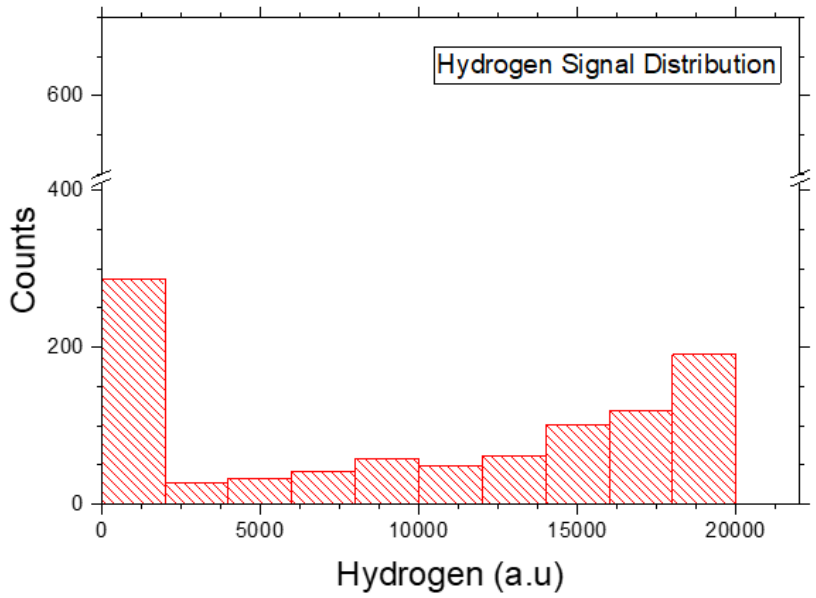

Figure 4.11 Histogram showing the signal distribution of hydrogen emission line from 1 burst, 970 pulses

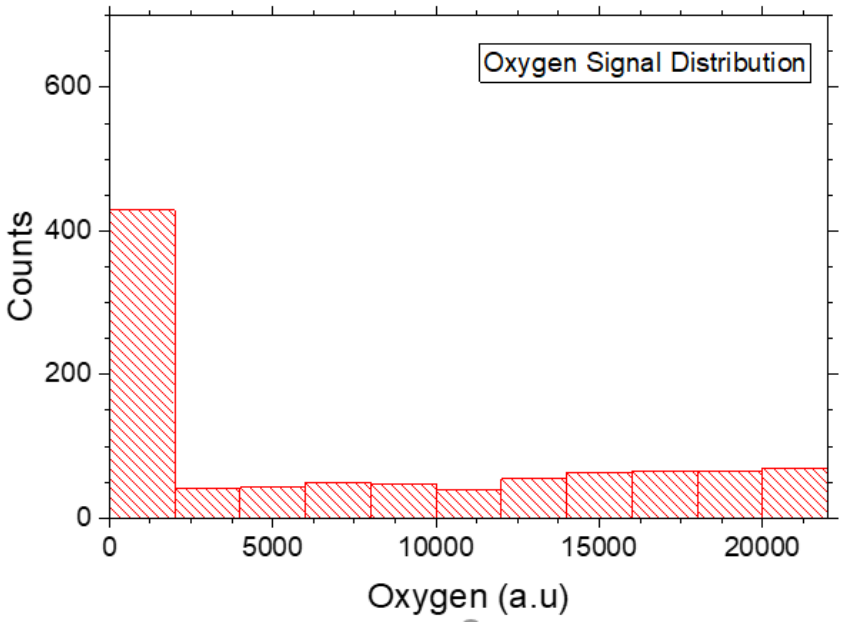

Figure 4.12 Histogram showing the signal distribution of oxygen emission line from 1 burst, 970 pulses

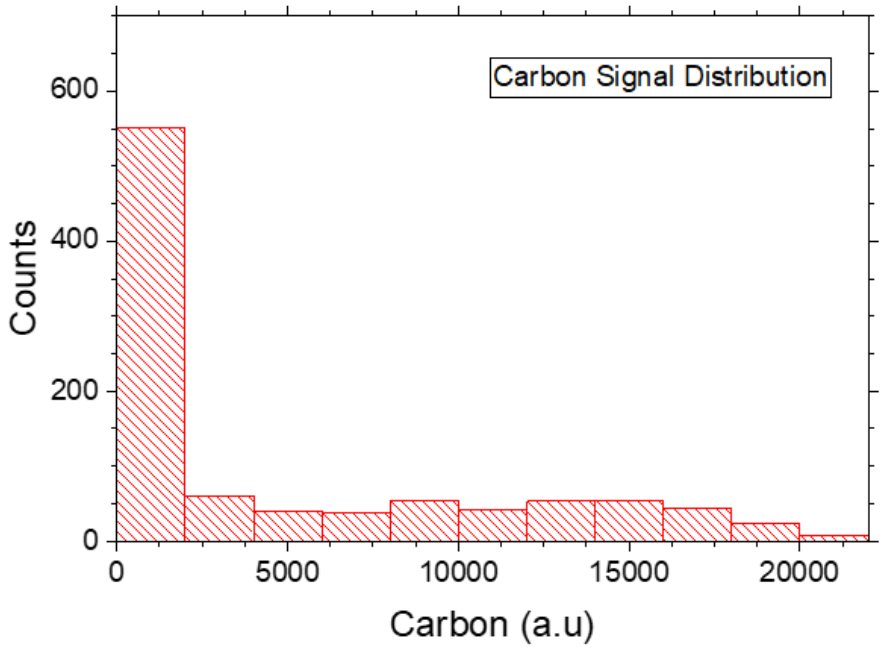

Figure 4.13 Histogram showing the signal distribution of carbon emission line from 1 burst, 970 pulses

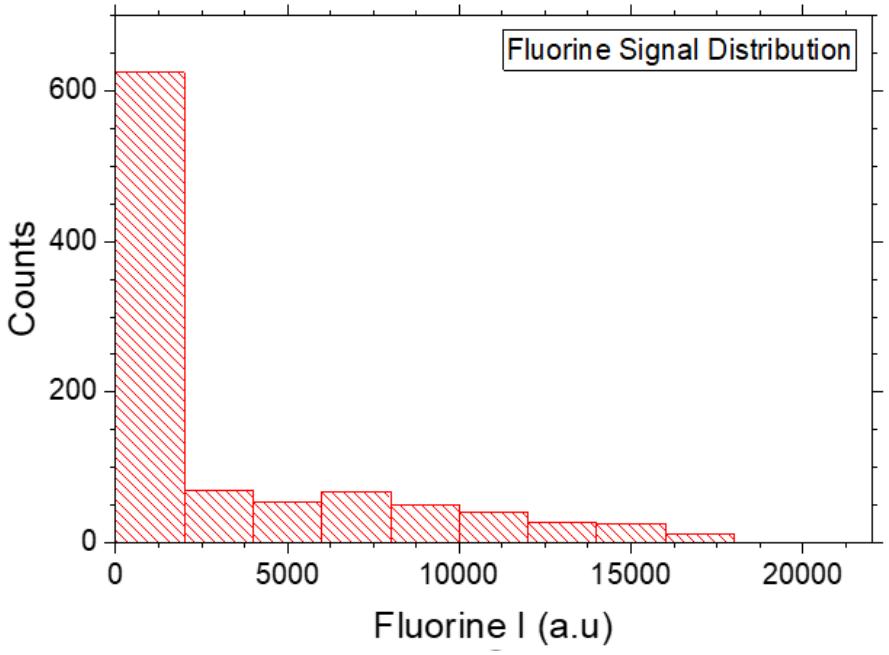

Figure 4.14 Histogram showing the signal distribution of fluorine emission line from 1 burst, 970 pulses

Although, the actual concentration of the aerosol sample mixture is unknown, the minimum to maximum achievable signals of all visible emission lines from the aerosol were in the same regimes and therefore an assumption was made that the concentration of particles within a signal intensity range corresponds to particle hits within the optimal detection range of the detector. From the figures, hydrogen has the most concentration at high signal levels from 15,000 to 20,000; followed by oxygen, carbon, and then fluorine inferred the emission. On the lower signal end hydrogen as the lowest concentration, followed by oxygen, carbon, and then fluorine with the highest concentration. Even though the observations were interesting, there was not enough information about the mixture being observed to derive a palpable conclusion about the individual behavior and the correlation between each emission line within the aerosol mixture. Though outside of the scope of this thesis, future experiments can be conducted to further analysis the behavior of gaseous compounds.

Within the scope of this thesis, the analysis observed with the pressurized aerosol sample helped us understand that there was no relationship between consequent laser shots and signal output when analyzing relatively fast-moving samples. However, it was not ruled out that the location of the particle within the reaction field can affect the signal recorded by the detector.

4.3. Propellants Study

Upon acquiring a basic understanding of the parameters (laser pulse energy, optimal gate delay time) needed to successfully apply LIBS to airborne micro-particles (~24 microns in diameter) release in propellants after being subjected to a combustion

process. All the propellant data for the Al concentrations and Pb concentration were test at 65 gain, gate width of 5 μs, gate time delay of 150 ns, and laser pulse energy of approximately 26 mJ. A sample spectrum from a 16% Al propellant strand was taken in Figure 4.15 and a sample spectrum of 16% Pb propellant was taken in Figure 4.16 This spectrum shows all emission line and ionizations can potentially be detected from each concentration of aluminum over each set of bursts. This spectrum was averaged over 970 pulses (1 burst). It is important to note that this figure was taken from one of the samples run to show all elements that can possibly be detected. These elemental peaks and ionization levels were also tested with the NIST LIBS emission spectrum database to ensure accuracy [81]. In most run, only the Al I line at 396.15-nm could be detected; this is acceptable because 396.15-nm is the target emission line of focus. Each propellant behave differently by slight margins, as is expected, because the flame reaction zone is considered a quasi-steady turbulent reaction. There are constant fluctuations in the behavior of the reaction, as there are rapid chemical reactions occurring through the entire burn process.

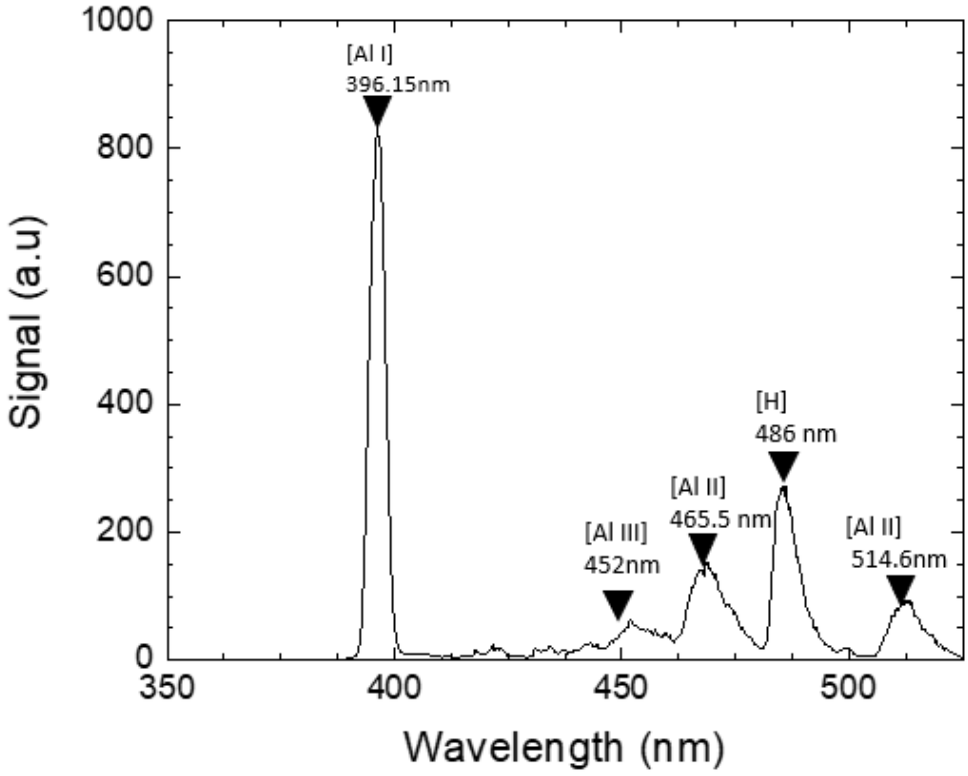

Figure 4.15 16% aluminum sample emission spectrum

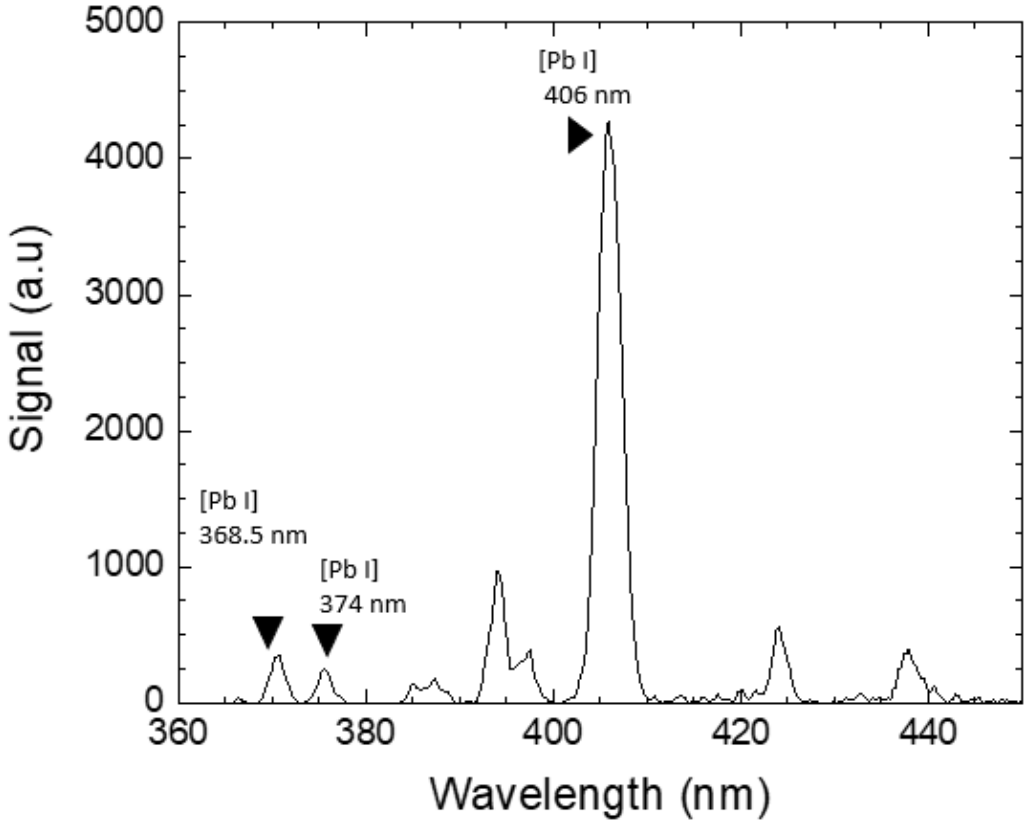

Figure 4.16 16% lead sample emission spectrum

Three bursts of data (2910 pulses) were taken from each propellant experiment burn. To observe the pulse to pulse variation changes from the raw laser output to the variation captured on the propellant strands, the Thorlabs photodiode was used to collect data from the raw laser pulse simultaneously with the Iso-plane spectrometer. Figure 4.17 displays the data collected on a normalized scale over the duration of one burst (10-ms) from one of the strand burns. Figure 4.18 further details the pulse to pulse fluctuation taken from one burst in a scatter plot. Appendix B includes 30 figures taken from 30 burst

from the 16% aluminum experiments. It is important to note that there are no notable patterns within each burst.

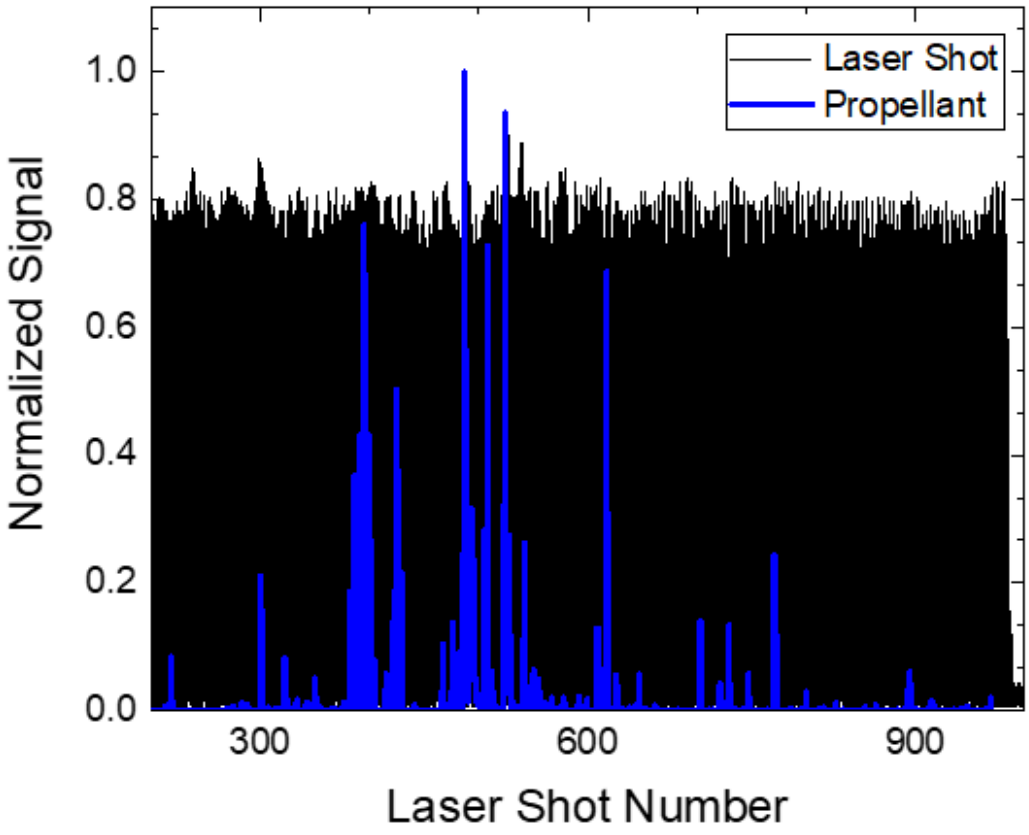

Figure 4.17 396.15 nm Al line detected signal vs raw laser pulse train

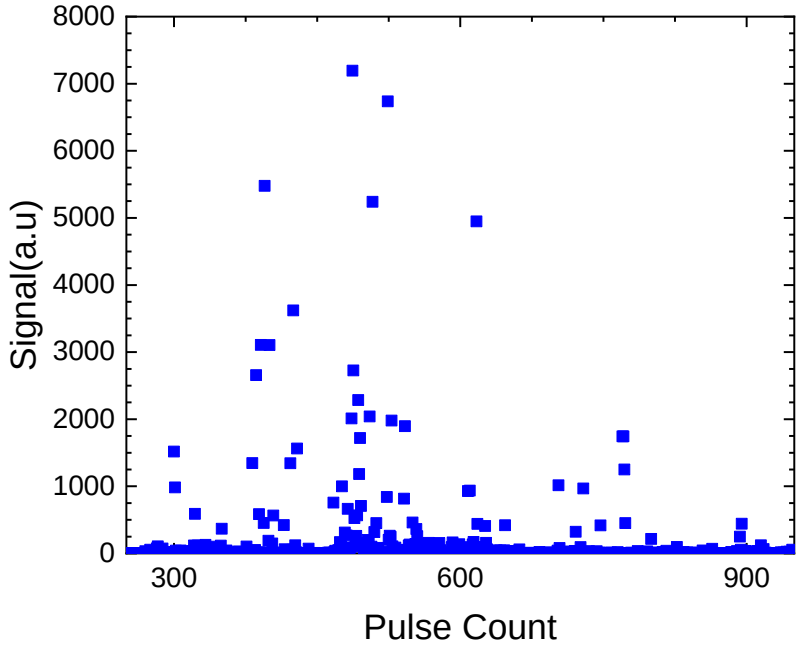

Figure 4.18 Scatter plot of 970 pulses with a burst for 396.15 nm line

From Figure 4.17 and Figure 4.18, it was concluded that because of the multi-directional movement, Al concentration, velocity of the particles, quasi-steady behavior of the reaction, and focus depth of particle location, the laser pulses miss or does not interact with most of the metallic particles being ejected from the propellant strand [7]. The analysis of all the possible catalysts for the pulse shape difference between laser and the propellant strand are especially difficult for this experiment because of the limitations of resources. However, previous work done by students in this lab have studied the movement speed and depth location of the ejected particles in space with Digital Inline Holography (DIH) using a 10-Hz Nd: YAG laser. Studying those work led to the prediction that the movement-speed and depth of interaction potentially contributes to the

large pulse to pulse intensity variation. The effect of depth/ particle location is also confirmed earlier in this section from the solid plate and aerosol sample experiments. Considering the pulse-burst laser was designed for high-speed flow analysis and visualization, the effect of velocity cannot be ruled out. The effects of velocity in is an area that can analyzed in the future.

The scope of this work did allow for propellant additive concentration studies to test the limit of detection (LOD) of the pulse-burst laser in the sample and generate a calibration curve for predictions of particle concentration in high-speed LIBS. Employing the strategies mention earlier in the literature review for the analysis of aerosol, a conditional analysis method will be used. The method suggests that rather than average all the spectra intensity to out the effects of concentration, it is preferred and more accurate to average the hits only. The hits are determined by setting a threshold and conditions that must be met between a pulse signal and noise. This method was chosen because there, is such a huge intensity fluctuation from pulse to pulse as discussed earlier. The conditions set for this experiment was that 30 bursts of data (29,100 total pulses) will be taken for each concentration, and from that the signal that can be considered as hits in each in pulse must be at least 120% greater than the background noise (410-nm–430-nm) signal. The ratio of total hits and total laser pulses will stand as the detection percentage from each concentration test

Figure 4.19 displays the detection percentage calculated for all concentrations of Al using the conditional analysis method. Figure 4.20 displays the percentage calculated with 16% aluminum as a baseline for present metallic particles. 16% aluminum will

remain the baseline to analyze other metallic components in lead samples as well. Table 4.1 breaks down the particle concentration with respect to 16% aluminum and the atomic mass of each metal.

Table 4.1 Breakdown of propellants studied and relative concentration to 16% aluminum

Additive	Additive concentration by Mass (%)	Metal Particle Concentration Relative to 16% Aluminum (%)
Aluminum	16	100
Aluminum	10	63
Aluminum	5	31
Lead	16	13
Lead Stearate	16	1

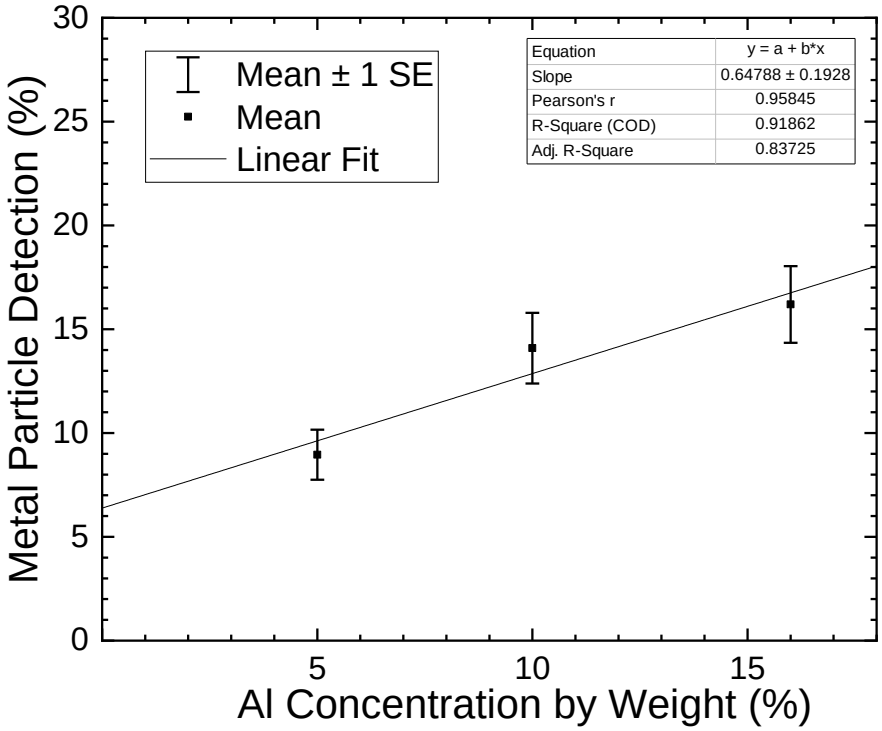

Figure 4.19 Detection percentage of Al particle hits over 90 bursts (30 for each concentration) and 87,300 total pulses with mean error bar

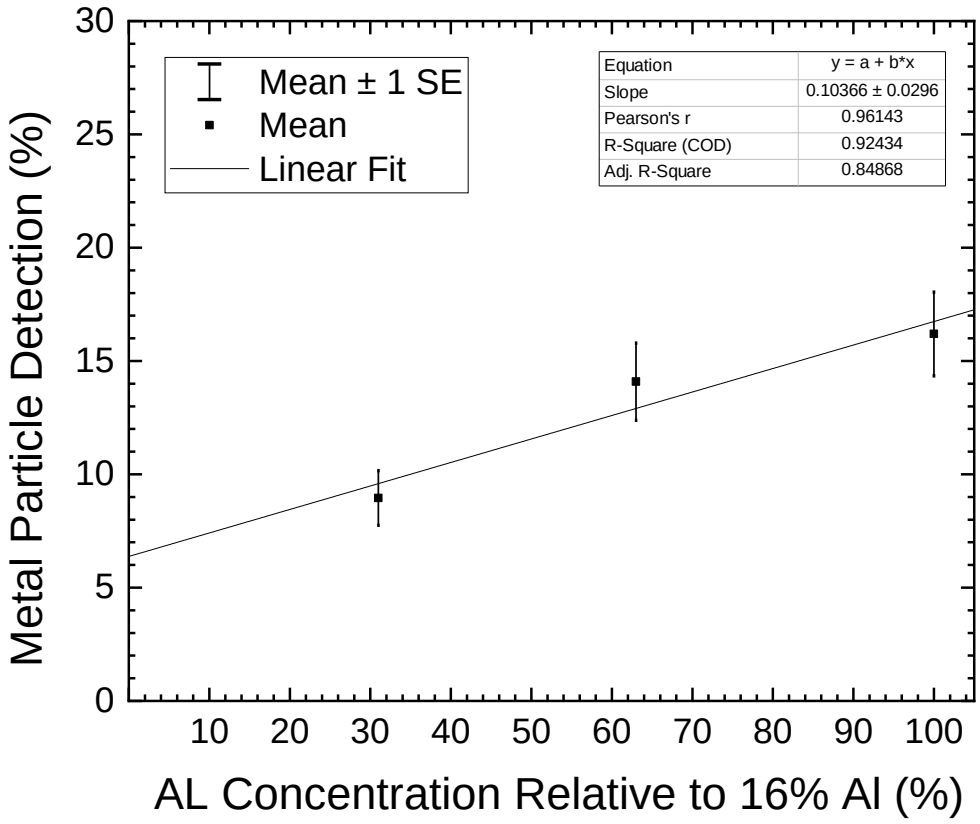

Figure 4.20 Detection percentage of Al particle hits over 90 bursts (30 for each concentration) and 87,300 total pulses with mean error bar with respect to 16% Aluminum

From Figure 4.19 and Figure 4.20, the LOD for aluminum concentrations were calculated to be 0.98% and 0.94% respectively. The results are relative and therefore enough to make a hypothesis that metallic particles less than 0.9 percent in relation to 16% aluminum as shown in Table 4.1 will not be detected by the pulse-burst laser. To test this hypothesis an experiment was conducted with the 16% lead propellant sticks, and another calibration line was plotted to check for correlation with the one from Figure 4.20. Figure

4.21 shows the result and calibration efforts for the lead propellants, which was calculated to be about 13% particle concentration by weight with respect to 16% Al.

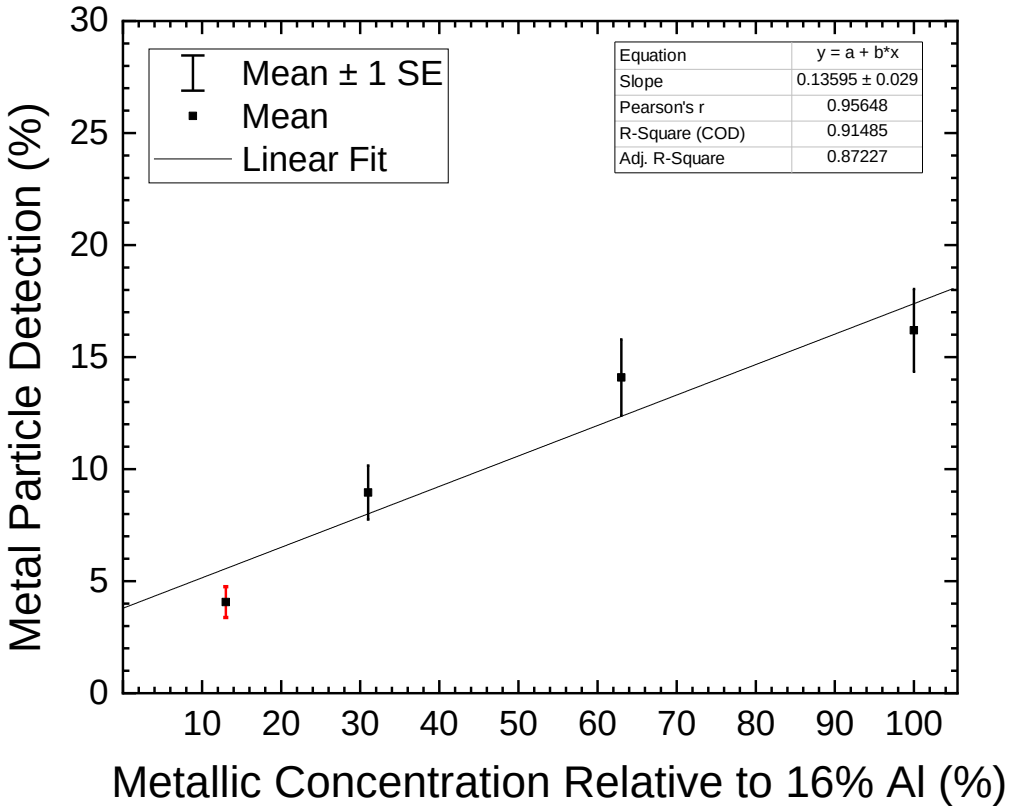

Figure 4.21 Detection percentage of Al particle hits over 120 bursts (40 for each concentration) with mean error bar with respect to 16% aluminum. The additon of the lead distribution is in red at approximatedly 13% of weight to the baseline Al

The calibration line here, from Figure 4.21, is different from that of Figure 4.19 and Figure 4.20 with the LOD being approximate 0.70%. Although smaller than 0.94% due to possible error margins with particle concentrations crossovers with different metal as they relate to 16% aluminum, the hypothesis still stands that particle less than 0.9%

concentration will be extremely difficult to detect. Therefore, the experiment proceeded to 16% lead stearate; which was calculated to contrail approximate 0.9 % metallic particle when weight with 16 aluminum by weight. The results seemed to align to the hypothesis as we did detect particles, however the detection percentage was near zero (0.2%) when compared to those of lead (4%), 5 % aluminum (9%), 10% aluminum (14%), and 16% aluminum (16%). This means the hit count for Pb particle hit in the lead stearate was on average 2 hits per burst (970 pulses). This is very little, and therefore any propellant experimentation with less than 1 % metallic concentration will has an extremely high probability of not being detected by the pulse burst laser. The results validated the earlier assumption that propellant with less than 0.9% will be extremely difficult to detect. The propellant section of this chapter has successfully proven that the pulse-burst laser can detect metallic concentration where a 10-Hz nanosecond failed, also the work also for a development of a calibration method for predicting the LOD for the pulse-laser and thereby paving the way to predicting particle concentration within a reaction zone of propellant combustion.

5. CONCLUSION AND RECOMMENDATIONS

5.1. Conclusion

100-kHz repetition rate LIBS with a pulse-burst laser was demonstrated for the first time. The laser characterization with the solid plate sample was successful in determined the optimum laser power, pulse signal behavior with depth, and the appropriate detection gate delay time. The laser energy dependence study suggested that approximately 26-mJ/pulse energy is allowable. The decay scans showed that a 150-ns gate delay time was optimal to eliminate the effects of background emissions. The calibrated emission line positions for the camera position from 1-3 agreed with the NIST spectra emission database.

The results from the preliminary analysis of metal plate samples and pressurized aerosol sample suggest the effects of depth penetration, movement speed, and depth location of species in relation to pulse-particle interactions and the detected signals. While the stationary plate samples suggest that subsequent pulses contributed to reduced signal, moving aerosol samples suggest there is no correlation.

The pulse-burst laser was successful in the fast sampling rate and detection of micro particles previous not detect by a 10-Hz nanosecond laser scheme, and a linear relationship was realized between the metallic concentration within the propellants and the amount of particle hits detected within the reaction region. Furthermore, LOD calibration was developed for future experiments with the pulse burst laser and particle released through combustion processes. It was also concluded that the 100-kHz repetition rate pulsed burst laser, from the results gathered from the pressurized aerosol and

propellant samples, is adequate in LIBS for applications geared towards detecting micro-sized fast-moving particles. This is significant because of the potential applications in ultra-fast reaction zones analysis of micro-particle agents released in short duration combustion reactions such as explosion and shockwaves.

5.2. Recommendations for Future Research

Further studies of the LOD of metallic particulates with the propellants can be conducted to verify the calibration data and investigate the detection limits of the pulse-burst laser and the current experimental parameters. The limits of the pressure-induced highspeed aerosol and the propellant samples experiment was that the effects of flow speed were not fully explored. An ultrasonic nebulizer-sample introduction can allow for the investigation of metallic additives such as Pb within the aerosol media. With the ultrasonic nebulizer, it is possible to investigate the effectiveness of the pulse-burst laser at different delivery speeds [82]. Furthermore, the coupling of the pulse-burst laser system with the DIH technique currently being investigated in our group, introduce promising possibilities of characterization of high-speed particle-laser interactions within the reaction region.

REFERENCES

1. López-López, M., et al., *An exploratory study of the potential of LIBS for visualizing gunshot residue patterns.* Forensic Science International, 2017. **273**: p. 124-131.
2. Lee, S.H., H. Thomas Hahn, and J. Yoh, *Towards a two-dimensional laser induced breakdown spectroscopy mapping of liquefied petroleum gas and electrolytic oxy-hydrogen flames*. Vol. 88. 2013. 63–68.
3. Stavropoulos, P., et al., *Quantitative local equivalence ratio determination in laminar premixed methane–air flames by laser induced breakdown spectroscopy (LIBS).* Chemical Physics Letters, 2005. **404**(4): p. 309-314.
4. Gottfried, J.L., et al., *Laser-induced breakdown spectroscopy for detection of explosives residues: a review of recent advances, challenges, and future prospects.* 2009. **395**(2): p. 283-300.
5. Lucia, F.C.D., J.L. Gottfried, and A.W. Miziolek, *Evaluation of femtosecond laser-induced breakdown spectroscopy for explosive residue detection.* Optics Express, 2009. **17**(2): p. 419-425.
6. Wang, Q.-Q., et al., *Detection of explosives with laser-induced breakdown spectroscopy.* 2012. **7**(6): p. 701-707.
7. O'Neil, M., et al., *Laser-induced-breakdown-spectroscopy-based detection of metal particles released into the air during combustion of solid propellants.* Applied Optics, 2018. **57**(8): p. 1910-1917.
8. O'Neil, M., et al., *Ultrashort-Pulse LIBS for Detecting Airborne Metal Particles from Energetic Material Reactions*. 2018. STu3N.3.
9. Carmicino, C. and A. Russo Sorge, *Experimental Investigation into the Effect of Solid-Fuel Additives on Hybrid Rocket Performance.* Journal of Propulsion and Power, 2014. **31**(2): p. 699-713.
10. Chaturvedi, S. and P.N. Dave, *Solid propellants: AP/HTPB composite propellants.* Arabian Journal of Chemistry, 2015.
11. Meda, L., et al., *Nano-aluminum as energetic material for rocket propellants.* Materials Science and Engineering: C, 2007. **27**(5): p. 1393-1396.
12. Stephens, M.A., et al., *Multi-Parameter Study of Nanoscale TiO2 and CeO2 Additives in Composite AP/HTPB Solid Propellants.* 2010. **35**(2): p. 143-152.
13. Cremers, D.A.R., L.J., *History*, in *Handbook of Laser-Induced Breakdown Spectroscopy*. 2006.
14. Fichet, P., et al., *Analysis by laser-induced breakdown spectroscopy of complex solids, liquids, and powders with an echelle spectrometer.* Applied Optics, 2003. **42**(30): p. 6029-6035.

15. Winefordner, J.D., et al., *Novel uses of lasers in atomic spectroscopy. Plenary Lecture.* Journal of Analytical Atomic Spectrometry, 2000. **15**(9): p. 1161-1189.

16. Thakur, S.N. and J.P. Singh, *Fundamentals of Laser Induced Breakdown Spectroscopy*, in *Laser-Induced Breakdown Spectroscopy,* J.P. Singh and S.N. Thakur, Editors. 2007, Elsevier: Amsterdam.

17. Haisch, C., et al., *Characterization of colloidal particles by laser-induced plasma spectroscopy (LIPS).* Analytica Chimica Acta, 1997. **346**(1): p. 23-35.

18. Park, K., G. Cho, and J.-h. Kwak, *Development of an Aerosol Focusing-Laser Induced Breakdown Spectroscopy (Aerosol Focusing-LIBS) for Determination of Fine and Ultrafine Metal Aerosols.* Aerosol Science and Technology, 2009. **43**(5): p. 375-386.

19. Godwal, Y., et al., *Development of laser-induced breakdown spectroscopy for microanalysis applications.* Laser and Particle Beams, 2008. **26**(1): p. 95-104.

20. Matroodi, F. and S.H. Tavassoli, *Experimental investigation on concurrent laser-induced breakdown spectroscopy Raman spectroscopy.* Applied Optics, 2015. **54**(3): p. 400-407.

21. Golovlyov, V.V. and V.S. Letokhov, *Laser ablation of absorbing liquids.* Applied Physics B, 1993. **57**(6): p. 417-423.

22. Esenaliev, R.O.K., A.A.; Podymova, N.B.; Letokhov, V.S., *Laser ablation of aqueous solutions with spatially homogeneous and heterogeneous absorption.* Applied Physics B, 1994. **59**: p. 9.

23. Knopp, R.S., F.J.; Kim, J.I., *Laser induced breakdown spectroscopy (LIBS) as an analytical tool for the detection of metal ions in aqueous solutions.* Fresenius J Anal Chem, 1996. **355**: p. 5.

24. Carranza, J.E., et al., *On-line analysis of ambient air aerosols using laser-induced breakdown spectroscopy.* Spectrochimica Acta Part B: Atomic Spectroscopy, 2001. **56**(6): p. 851-864.

25. Mukherjee, D., A. Rai, and M.R. Zachariah, *Quantitative laser-induced breakdown spectroscopy for aerosols via internal calibration: Application to the oxidative coating of aluminum nanoparticles*. Vol. 37. 2006. 677-695.

26. Cremers, D.A., L.J. Radziemski, and T.R. Loree, *Spectrochemical Analysis of Liquids Using the Laser Spark.* Applied Spectroscopy, 1984. **38**(5): p. 721-729.

27. Margetic, V., et al., *A comparison of nanosecond and femtosecond laser-induced plasma spectroscopy of brass samples.* Spectrochimica Acta Part B: Atomic Spectroscopy, 2000. **55**(11): p. 1771-1785.

28. Emmert, L.A., et al., *Comparative study of femtosecond and nanosecond laser-induced breakdown spectroscopy of depleted uranium.* Applied Optics, 2011. **50**(3): p. 313-317.

29. Baudelet, M., et al., *Femtosecond time-resolved laser-induced breakdown spectroscopy for detection and identification of bacteria: A comparison to the nanosecond regime.* 2006. **99**(8): p. 084701.

30. Baudelet, M., et al., *Spectral signature of native CN bonds for bacterium detection and identification using femtosecond laser-induced breakdown spectroscopy*. Vol. 88. 2006. 063901-063901.

31. Eland, K.L., et al., *Energy Dependence of Emission Intensity and Temperature in a LIBS Plasma Using Femtosecond Excitation.* 2001. **55**(3): p. 286-291.

32. Wu, P., W.L. Lempert, and R.B. Miles, *Megahertz Pulse-Burst Laser and Visualization of Shock-Wave/Boundary-Layer Interaction.* AIAA Journal, 2000. **38**(4): p. 672-679.

33. Thurow, B.S., et al., *3-D flow imaging using a MHz-rate pulse burst LASER system.* 15th Int Symp on Applications of Laser Techniques to Fluid Mechanics, 2010.

34. Fuest, F., et al., *Development of a High-Energy Pulse Burst Laser System for High-Speed Fluid Dynamics and Combustion Measurements*, in *51st AIAA Aerospace Sciences Meeting including the New Horizons Forum and Aerospace Exposition*. 2013, American Institute of Aeronautics and Astronautics.

35. Pořízka, P., et al., *High repetition rate laser-induced breakdown spectroscopy using acousto-optically gated detection*. Vol. 85. 2014. 073104-073104.

36. Cristoforetti, G., et al., *Quantitative analysis of aluminium alloys by low-energy, high-repetition rate laser-induced breakdown spectroscopy.* Journal of Analytical Atomic Spectrometry, 2006. **21**(7): p. 697-702.

37. Wu, P.P. and R.B. Miles, *High-energy pulse-burst laser system for megahertz-rate flow visualization.* Optics Letters, 2000. **25**(22): p. 1639-1641.

38. Slipchenko, M.N., et al., *All-diode-pumped quasi-continuous burst-mode laser for extended high-speed planar imaging.* Optics Express, 2013. **21**(1): p. 681-689.

39. Roy, S., et al., *100-ps-pulse-duration, 100-J burst-mode laser for kHz-MHz flow diagnostics.* Optics Letters, 2014. **39**(22): p. 6462-6465.

40. Wu, W., et al., *100 kHz, 3.1 ns, 1.89 J cavity-dumped burst-mode Nd:YAG MOPA laser.* Optics Express, 2017. **25**(22): p. 26875-26884.

41. Hammack, S.D., et al., *20 kHz CH2O and OH PLIF with stereo PIV.* Optics Letters, 2018. **43**(5): p. 1115-1118.

42. Drogoff, B.L., et al., *Influence of the laser pulse duration on laser-produced plasma properties.* Plasma Sources Science and Technology, 2004. **13**(2): p. 223-230.

43. Miller, J.D., et al., *Ultrahigh-frame-rate OH fluorescence imaging in turbulent flames using a burst-mode optical parametric oscillator.* Optics Letters, 2009. **34**(9): p. 1309-1311.

44. Jiang, N., et al., *Development of high-repetition rate CH PLIF imaging in turbulent nonpremixed flames.* Proceedings of the Combustion Institute, 2011. **33**(1): p. 767-774.

45. Gabet, K.N., et al., *High-speed CH2O PLIF imaging in turbulent flames using a pulse-burst laser system.* Applied Physics B, 2012. **106**(3): p. 569-575.

46. Halls, B.R., et al., *20-kHz-rate three-dimensional tomographic imaging of the concentration field in a turbulent jet.* Proceedings of the Combustion Institute, 2017. **36**(3): p. 4611-4618.

47. Halls, B.R., et al., *4D spatiotemporal evolution of combustion intermediates in turbulent flames using burst-mode volumetric laser-induced fluorescence.* Optics Letters, 2017. **42**(14): p. 2830-2833.

48. Essien, M., L.J. Radziemski, and J. Sneddon, *Detection of cadmium, lead and zinc in aerosols by laser-induced breakdown spectrometry.* Journal of Analytical Atomic Spectrometry, 1988. **3**(7): p. 985-988.

49. Neuhauser, R.E., U. Panne, and R. Niessner, *Laser-induced plasma spectroscopy (LIPS): a versatile tool for monitoring heavy metal aerosols.* Analytica Chimica Acta, 1999. **392**(1): p. 47-54.

50. Zhang, H., F.-Y. Yueh, and J.P. Singh, *Laser-induced breakdown spectrometry as a multimetal continuous-emission monitor.* Applied Optics, 1999. **38**(9): p. 1459-1466.

51. Cheng, M.-D., *Real-time measurement of trace metals on fine particles by laser-induced plasma techniques1The submitted manuscript has been authorized by a contractor of the US Government under Contract no. DE-AC05-95OR22464. Accordingly, the US Government retains a nonexclusive, royalty-free license to publish or reproduce the published form of this contribution, or all others to do so, for US Government purposes.1.* Fuel Processing Technology, 2000. **65-66**: p. 219-229.

52. Anabitarte, F., A. Cobo, and J.M. Lopez-Higuera, *Laser-Induced Breakdown Spectroscopy: Fundamentals, Applications, and Challenges %J ISRN Spectroscopy.* 2012. **2012**: p. 12.

53. Russo, R.E., et al., *Influence of wavelength on fractionation in laser ablation ICP-MS.* Journal of Analytical Atomic Spectrometry, 2000. **15**(9): p. 1115-1120.

54. Alan Hoffman, M.L., Vyshnavi Suntharalingam, *CMOS Detector Technology.* Scientific Detectors for Astronomy, 2005: p. 377-402.

55. Laserna, J., J.M. Vadillo, and P. Purohit, *Laser-Induced Breakdown Spectroscopy (LIBS): Fast, Effective, and Agile Leading Edge Analytical Technology.* Applied Spectroscopy, 2018. **72**(1_suppl): p. 35-50.

56. Fichet, P., et al., *Quantitative elemental determination in water and oil by laser induced breakdown spectroscopy.* Analytica Chimica Acta, 2001. **429**(2): p. 269-278.

57. Zhang, D.C., et al., *Simple method for liquid analysis by laser-induced breakdown spectroscopy (LIBS).* Optics Express, 2018. **26**(14): p. 18794-18802.

58. Bilge, G., et al., *Performance evaluation of laser induced breakdown spectroscopy in the measurement of liquid and solid samples.* Spectrochimica Acta Part B: Atomic Spectroscopy, 2018. **145**: p. 115-121.

59. Melessanaki, K., et al., *The application of LIBS for the analysis of archaeological ceramic and metal artifacts.* Applied Surface Science, 2002. **197-198**: p. 156-163.

60. Fortes, F.J., et al., *Chronocultural sorting of archaeological bronze objects using laser-induced breakdown spectrometry.* Analytica Chimica Acta, 2005. **554**(1): p. 136-143.

61. Corsi, M., et al., *A fast and accurate method for the determination of precious alloys caratage by Laser Induced Plasma Spectroscopy*. Vol. 13. 2001. 373-377.

62. Jurado-López, A. and M. Castro, *Chemometric Approach to Laser-Induced Breakdown Analysis of Gold Alloys*. Vol. 57. 2003. 349-52.

63. Nguyen, T.H., et al. *Laser induced breakdown spectroscopy (LIBS) study of surface oxidation of bulk aluminum and aluminum particles*. in *Laser Applications to Chemical and Environmental Analysis*. 2004. Annapolis, Maryland: Optical Society of America.

64. Vors, E., L.J.A. Salmon, and B. Chemistry, *Laser-induced breakdown spectroscopy (LIBS) for carbon single shot analysis of micrometer-sized particles.* 2006. **385**(2): p. 281-286.

65. Hahn, D.W., W.L. Flower, and K.R. Hencken, *Discrete Particle Detection and Metal Emissions Monitoring Using Laser-Induced Breakdown Spectroscopy.* Applied Spectroscopy, 1997. **51**(12): p. 1836-1844.

66. Thurow, B. and A. Satija, *Design of a MHz Repetition Rate Pulse Burst Laser System at Auburn University*, in *44th AIAA Aerospace Sciences Meeting and Exhibit*. 2006, American Institute of Aeronautics and Astronautics.

67. Hartog, D.J.D., et al., *Pulse-burst laser systems for fast Thomson scattering (invited).* 2010. **81**(10): p. 10D513.

68. Hartog, D.J.D., et al., *A pulse-burst laser system for Thomson scattering on NSTX-U.* Journal of Instrumentation, 2017. **12**(10): p. C10002-C10002.

69. Young, W.C., et al., *High-repetition-rate pulse-burst laser for Thomson scattering on the MST reversed-field pinch.* Journal of Instrumentation, 2013. **8**(11): p. C11013-C11013.

70. Roy, S., et al., *Development of a three-legged, high-speed, burst-mode laser system for simultaneous measurements of velocity and scalars in reacting flows.* Optics Letters, 2018. **43**(11): p. 2704-2707.

71. Lynch, K. and B. Thurow, *Three Dimensional Flow Visualization Using a Pulse Burst Laser System*. 2009: AIAA.

72. Thurow, B., et al., *Narrow-linewidth megahertz-rate pulse-burst laser for high-speed flow diagnostics.* Applied Optics, 2004. **43**(26): p. 5064-5073.

73. Beresh, S.J., et al., *Pulse-Burst PIV in a High-Speed Wind Tunnel*, in *53rd AIAA Aerospace Sciences Meeting*. 2015, American Institute of Aeronautics and Astronautics.

74. Wang, Z., et al., *Ultra-high-speed PLIF imaging for simultaneous visualization of multiple species in turbulent flames.* Optics Express, 2017. **25**(24): p. 30214-30228.

75. Thurow, B., et al., *Further Development of Temporally Resolved PDV and Its Application to Compressible Free Shear Layers*, in *24th AIAA Aerodynamic Measurement Technology and Ground Testing Conference*. 2004, American Institute of Aeronautics and Astronautics.

76. Meyer, T.R., et al., *High-speed, three-dimensional tomographic laser-induced incandescence imaging of soot volume fraction in turbulent flames.* Optics Express, 2016. **24**(26): p. 29547-29555.

77. Stephens, M., et al., *Comparison of Hand and Mechanically Mixed AP/HTPB Solid Composite Propellants*. 2007: AIAA.

78. Hohreiter, V., J.E. Carranza, and D.W. Hahn, *Temporal analysis of laser-induced plasma properties as related to laser-induced breakdown spectroscopy.* Spectrochimica Acta Part B: Atomic Spectroscopy, 2004. **59**(3): p. 327-333.

79. Gondal, M.A., T. Hussain, and Z.H. Yamani, *Optimization of the LIBS Parameters for Detection of Trace Metals in Petroleum Products.* Energy Sources, Part A: Recovery, Utilization, and Environmental Effects, 2008. **30**(5): p. 441-451.

80. Shrivastava, A. and V. Gupta, *Methods for the determination of limit of detection and limit of quantitation of the analytical methods.* Chronicles of Young Scientists, 2011. **2**(1): p. 21-25.

81. Technology, N.I.o.S.a. *NIST atomic energy Levels data center-NIST atomic spectra database*. 1999.

82. Aras, N., et al., *Ultrasonic nebulization-sample introduction system for quantitative analysis of liquid samples by laser-induced breakdown spectroscopy.* Spectrochimica Acta Part B: Atomic Spectroscopy, 2012. **74-75**: p. 87-94.

APPENDIX A

A. Data Analysis Code

This Mat-lab code was used for the data analysis. Each experimental run was saved in a directory and the images gathered were analyzed. We were able to analyze the signals for various delays over all pulses within a burst and quantify the number of laser-particle interactions.

```
clear
%dbstop if error

%Load Save file from Laptop

srcFile_1=dir('E:\LIB_AirPlasma_Aerosol\103118_AirplasmaFreezer_150nsDelay_Gate
5000ns_Gain67_25mj_CL630\*.tif');


%number of images/pulses for analysis

for i_1 =1:970

%call each image within the file and read

filename_1=strcat('E:\LIB_AirPlasma_Aerosol\103118_AirplasmaFreezer_3690nsDelay
_Gate5000ns_Gain67_25mj_CL630\',srcFile_1(i_1).name);
    images_1=imread(filename_1);



 %ALWAYS CHECK TO SEE IF THE IMAGES ARE FLIPPED/inverted
BEFOREHAND
% calculate sum of pixels of x-axis (1:1024) and y-axis (1:144)
          y_1(i_1,:)=sum((fliplr(images_1(1:144,1:1024))));

             y_01= mean(y_1);

%
%   analyzing the elemental peaks of interests
% %%
         area1=(y_1(:,184:208));
          area_1=mean(area1(:));
```

```
area01=(y_1(:,562:584));
area_01=mean(area01(:));
area001=(y_1(:,635:667));
 area_001=mean(area001(:));
area0001=(y_1(:,761:795));
area_0001=mean(area0001(:));
area00001=(y_1(:,321:351));
area_00001=mean(area00001(:));
pulsescan_1=mean(area1,2);
 pulsescan_01=mean(area01,2);
 pulsescan_001=mean(area001,2);
  pulsescan_0001=mean(area0001,2);
   pulsescan_00001=mean(area00001,2);
%
End

%
% Apply conditional averaging conditions to find appropriate particle hits for a given
element

SPH1=find(pulsescan_1>=(area_001*2.2));

%  Apply conditional averaging conditions to find appropriate particle hits for all
elements

OSPH1=find(abs(pulsescan_1-pulsescan_0001)>=(area_001*2.2));
%
%
 Hits1=mean(y_1([SPH1(:)],:));

% number of particle hits

plot(Hits1)

% plot emission spectra

plot(y_01)
  plot(pulsescan_1)


 %%
```

APPENDIX B

B. Plots of All Propellant 16% Al Particle-Pulse Interaction

Pulse-pulse fluctuations from the experimental run of 10 16% Al propellants over 3 burst each

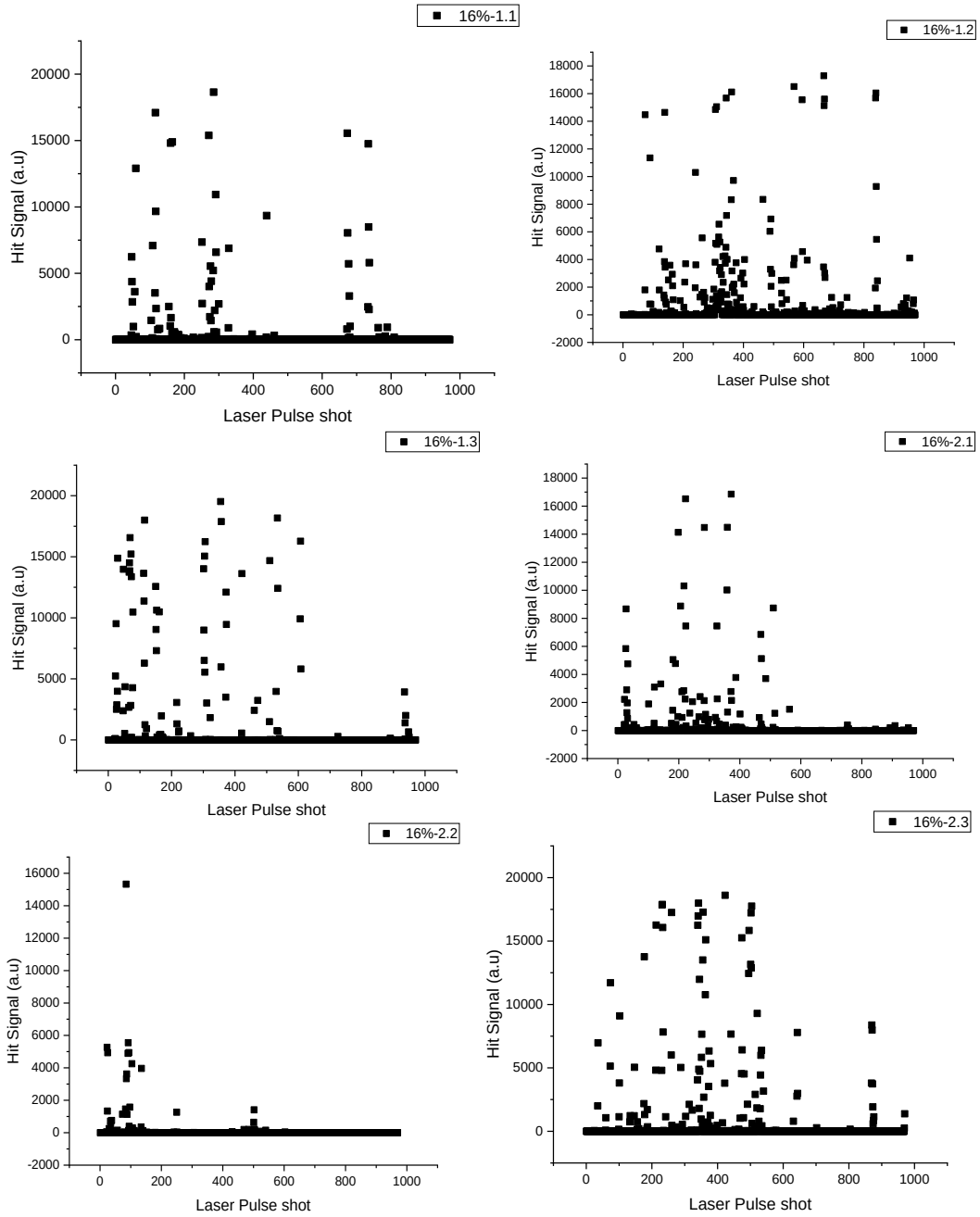

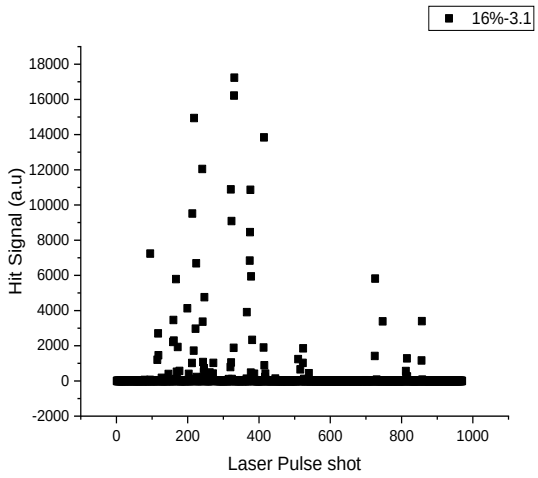
16%-3.1
Hit Signal (a.u)
Laser Pulse shot

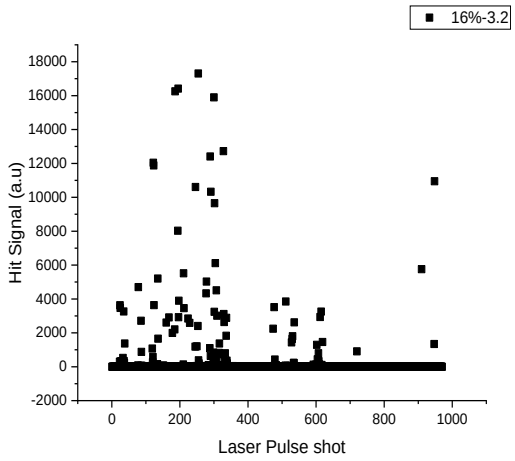
16%-3.2
Hit Signal (a.u)
Laser Pulse shot

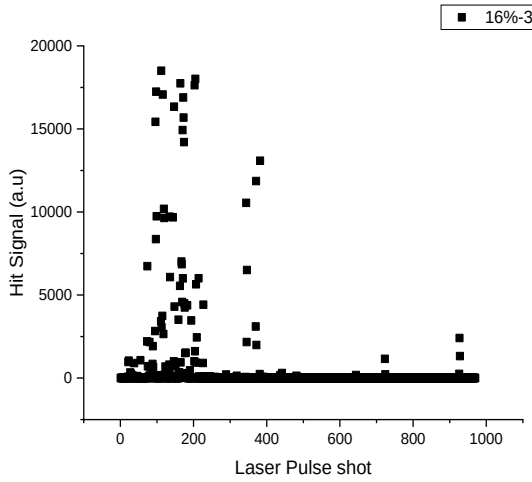
16%-3.3
Hit Signal (a.u)
Laser Pulse shot

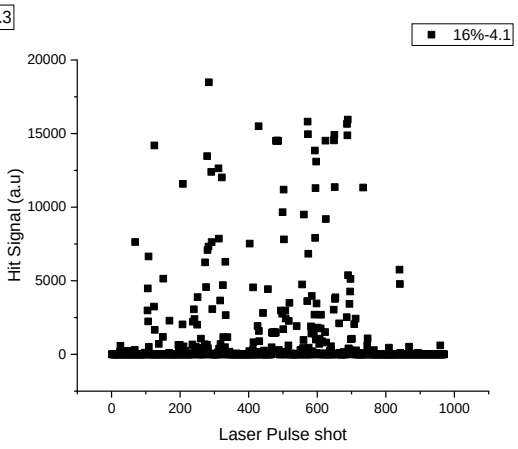
16%-4.1
Hit Signal (a.u)
Laser Pulse shot

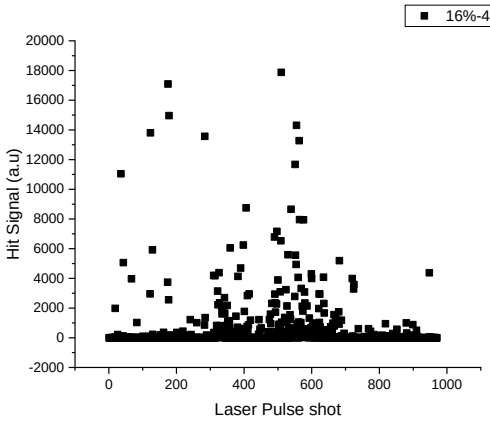
16%-4.2
Hit Signal (a.u)
Laser Pulse shot

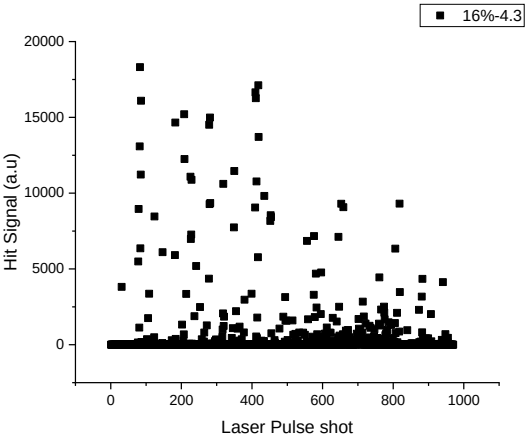
16%-4.3
Hit Signal (a.u)
Laser Pulse shot

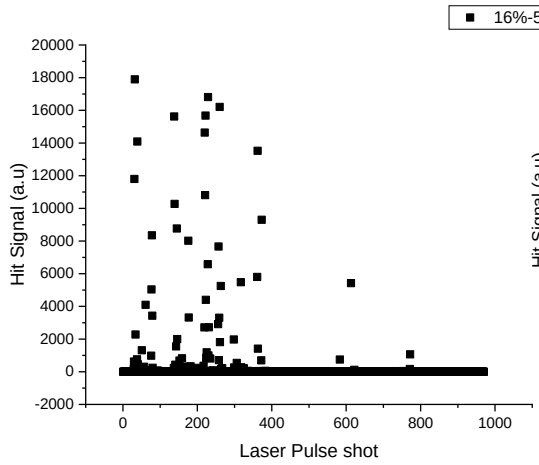
16%-5.1
Hit Signal (a.u)
Laser Pulse shot

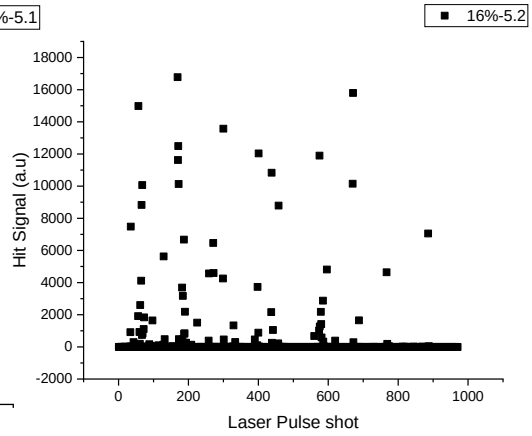
16%-5.2
Hit Signal (a.u)
Laser Pulse shot

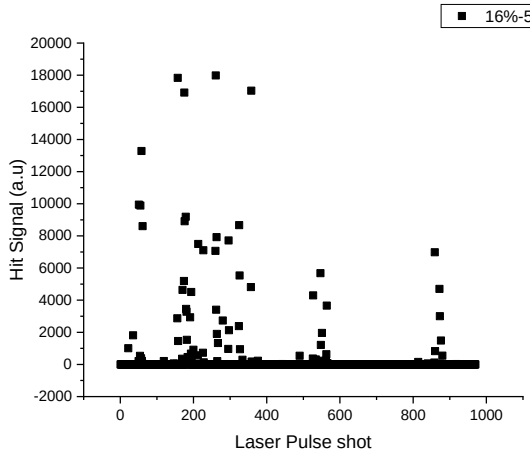
16%-5.3
Hit Signal (a.u)
Laser Pulse shot

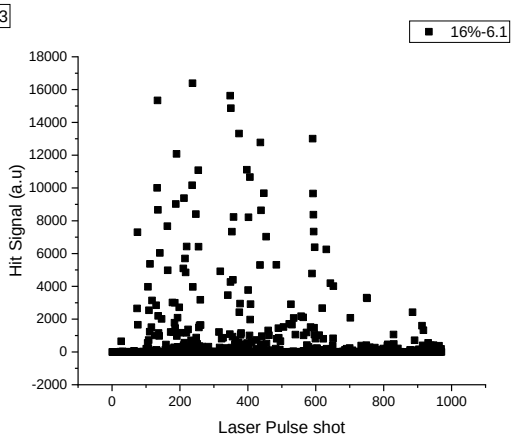
16%-6.1
Hit Signal (a.u)
Laser Pulse shot

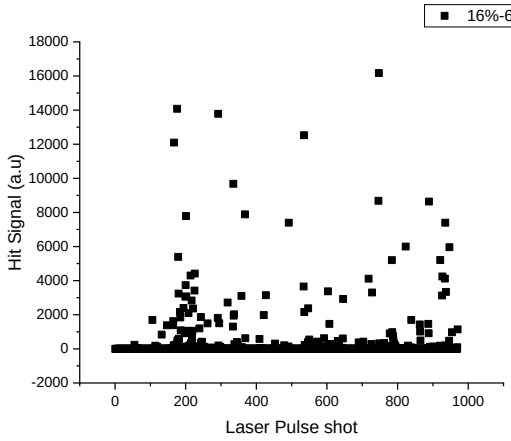
16%-6.2
Hit Signal (a.u)
Laser Pulse shot

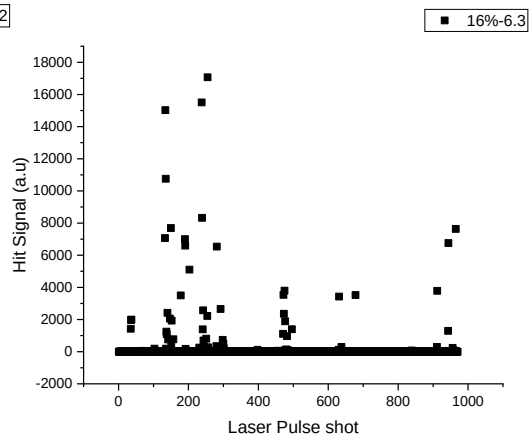
16%-6.3
Hit Signal (a.u)
Laser Pulse shot

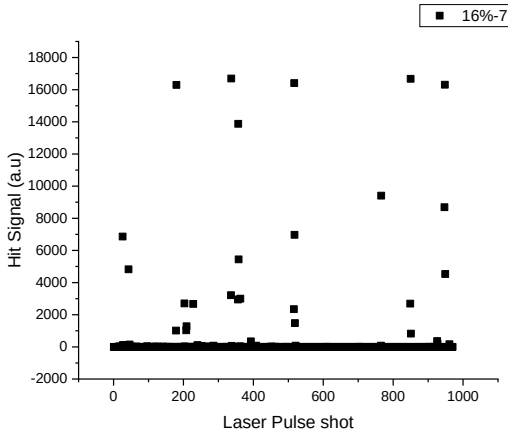
16%-7.1
Hit Signal (a.u)
Laser Pulse shot

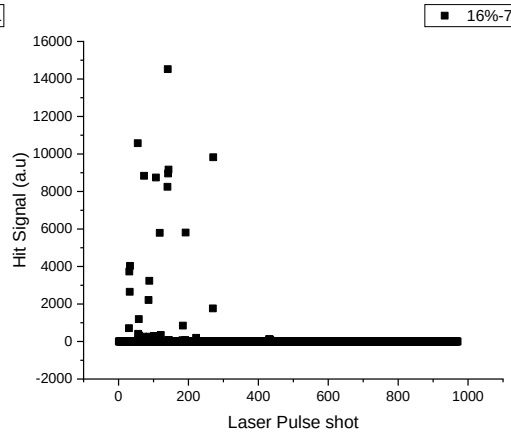
16%-7.2
Hit Signal (a.u)
Laser Pulse shot

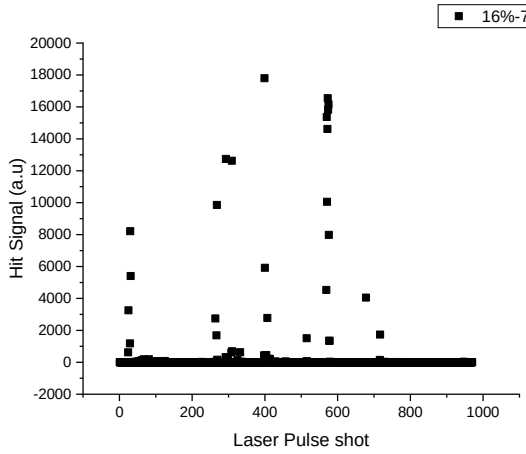
16%-7.3
Hit Signal (a.u)
Laser Pulse shot

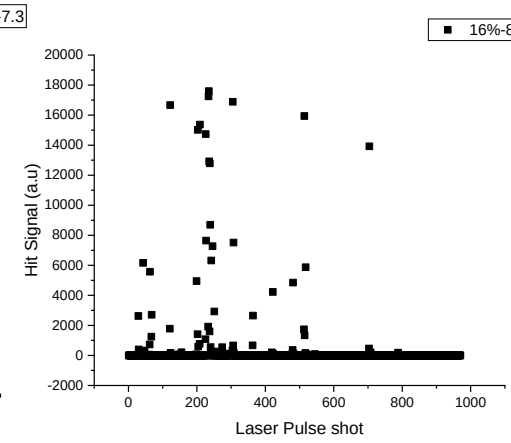
16%-8.1
Hit Signal (a.u)
Laser Pulse shot

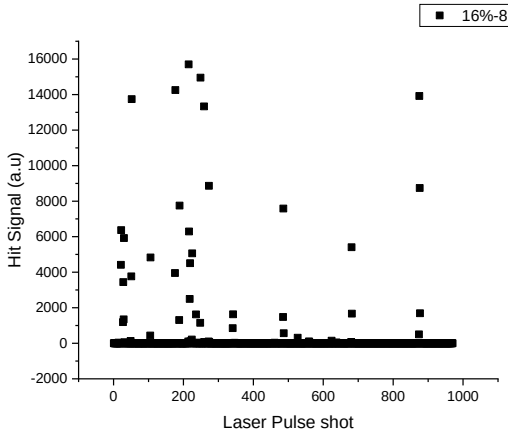
16%-8.2
Hit Signal (a.u)
Laser Pulse shot

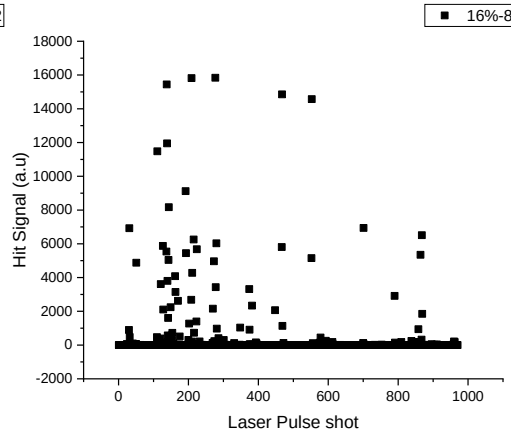
16%-8.3
Hit Signal (a.u)
Laser Pulse shot

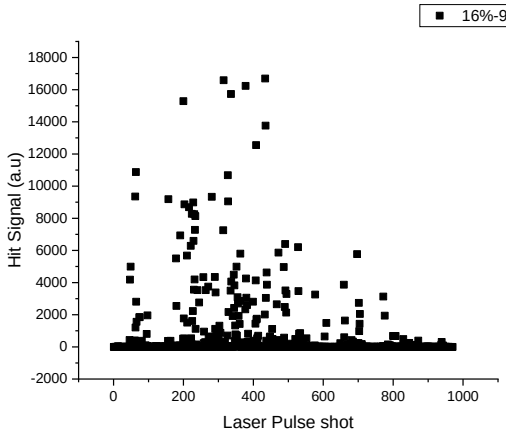
16%-9.1
Hit Signal (a.u)
Laser Pulse shot

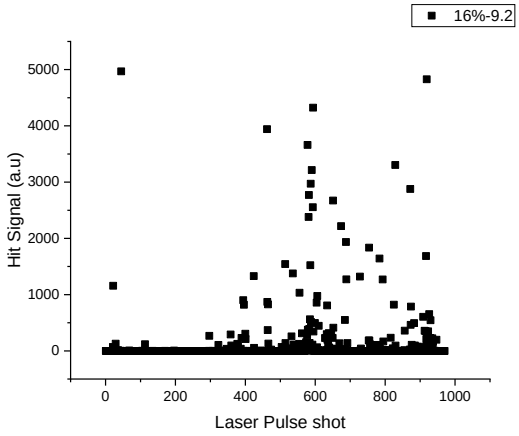
16%-9.2
Hit Signal (a.u)
Laser Pulse shot

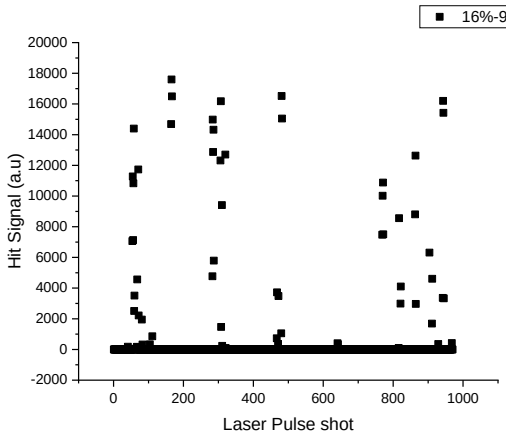
16%-9.3
Hit Signal (a.u)
Laser Pulse shot

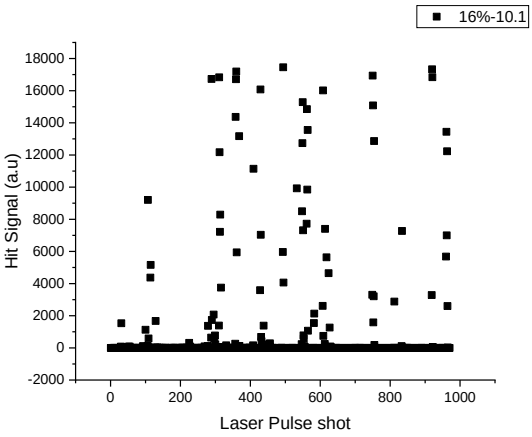
16%-10.1
Hit Signal (a.u)
Laser Pulse shot

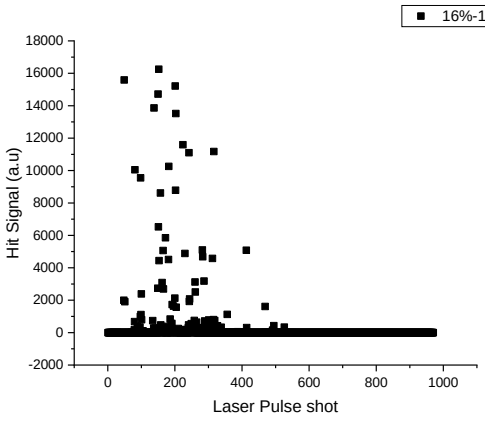
16%-10.2
Hit Signal (a.u)
Laser Pulse shot

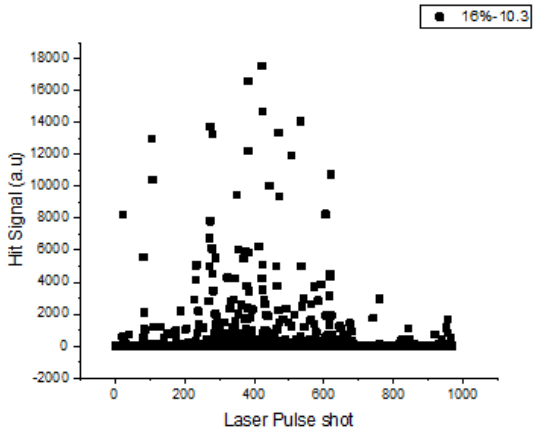
16%-10.3
Hit Signal (a.u)
Laser Pulse shot

APPENDIX C

C. Specifications of Experimental Components

C.1. Lavision High-Speed IRO Intensifier

LAVISION
FOCUS ON IMAGING

HighSpeed IRO

Lens coupled image intensifier module for high-speed camera systems

The **HighSpeed IRO** is an **Intensified Relay Optic** system equipped with an extremely fast gated high precision shutter control. It improves the performance of LaVision's high-speed camera series or other commonly used CMOS cameras.

The **HighSpeed IRO** offers:

- highest UV sensitivity
- sensitivity peak within visible range
- short gating times down to 10 ns
- enhanced lens coupling unit resulting in reduced vignetting (signal decrease to the rim)

The **HighSpeed IRO** is a modular lens-coupled system to be mounted in front of high-speed cameras. It has an optimized image intensifier system with fast P46 phosphors for high frame-rate recording without ghosting into subsequent frames.
LaVision **HighSpeed IRO** is available as single-stage (MCP) system or 2-stage (MCP and booster) system. The 2-stage intensifier system configuration yields approx. 10 times higher signal output compared to single-stage system.
For highest frame rates a 2-stage system is required to get adequate dynamic behavior, for moderate frame rates up to approx. 20 kHz a single-stage system can be sufficient. The max. achievable frame-rate when using a single-stage system is also dependent on the parameters of the high-speed camera in use.
The IRO controller ensures optimized synchronization to the camera offering various timing modes and automatic enabling/disabling synchronous to the camera recording. Controlling is done via local keypad or remote by the IRO App or by LaVision DaVis program via USB interface. The controller offers the timing modes: Internal, Direct and Burst Seq.
The **HighSpeed IRO** lens system is a 1:1 coupling optics optimized for highest collection efficiency, resolution and minimized shading (center to rim) for object diameter of 25 mm. The 1:1 coupling matches optimal typical large CMOS high-speed camera sensors, as this way the whole sensor is illuminated by the image of the 25 mm intensifier.
An appropriate mounting kit consisting of 500 mm optical rail with 3 clamps, posts and holders is included in the system. The rail holds the **HighSpeed IRO** and the CMOS camera. An optional add on "**HighSpeed IRO** Focusing Base Mount" allows easy focusing of the **HighSpeed IRO** to the CMOS camera.

LaVisionUK Ltd
2 Minton Place / Victoria Road
Bicester, Oxon / OX26 6QB / United Kingdom
E-Mail: sales@lavision.com / www.lavisionuk.com
Phone: +44-(0)-870-997-6532 / Fax: +44-(0)-870-762-6252

LaVision GmbH
Anna-Vandenhoeck-Ring 19
D-37081 Göttingen / Germany
E-Mail: info@lavision.com / www.lavision.com
Tel. +49-(0)551-9004-0 / Fax +49-(0)551-9004-100

LaVision Inc.
211 W. Michigan Ave. / Suite 100
Ypsilanti, MI 48197 / USA
E-mail: sales@lavisioninc.com / www.lavisioninc.com
Phone: (734) 485 - 0913 / Fax: (240) 465 - 4306

LaVision
FOCUS ON IMAGING

General System Specification

Spectral range	190 – 800 nm (depending on photo cathode)
Max. repetition rate	up to 300 kHz with 10 ns gate for 2-stage systems up to 20 kHz with 10 ns gate for single-stage systems depending on camera model used
Min. exposure time	10 ns in internal mode
Lens coupling	1:1, η~ 12%
Input adapter	Nikon F-mount
Vignetting	< 10% (center to rim)

Image Intensifier

2-stage system	intensifier type: 1st stage: Gen 2 proximity focused MCP 2nd stage: Gen 1 proximity tube (booster)
Single-stage system	intensifier type 1st stage: Gen 2 proximity focused MCP
Diameter	25 mm
Input window	quartz (other on request)
Photo cathode	S20 (S25), minimum gate 10 ns
Phosphor screen	P46, decay time < 3 µs (to 1%)

Electronics

Operation modes

Internal

Gating (exposure)	10 ns – 80 ms (5 ns/3 ns with PS-delay option)
Delay	0 – 80 ms
Delay/gate resolution	5 ns steps (1 ns with PS-delay option)

Direct

Gating (exposure)	follows external TTL signal
Gate min.	5 ns (3 ns optional)

Burst Seq.

Multiple gate pulses as in mode internal released by one external trigger.

Max frequency	300 kHz corresponding to min cycle time = 33 µs for delay/gate entries

Programming

Remote control via	USB interface
Control	a) local via LCD keypad/display b) remote from PC via DaVis or IRO App
Power supply	230 V or 110 V

Non-Uniformity	+/-15% for MCP image intensifiers +/-10% for NON-MCP intensifiers (boosters)

LaVisionUK Ltd
2 Minton Place / Victoria Road
Bicester, Oxon / OX26 6QB / United Kingdom
E-Mail: sales@lavision.com / www.lavisionuk.com
Phone: +44-(0)-870-997-6532 / Fax: +44-(0)-870-762-6252

LaVision GmbH
Anna-Vandenhoeck-Ring 19
D-37081 Göttingen / Germany
E-Mail: info@lavision.com / www.lavision.com
Tel. +49-(0)551-9004-0 / Fax +49-(0)551-9004-100

LaVision Inc.
211 W. Michigan Ave. / Suite 100
Ypsilanti, MI 48197 / USA
E-mail: sales@lavisioninc.com / www.lavisioninc.com
Phone: (734) 485 - 0913 / Fax: (240) 465 - 4306

LAVISION
FOCUS ON IMAGING

Cathode Sensitivity

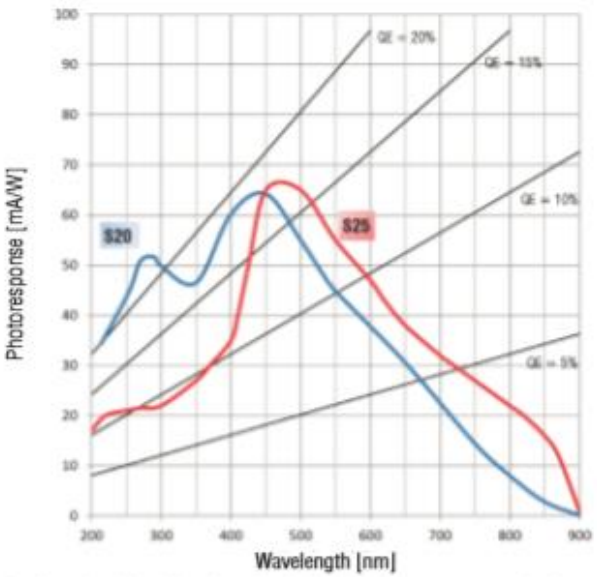

The dynamic behavior is determined by the maximum amount of recharge current and the optimized configuration of components. A selected gain factor cannot be maintained in a stable operation when the recharge current cannot deliver the required number of electrons for that gain. This effect is called 'depletion'. At smaller signal levels (few counts) this will show up at higher repetition rates. A good high-speed intensifier can maintain linearity even at full signal level (1024 counts for a 10 bit camera) up to very high repetition rates. The maximum signal current depends on the pixel size and sensitivity of the selected camera detector.

HighSpeed IRO Dynamics

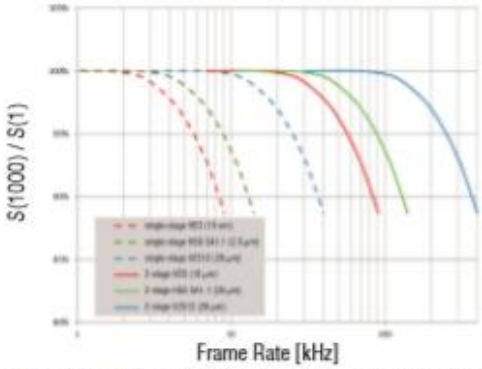

The **HighSpeed IRO** dynamics specifies the linear range limit for recording a constant signal where the signal degradation is less than 10% of the original signal at first frames.
The graph shows the signal degradation of **HighSpeed IRO** as function of frame rate for various high-speed cameras at a constant signal level of 1000 cnts. The solid lines represent the 2-stage **HighSpeed IRO** systems. The dashed lines are given for single-stage **HighSpeed IRO** systems.

LAVISION
FOCUS ON IMAGING

Dimensions

Size (L x W x H)	300 x 135 x 155 mm³
Weight	~ 6 kg

An optional focusing mount with micrometer screw is available for precise alignment of the focal plane of the high-speed camera with respect to the **HighSpeed IRO**.

Ordering information

Part number	Description
1102052	HighSpeed IRO, 25 mm, 10 ns, 300 kHz, S20, 2-stage, with 1:1 coupling
1102054	HighSpeed IRO, 25 mm,10 ns, 300 kHz, S25, 2-stage, with 1:1 coupling
1102057	HighSpeed IRO, 25mm, 10ns, 20 kHz, S20, single-stage,with 1: 1 coupling
1010103	Adapter for FASTCAM SA4 / SA1.1 / SA5 cameras
1010104	Adapter for FASTCAM SA4 / SA1.1 / SA5 cameras w/o internal mech. shutter
1010105	Adapter for FASTCAM SA-X2 / SA-Z cameras
1010633	Adapter for FASTCAM Mini AX
1008857	Adapter for Phantom vx1x / vx4x / vox1x / vox4x cameras
1011486	Adapter for Phantom Miro and VEO cameras
1102056	HighSpeed IRO focusing base mount including micrometer screw for easy focusing

Princeton Instruments

SPECTROSCOPY GROUP

IsoPlane® 160 Spectrometer

The IsoPlane 160 spectrometer brings Princeton Instruments' award-winning IsoPlane SCT-320 performance to a new, smaller platform. The IsoPlane 160 is the first compact spectrometer that provides outstanding imaging, high spectral resolution and excellent light-gathering power from the vacuum UV to the mid-IR without compromises. The IsoPlane 160 is ideally suited for multifiber spectroscopy and can resolve dozens of spatially separate spectral channels without crosstalk. It works seamlessly with Princeton Instruments' industry-leading cameras and detectors, and our LightField with IntelliCal or WinSpec data acquisition software packages. **Spectroscopy reimagined!**

FEATURES	BENEFITS
Aberration-reduced design	Greatly reduced astigmatism and coma at all wavelengths across the entire focal plane. Resolve up to100 optical fiber channels with minimal crosstalk. Excellent spatial and spectral resolution with CCD cameras with heights of up to 14 mm. No other mirror-based scanning spectrograph offers comparable performance.
Outstanding imaging performance and large f/3.88 entrance aperture	Spectral linewidths of 2.0 20 µm pixels or better across the 27 mm wide focal plane. The IsoPlane 160 offers the resolution of a 300 mm instrument with equal or better light-gathering power.
High fluence	The IsoPlane 160 is a high-fluence instrument: photons are diffracted to the peaks of spectral lines rather than to the wings. High resolution is maintained when binning over a single row or the entire sensor height.
Sliding tube camera mount	Easy camera mounting with improved split-clamp hardware. Fine adjustment for razor-sharp focus.
Kinematic torque-limiting turret mount	Improves reproducibility when changing grating turrets. Up to three triple-grating turrets supported.
High efficiency optical coatings	Acton #1900 mirror coating gives highest reflectivity from UV to NIR. Optional silver, gold, or dielectric coatings are available with reflectivities of 98% or better. See page 4 for details.
Compatible with wide variety of cameras	Princeton Instruments PIXIS, PyLoN, Spec-10/LN, PyLoN-IR, ProEM 1600, PI-MAX3/4 and NIRvana cameras with spectroscopy or C mount.
Wide range of accessories	Including fiber bundles, adapters, shutters, filter wheels, purge ports, and light sources such as the IntelliCal® spectrograph wavelength and intensity calibration system. Accessories sold separately.
Optional: LightField® (for Windows® 7/8, 64-bit) or WinSpec (forWindows XP®/7/8, 32-bit)	Flexible software packages for data acquisition, display, and analysis. LightField offers intuitive, cutting-edge user interface, IntelliCal, hardware time stamping, and more. Software sold separately.

Powered by LightField®

NOTE: IsoPlane 160 is shown pictured with a Princeton Instruments PIXIS:400BR_eXcelon camera - sold separately.

Applications:
Multi-channel spectroscopy,
Microspectroscopy, Raman scattering,
Fluorescence, Photoluminescence, LIBS,
Fourier-domain spectroscopy, Biomedical imaging

Princeton Instruments

SPECTROSCOPY GROUP

Specifications

	IsoPlane 160
Focal length	203 mm
Aperture ratio	f/3.88
Usable wavelength range	190 nm to mid-IR with available mirror coatings, gratings, and detectors (to ~150 nm with optional purge capability)
CCD resolution (20 µm pixels)*	0.16 nm or better across a 27 mm wide focal plane
PMT resolution (10 µm slit)*	0.13 nm
Stray light	< 4 x 10^{-5}
Grating mount /size	Interchangeable triple grating turret with on-axis grating rotation: 40 x 40 mm gratings
Focal plane size	27 mm wide x 14 mm high
Astigmatism	<100 µm at all wavelengths across the entire focal plane
Spatial resolution (MTF)	≥12 line pairs/mm @ 50% modulation, measured at focal plane center ≥ 6 line pairs/mm @ 50% modulation, measured over 27 x 8 mm focal plane
Slits	**Entrance and Exit slits:** - Standard manual (10 µm – 3 mm) - Optional motorized (10 µm – 3 mm and 10 µm – 12 mm versions) Kinematic entrance slit available for imaging and microspectroscopy.
Wavelength accuracy*	Mechanical: ± 0.2 nm | With IntelliCal (using fixed wavelength calibration): ± 0.02 nm
Wavelength repeatability*	Mechanical: ± 0.025 nm | With IntelliCal (using fixed wavelength calibration): ± 0.0025 nm
Drive step size*	0.005 nm
Size Weight	8.5" x 9.25" x 8" height 15 lbs.
Optical axis height	Adjustable: 5.0" to 5.875"
Computer interface	USB and RS232

* With 1200 groove/mm grating @ 435 nm

Use the Grating Dispersion Calculator on our website:
www.princetoninstruments.com/spectroscopy/calculator/ for information on IsoPlane 160 performance with various gratings and Princeton Instruments cameras.

Specifications subject to change without notice.

www.princetoninstruments.com | info@princetoninstruments.com
TOLL-FREE +1.877.474.2286 | PHONE +1 609.587.9797
Visit the Princeton Instruments website to find a dealer in your area.

C.2. Princeton Instruments Iso-Plane 160 Spectrometer

Princeton Instruments
SPECTROSCOPY GROUP

IsoPlane 160:
Oustanding Imaging
& Spectral Resolution

IsoPlane 160 - high resolution across the entire focal plane

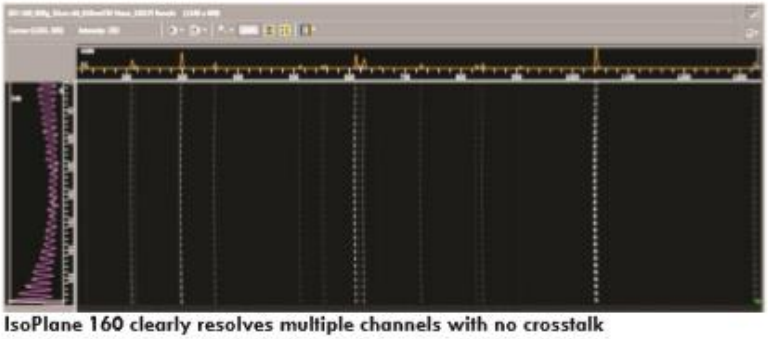

IsoPlane 160 clearly resolves multiple channels with no crosstalk

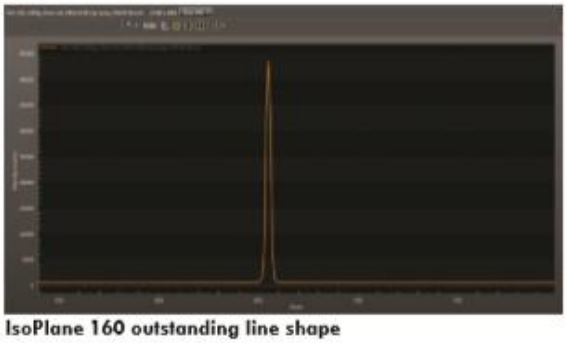

IsoPlane 160 outstanding line shape
546 nm Hg line with 1200 g/mm grating

www.princetoninstruments.com | info@princetoninstruments.com
TOLL-FREE +1.877.474.2286 | PHONE +1 609.587.9797
Visit the Princeton Instruments website to find a dealer in your area.

Princeton Instruments

SPECTROSCOPY GROUP

Mirror Coatings: Reflectance Curves

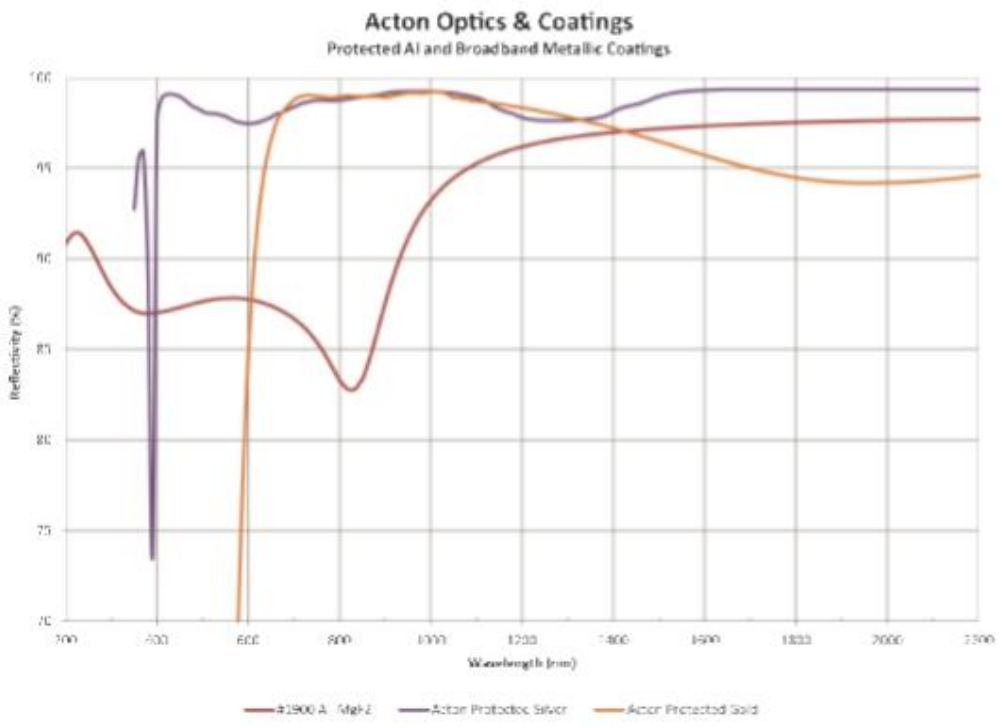

NOTE: #1900 coating is standard on IsoPlane mirrors. Gold and silver coatings are offered as an option at an additional fee.

C.3. Photron Ultra-High-Speed FASTCAM SA-Z

Photron

Datasheet

High performance high-speed camera system

The Photron FASTCAM SA-Z offers scientists, researchers and engineers the ability to capture high resolution digital images at ultra-high speeds to see and understand previously invisible processes and events. Using Photron's proprietary CMOS image sensor technology, the FASTCAM SA-Z combines high recording rates with outstanding light sensitivity and excellent image quality to provide the most versatile ultra-high speed digital camera available today.

The ultra-high speed FASTCAM SA-Z provides megapixel image resolution at frame rates up to 21,000 frames per second (fps) from its highly light sensitive image sensor (monochrome ISO 50,000) with 12-bit dynamic range delivering the ultimate imaging performance. The FASTCAM SA-Z provides frame rates greater than 2 million fps at reduced image resolution and shutter speeds as short as 159 nanoseconds (export restrictions may apply).

An innovative camera body design exploiting heat-pipe technology provides a thermally stable and reliable high-speed imaging system suitable for use in the most challenging environments. Available in 12-bit monochrome or 36-bit color versions with recording memory options from 8GB to 128GB, the FASTCAM SA-Z offers versatility of use in a wide range of scientific and industrial applications.

Standard operational features of the FASTCAM SA-Z include a mechanical shutter to allow remote system calibration, dual-channel Gigabit Ethernet Interface for fast image download, and internal memory card drives allowing image download and storage to low cost removable recording media. The system also features memory segmentation to allow recording in one memory partition while at the same time downloading a previous recording, and the ability to remotely switch off cooling fans to eliminate vibration when recording at high magnifications.

FASTCAM SA-Z is optionally available with the FASTDrive removable SSD drive permitting high-speed transfer of image data from camera recording memory to removable mass storage media enabling repeated recordings to be made in quick succession without the delays associated with download of data to a PC.

FASTCAM SA-Z

1-Megapixel CMOS Image Sensor:
1024 x 1024 pixels at 20,000fps
896 x 896 pixels at 25,000fps
768 x 512 pixels at 50,400fps
512 x 384 pixels at 87,500fps
512 x 256 pixels at 120,000fps

Maximum Frame Rate:
224,000fps (FASTCAM SA-Z type 200K)
480,000fps (FASTCAM SA-Z type 480K)
2,100,000fps (FASTCAM SA-Z type 2100K)

Class Leading Light Sensitivity:
ISO 12232 Ssat
- ISO 50,000 monochrome
- ISO 20,000 color

Global Electronic Shutter:
1ms to 159ns independent of frame rate (sub-microsecond shutter available on type 2100K only, subject to export control)

Dynamic Range (ADC):
12-bit monochrome, 36-bit color

Internal Recording Memory:
8GB, 16GB, 32GB, 64GB, or 128GB

Optional FASTDrive High Capacity Non-Volatile Data Storage:
1TB or 2TB high-speed solid state drive

Fast Gigabit Ethernet Interface:
Dual Gigabit Ethernet Interface provides high-speed image download to standard notebook/PC

Flexible Frame Synchronization:
Frame rate may be synchronized to external unstable frequencies

Fan Stop Function:
Remotely switch off cooling fans to eliminate vibration when recording at high magnifications

Image Sensor Technical Data

Light Sensitivity:
Expressions of light sensitivity in high-speed cameras can be confusing as a variety of differing measurement techniques are used. Photron publishes light sensitivity figures for its products using the ISO 12232 Ssat Standard.

FASTCAM SA-Z	ISO 12232 Ssat
Monochrome models	ISO 50,000
Color models	ISO 20,000

ISO 12232 Ssat values published by Photron for both monochrome and color cameras are measured excluding infrared sensitivity as defined by the ISO standard measurement procedure ISO 14524.

Monochrome sensors used in the FASTCAM SA-Z are supplied without an IR absorbing filter, extending the camera spectral response beyond 900nm. When the sensitivity of the FASTCAM SA-Z is measured to tungsten light including near IR response an equivalent value of ISO 125,000 is obtained.

Image Sensor:
The FASTCAM SA-Z uses an advanced CMOS image sensor optimized for light sensitivity and high image quality that is unique to Photron.

A 20-micron pixel pitch gives a sensor size at full image resolution of 20.48 x 20.48mm (diagonal 28.96mm).

Lenses designed for both FX (35mm full frame) and also DX (APS-C digital SLR) formats are fully compatible with the FASTCAM SA-Z at full image resolution.

Sensor Type	Proprietary Design Advanced CMOS
Maximum Resolution (pixels)	1024 x 1024 pixels
Sensor Size / Diagonal	20.48 x 20.48mm / 28.96mm
Pixel Size (microns)	20µm x 20µm
Quantum Efficiency	46% at 630nm
Fill Factor	58%
Color Matrix	Bayer CFA (single sensor)
ISO 12232 Ssat sensitivity	ISO 50,000 monochrome ISO 20,000 color (monochrome sensor equivalent ISO 125,000 including near IR response)
Shutter	Global Electronic Shutter 1ms to 1µs independent of frame rate (2100K only: 159ns shutter available subject to export control)

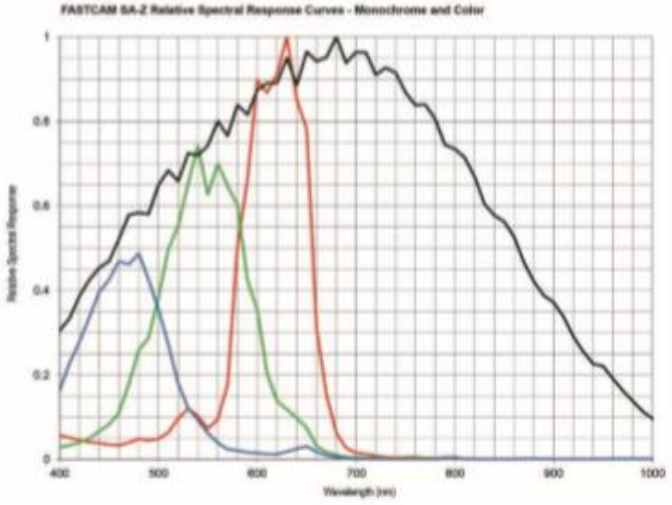

Camera Performance Specifications

Camera Performance Specifications

Model	SA-Z
Full Frame Performance	20,000fps 1024 x 1024 pixels
Maximum Frame Rate	Type 200K: 224,000fps Type 480K: 480,000fps* Type 2100K: 2,100,000fps*
Minimum Exposure	Global electronic shutter to 1µs selectable independent of frame rate (159ns option available with SA-Z type 2100K only) *
Ruggedized Mechanical Calibration Shutter	Standard Feature
Dynamic Range (ADC)	12-bit monochrome 36-bit color
Memory Capacity Options	8GB: 5,453 frames at full resolution 16GB: 10,914 frames at full resolution 32GB: 21,837 frames at full resolution 64GB: 43,682 frames at full resolution 128GB: 87,373 frames at full resolution
Memory Partitions	Up to 128 memory segments
Region of Interest	Selectable in steps of 128 pixels (horizontal) x 8 pixels (vertical)
Trigger Inputs	Selectable +/- TTL 5V and switch closure
Trigger Delay	Programmable on selected input / output triggers: 100ns resolution
Input / Output	Input: Trigger (TTL/Switch), sync, ready, event, IRIG Output: trigger, sync, ready, rec, exposure
Trigger Modes	Start, end, center, manual, random, random reset, random center, random manual, random loop, record on command
Time Code Input	IRIG-B
External Sync	+/- TTL 5Vp-p Variable frequency sync
Camera Control Interface	High-speed Gigabit Ethernet - (Single or Dual connections)
Image Data Display	Frame rate, shutter speed, trigger mode, date/time, status, real time / IRIG time, frame count, resolution
Saved Image Formats	JPEG, AVI, TIFF, BMP, RAW, RAWW, MRAW, PNG, MOV, and FTIF - Images can be saved with or without image data and in 8-bit,16-bit or 36-bit depth of sensor where supported
Supported OS	Microsoft Windows operating system including: 7, 8, 8.1, 10 (32/64-bit)

*** Frame rates above 226,000fps and exposure times below 1µs may be subject to export control regulations in some areas**

Removable Data Storage Options:

To enable the rapid transfer of camera memory data to high capacity, removable non-volatile storage media the FASTCAM SA-Z offers two options:

Supplied as standard with the system are two UHS-I (SDR104) compatible SD memory card drives. Readily available high capacity SD cards compatible with these drives offer a low cost and convenient non-volatile removable storage option.

Optionally, the FASTCAM SA-Z can be supplied with the Photron FASTDrive high capacity removable SSD media system in place of SD card drives. The ultra-high data rate FASTDrive system allows a 64GB camera memory recording to be transferred to a removable SSD media drive in approximately 1 minute. Recorded data can then be directly accessed while coupled to the camera or the drive may be removed and inserted into the portable FASTDock station connected to any Windows PC.

Camera Operation Features

Frame Synchronization	Accurate frame synchronization with other cameras and with external and unstable frequencies.
Dual Slope Shutter (Extended Dynamic Range)	Selectable in 20 steps (0 to 95% in 5% increments) to prevent pixel over exposure without post processing.
Memory Partitions	Up to 128 memory segments allow multiple events to be stored in camera memory before downloading, with automatic progression to the next available partition.
Low Light Mode	Operation at minimum frame rate with separately adjustable shutter time to allow easy camera set-up and focus in ambient lighting.
Video Output	Live and playback via dual HD-SDI or RS-170 (NTSC/PAL) (zoom, pan, scroll control via optional LCD keypad).
IRIG Phase Lock	Enables multiple cameras to be synchronized together with other instrumentation equipment to a master external time source.
Internal Delay Generator	Allows programmable delays to be set on input and output triggers, 100ns resolution.
Event Markers	Up to ten user entered event markers to define specific events within the recorded image sequence .
Download While Recording	FASTCAM SA-Z supports Partition Recording Mode, allowing image data captured in one memory partition to be downloaded while at the same time recording into another partition.
Automatic Download	The system can be set to automatically download image data to the control PC and, when download is complete to re-arm in readiness for the next trigger with automatically incremented file names.
Software Binning	Virtual pixel binning (2x2, 4x4 etc.) allows increased light sensitivity with reduced image resolution without changing camera field of view.
SD Media Storage	Two UHS-I (SDR104) compatible SD memory card drives allow data transfer to low cost and convenient non-volatile removable media.
FASTDrive	Optional 1TB / 2TB solid state drive (SSD) memory pack provides ultra high data rate transfer to removable media.

Software Operation Features

Image Calibration	2D image calibration allows the measurement of distance and angle from the image. A calibration grid overlay can be superimposed on the image.
Image Overlay	A stored reference image may be overlaid on the live image to allow accurate camera positioning to achieve the same view as a previous test.
Import of Multiple Image Sequences	Multiple image sequences can be loaded and simultaneously replayed. Timing of image sequences can be adjusted to create a common time reference. Time based synchronization allows images captured at different frame rates to be synchronized.
High Dynamic Range Mode	Making use of the full sensor dynamic range, HDR mode allows enhanced detail in both light and dark areas of an image to be displayed simultaneously.
Motion Detector	In order to highlight subtle changes in an image, Motion Detector allows a reference image to be subtracted from a recorded sequence. Details including propagation of shock waves and surface changes during impact can be visualized using the feature.
Line Profile	A line profile representing grey levels along a line drawn across any region of the image is displayed. In live mode the Line Profile can be used to ensure optimum image focus is achieved.
Histogram	A histogram displaying grey levels within a user-defined image area is displayed. In live mode the Histogram can be used to ensure that optimum exposure levels are set for the scene being recorded.

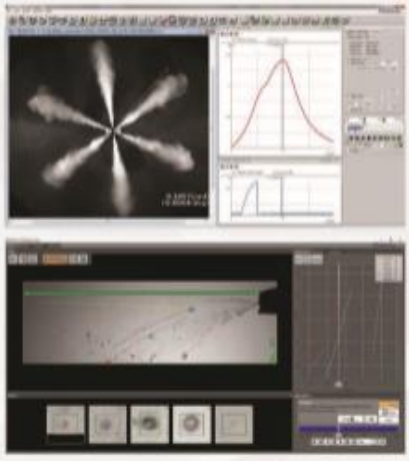

Photron FASTCAM Viewer:
Photron FASTCAM Viewer software (PFV) has been designed to provide an intuitive and feature rich user interface for the control of Photron high-speed cameras, data saving, image replay and simple motion analysis. Advanced operation menus provide access to features for advanced camera operation and image enhancement. Tools are provided to allow image calibration and easy measurement of angles and distances from image data. Also included are a C++ SDK and wrappers for LabView and MATLAB ®.

An optional software plug-in module provides synchronisation between Photron high- speed cameras and data acquired through National Instruments data acquisition systems. Synchronised data captured by the DAQ system provides waveform information which can be viewed alongside high-speed camera images.

Photron FASTCAM Analysis:
PFV software allows image sequences to be exported directly to optional Photron FASTCAM Analysis (PFA) Motion Analysis software. This entry level Motion Analysis software with an on screen 'step by step guide' function launches automatically from Photron FASTCAM Viewer software, and provides automated tracking of up to 5 points using feature or correlation tracking algorithms for the automated analysis of motion within an image sequence.

Operation Features Continued

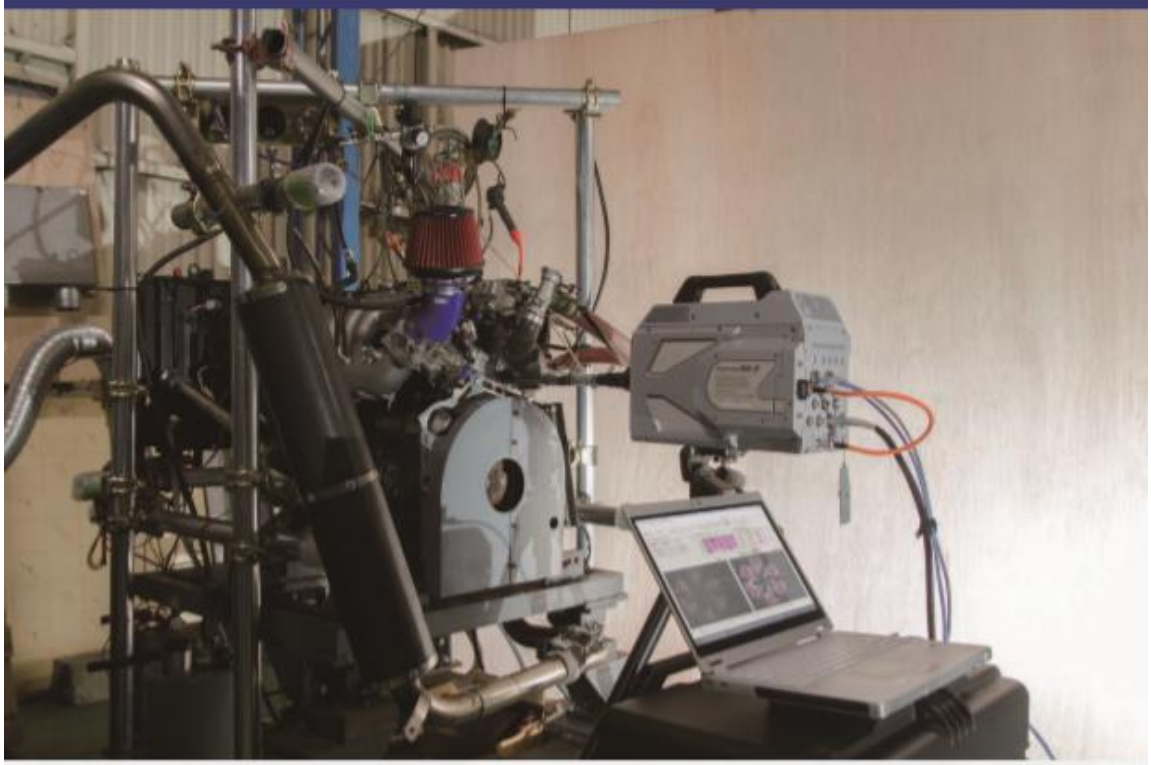

Variable Region of Interest:
Region of Interest (ROI) or sub-windowing allows
a user-specified portion of the sensor to be defined to capture images. By using a reduced portion of the image area, the frame rate at which images are recorded can be increased. FASTCAM SA-Z allows the ROI to be set in increments of 128 pixels horizontal and 8 pixels vertical.

Square Image Sensor Format:
Unlike broadcast and media applications where image formats such as 16:9 have now become standard, in scientific and industrial imaging applications an image sensor with a 1:1 image format is generally accepted to be advantageous. To capture the maximum useful image data in applications including microscopy, detonics, combustion imaging and many others, a 1:1 sensor format provides greater flexibility than 'letterbox' image formats. The FASTCAM SA-Z image sensor allows the user to choose either square or rectangular image formats in order to obtain the maximum subject information.

External Frame Synchronization:
The FASTCAM SA-Z can be fully synchronized with an external event to allow the timing of when each individual image is captured to be precisely referenced. The camera can be accurately synchronized to unstable frequencies allowing complex events such as combustion in rapidly accelerating or decelerating engines to be recorded and studied.

Record During Download Operation:
FASTCAM SA-Z recording memory can be divided into multiple active sections. The user can record an on-going event in one memory partition while at the same time downloading a previously recorded image sequence in order to improve workflow and optimize camera operation.

SA-Z 2100K											
Resolution	Frame Rate	8GB		16GB		32GB		64GB		128GB	
(h x v pixels)	Max fps	Frames	Time (sec)**	Frames	Time (sec)**	Frames	Time (sec)**	Frames	Time (sec)**	Frames	Time (sec)**
1024 x 1024	20,000	5,453	0.27	10,914	0.55	21,837	1.09	43,682	2.18	87,373	4.37
1024 x 1000	21,000	5,584	0.27	11,176	0.53	22,361	1.06	44,731	2.13	89,470	4.26
1024 x 640	25,000	8,648	0.27	13,305	0.53	26,621	1.06	53,251	2.13	106,512	4.26
1024 x 512	40,000	10,908	0.27	21,831	0.55	43,676	1.09	87,367	2.18	174,748	4.37
640 x 488	60,000	18,313	0.31	36,649	0.61	73,320	1.22	146,663	2.44	293,349	4.89
512 x 456	75,000	24,499	0.33	49,027	0.65	98,083	1.31	196,195	2.62	392,420	5.23
640 x 280	100,000	31,919	0.32	63,876	0.64	127,789	1.28	255,615	2.56	511,268	5.11
512 x 256	120,000	43,640	0.36	87,331	0.73	174,712	1.46	349,475	2.91	699,000	5.83
384 x 176	200,000	84,638	0.42	169,371	0.85	338,838	1.69	677,772	3.39	1,355,639	6.78
512 x 56	450,000	199,507	0.42	399,236	0.83	798,593	1.66	1,597,606	3.33	3,195,435	6.66
384 x 64	525,000	232,755	0.44	465,775	0.89	931,809	1.77	1,863,877	3.55	3,728,012	7.10
256 x 56	700,000	299,016	0.57	598,474	1.14	1,597,389	2.28	3,195,219	4.56	6,390,579	9.13
128 x 56	900,000	795,035	0.89	1,596,950	1.77	3,194,750	3.55	6,390,440	7.10	12,781,761	14.20
256 x 24	1,000,000	931,041	0.92	1,863,109	1.85	3,727,244	3.73	7,455,514	7.40	14,912,054	14.79
128 x 32	1,200,000	1,396,563	1.16	2,794,664	2.33	5,590,867	4.66	11,183,272	9.32	22,368,083	18.64
128 x 8	2,100,000	5,586,259	2.66	11,175,654	5.32	22,363,475	10.65	44,733,096	21.30	89,472,339	42.61

* Specifications subject to change without notice.
** Recording time is an estimate and may be different depending on recording conditions and settings.

SA-Z 480K											
Resolution	Frame Rate	8GB		16GB		32GB		64GB		128GB	
(h x v pixels)	Max fps	Frames	Time (sec)**	Frames	Time (sec)**	Frames	Time (sec)**	Frames	Time (sec)**	Frames	Time (sec)**
1024 x 1024	20,000	5,453	0.27	10,914	0.55	21,837	1.09	43,682	2.18	87,373	4.37
1024 x 1000	21,000	5,584	0.27	11,176	0.53	22,361	1.06	44,731	2.13	89,470	4.26
1024 x 640	25,000	8,648	0.27	13,305	0.53	26,621	1.06	53,251	2.13	106,512	4.26
1024 x 512	40,000	10,908	0.27	21,831	0.55	43,676	1.09	87,367	2.18	174,748	4.37
640 x 488	60,000	18,313	0.31	36,649	0.61	73,320	1.22	146,663	2.44	293,349	4.89
512 x 456	75,000	24,499	0.33	49,027	0.65	98,083	1.31	196,195	2.62	392,420	5.23
640 x 280	100,000	31,919	0.32	63,876	0.64	127,789	1.28	255,615	2.56	511,268	5.11
512 x 256	120,000	43,640	0.36	87,331	0.73	174,712	1.46	349,475	2.91	699,000	5.83
384 x 176	200,000	84,638	0.42	169,371	0.85	338,838	1.69	677,772	3.39	1,355,639	6.78
512 x 56	450,000	199,507	0.42	399,236	0.83	798,593	1.66	1,597,606	3.33	3,195,435	6.66
384 x 64	450,000	232,755	0.48	465,775	0.97	931,809	1.94	1,863,877	3.88	3,728,012	7.77
256 x 56	450,000	299,016	0.83	598,474	1.66	1,597,389	3.33	3,195,219	6.66	6,390,579	12.31
128 x 56	450,000	795,035	1.66	1,596,950	3.33	3,194,750	6.66	6,390,440	13.31	12,781,761	26.63
256 x 24	450,000	931,041	1.94	1,863,109	3.88	3,727,244	7.77	7,455,514	15.53	14,912,054	31.07
128 x 32	450,000	1,396,563	2.91	2,794,664	5.82	5,590,867	11.65	11,183,272	23.30	22,368,083	46.60
128 x 8	450,000	5,586,259	11.64	11,175,654	23.29	22,363,475	46.59	44,733,096	93.19	89,472,339	186.40

* Specifications subject to change without notice.
** Recording time is an estimate and may be different depending on recording conditions and settings.

SA-Z 200K											
Resolution	Frame Rate	8GB		16GB		32GB		64GB		128GB	
(h x v pixels)	Max fps	Frames	Time (sec)**	Frames	Time (sec)**	Frames	Time (sec)**	Frames	Time (sec)**	Frames	Time (sec)**
1024 x 1024	20,000	5,453	0.27	10,914	0.55	21,837	1.09	43,682	2.18	87,373	4.37
1024 x 1000	21,000	5,584	0.27	11,178	0.53	22,361	1.06	44,731	2.13	89,470	4.26
1024 x 640	25,000	8,648	0.27	13,305	0.53	26,621	1.06	53,251	2.13	106,512	4.26
1024 x 512	40,000	10,908	0.27	21,831	0.55	43,676	1.09	87,367	2.18	174,748	4.37
640 x 488	60,000	18,313	0.31	36,649	0.61	73,320	1.22	147,663	2.46	293,349	4.89
512 x 456	75,000	24,499	0.33	49,027	0.65	98,083	1.31	196,195	2.62	392,420	5.23
640 x 280	100,000	31,919	0.32	63,876	0.64	127,789	1.28	255,615	2.56	511,268	5.11
512 x 256	120,000	43,640	0.36	87,331	0.73	174,712	1.46	349,475	2.91	699,000	5.83
384 x 176	224,000	84,638	0.38	169,371	0.76	338,838	1.51	677,772	3.03	1,355,639	6.05

* Specifications subject to change without notice. Additional Charts for SA-Z models 480K and 2100K are available in the full product datasheet.
** Recording time is an estimate and may be different depending on recording conditions and settings.

Mechanical & Environmental Specifications

Mechanical and Environmental Specifications	
Mechanical	
Lens Mount	F-mount (G-type lens compatible) and C-mount provided - Optional lens mounts available include Canon EF remote control mount
Camera Mountings	7 x 1/4 - 20 UNC (base, top and sides), 3 x 3/8 - 16 UNC (base and sides)
External Dimensions	
Camera Body (excluding protrusions)	261.6mm (H) x 150mm (W) x 375.4mm (D) 10.3" (H) x 5.9" (W) x 14.8" (D)
Weight	
Camera Body	10.4kg (22.93lbs)
Environmental	
Operating Temperature	0 to 45C, 32° to 113°F
Storage Temperature	-20 to 60C, -4° to 140°F
Humidity	80% or less (non-condensing)
Operational Shock	Tested to 25G, 11ms, 6-axes, 10 times/axis
Cooling	Internal fan cooling (fan-off mode supported)
Power	
AC Power (with supplied adapter)	100 to 240V, 50 to 60Hz
DC Power	20 to 36V, 230VA

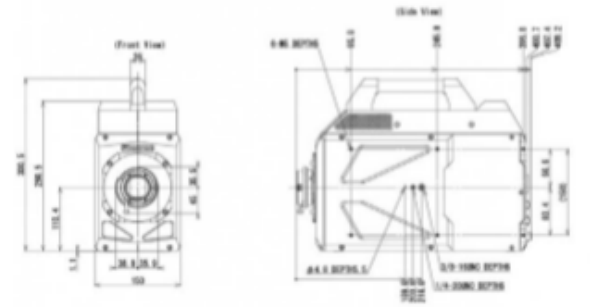

All measurements are in millimeters (mm)

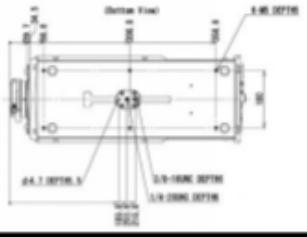

Remote Control LCD Keypad:
An optional hand-held remote control keypad is available to enhance field operation. The keypad provides the operator with local control of all primary camera functions to simplify camera set-up and allow operation without PC connection.

Nikon G-Type Compatible Lens Fitting:
The FASTCAM SA-Z camera is equipped with an objective lens mount compatible with readily available Nikon G-type lenses. Controls provided within the lens mount allow the control of lens aperture on lenses without external iris control.

Canon EF Lens Mount Option:
An optional lens mount supporting Canon EF lenses is available for the FASTCAM SA-Z providing remote control of lens aperture and iris through Photron PFV software.

Rugged Design:
The FASTCAM SA-Z has been designed for operation in harsh environments. Usage of the system in high shock conditions has been confirmed by testing the system at 25G 11ms, 6-axes, 10times/axis during operation.

Operation Environments:
The 'sealed body' design of the FASTCAM SA-Z utilizes heat-pipe technology to ensure that during operation heat can be effectively drawn out from the inside of the system and dissipated via externally mounted fans. This ensures optimum air flow and prevents dust and corrosive particles from being ingested within the camera body where they can damage sensitive electronics. The fans may be disabled during recording for any vibration sensitive measurements.

The FASTCAM SA-Z camera has been extensively tested to ensure operation for extended periods in ambient temperatures up to 45 degrees C.

Specifications subject to change without notice.

PHOTRON USA, INC.
9520 Padgett Street, Suite 110
San Diego, CA 92126
USA

Tel: 858.684.3555 or 800.585.2129
Fax: 858.684.3558
Email: image@photron.com
www.photron.com

PHOTRON EUROPE LIMITED
The Barn, Bottom Road
West Wycombe, Bucks. HP14 4BS
United Kingdom

Tel: +44 (0) 1494 481011
Fax: +44 (0) 1494 487011
Email: image@photron.com
www.photron.com

PHOTRON (Shanghai)
Room 20C, Zhao-Feng
World Trade Building
No. 369, JiangSu Road
ChangNing District
Shanghai, 200050 China
Tel: +86 (0) 21-5268-3700
Email: info@photron.cn.com
www.photron.cn.com

PHOTRON LIMITED
Kanda Jinbo-cho 1-105
Chiyoda-ku, Tokyo 101-0051
Japan

Tel: +81 (0) 3 3518-6271
Fax: +81 (0) 3 3518-6279
Email: image@photron.co.jp
www.photron.co.jp

REV# 16.02.21